The
University
Of
Sheffield.

FULL-FIELD DAMAGE ASSESSMENT OF NOTCHED CFRP LAMINATES

THESIS BY

Fernando Salmon-Guzman

In Partial Fulfilment of the Requirements for the
Degree of Doctor of Philosophy.

Department of Mechanical Engineering
The University of Sheffield

January 2019

ABSTRACT

The work presented in this thesis constitutes the first dedicated application of surface full-field experimental techniques to the comprehensive damage assessment of open-hole compression (OHC) in composite laminates, under both static and fatigue loading. The relevance of the work comes from OHC being one of the two main tests used in industry to measure damage tolerance of composite material systems.

The main motivation for the work is the existence of a gap in the published literature pertaining to the location of the occurrence of different damage events during the life of notched composite structures. Additionally, the effect of toughening laminates by interleaving of particles, intended to improve the damage tolerance, was studied. As such, the main goal was to demonstrate the viability of using full-field non-contact experimental techniques to study the evolution of damage in notched carbon fibre reinforced polymer laminates. The specific techniques used were thermoelastic stress analysis (TSA) and digital image correlation (DIC).

It was found that a characteristic damage sequence is independent of the material system and that final failure of the laminate is controlled by the development of crush zones at the east and west sides of the hole. These crush zones result from the collapse of kink bands whose development is in turn controlled by matrix cracking early in the life of the laminate. Hence, by characterizing the sequence of damage events and their occurrence in notched coupons, the design allowables of actual composite structures can be better approximated. Pertaining to the effect of particle interleaving, statistical analysis of life data demonstrated that it could not be concluded that this kind of toughening improves the OHC fatigue life of the laminates tested.

The work presented in thesis thereby demonstrates that TSA and DIC can be applied to the study of damage in composite laminates and, thus, represents a significant step towards an improved understanding of damage morphology and evolution in heterogeneous materials.

ACKNOWLEDGEMENTS

The submission of this thesis cannot go without saying thanks to the many ones that helped and cheered me unto this day; it would have been a lot harder without them.

To Dr. Rachel Tomlinson, my doctoral adviser, I would like to say: thank you for the unrelenting support from the very first day and thank you for your dedication to your role as adviser and mentor to the very end. I hope this thesis can repay a bit of all the hard work you put into it too.

To Mr. Richard Kay, Lea lab technician: Thanks for all the help with my experiments and the scintillating conversations. I cannot recall a day when you were not sporting a smile during my time at the lab.

To Mr. Christopher Todd, electronics technician: Thanks for all the help in resuscitating the MAND and instrumenting it. Keep practicing that Spanish!

To all those lecturers that gave me the opportunity to help as a teaching assistant: Thanks for all the fun and learning!

To my friends and fellow PhD candidates: Thank you for all the shared experiences and laughs.

To my parents: I know for a fact that were your incessant prayers that got me through the end. I cannot thank God enough for the privilege of being your son.

To my beloved daughter Joelle: thank God that such a thing like your smile exists.

Finally and most heartfelt, to my darling wife Eli: thank you for keeping me sane during all these years of absent-mindedness. It was a monumental effort and for that you deserve a medal ;)

CONTENTS

FIGURES

TABLES

CHAPTER 1 INTRODUCTION

1.1 Background and motivation

The invention of the first viable process to produce structurally sound carbon fibre was made at the Royal Aircraft Establishment at Farnborough, UK in 1963. Since then, its application as reinforcement in the construction of advanced structures has seen exponential growth. A very relevant example of this is the use by weight of carbon-based composite material in the latest generation of civil aircraft as shown in Figure 1-1a for Boeing airframes. The distribution of materials per weight in Boeing's 787 accounts for more than 50% of composite. Figure 1b shows the material distribution in the 787. By volume, the 787 comprises 80% of composite, most of which is carbon fibre reinforced polymer (CFRP) laminate.

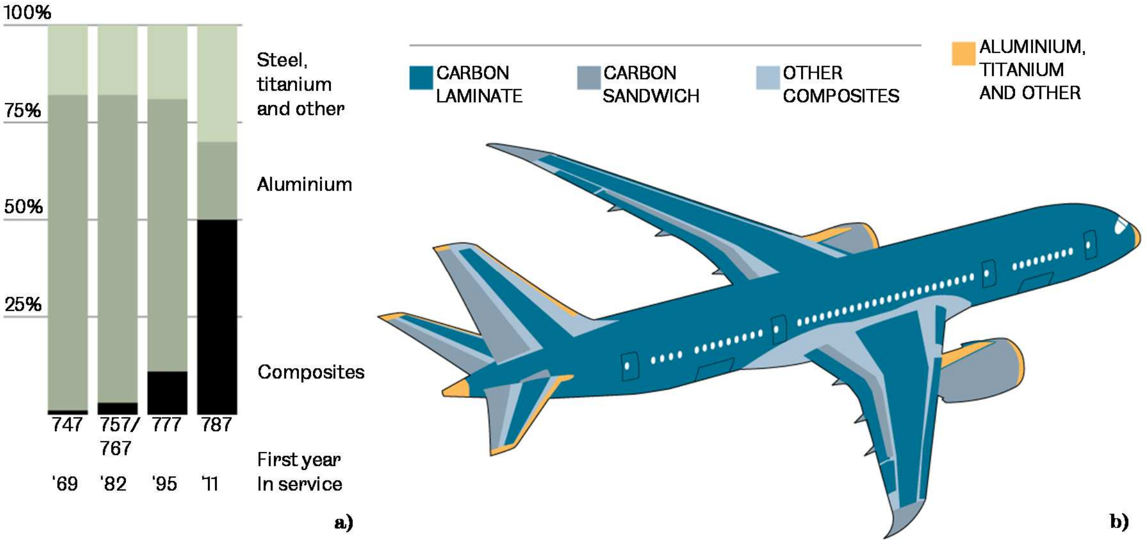

Figure 1-1. (a) Materials by weight in Boeing airframes; (b) Boeing 787 airframe materials[1].

Arguably, the most salient innovation in the 787 airframe is the all-composite fuselage consisting of 4 filament wound barrel sections joined end to end. This eliminated the use of more than 50,000 fasteners simplifying the

---

[1] https://archive.nytimes.com/www.nytimes.com/interactive/2013/07/29/business/The-Jump-to-a-Composite-Plane.html

manufacturing process and further reducing the net weight of the airframe. Other benefits include a higher allowable cabin air pressure due to the superior fatigue properties of continuous CFRP under tension and higher cabin humidity levels as corrosion is no longer a concern; thus reducing the potential for respiratory distress of the passengers.

The benefits of an integral composite construction are manifold, delivering much welcomed fuel savings and reduced emissions to operators and regulatory bodies, and increased comfort to the passengers, *inter alia*. However, the engineering cost needed in order to certify composite structures to the same level of safety as the more traditional metallic skin fuselages is significantly higher. The main reason is that the understanding of the damage mechanics of composites, in particular PMCs (polymer matrix composite materials), is still in its infancy when compared with metals. This is partly due to the relatively recent advent of composite structures, but a more plausible reason is the increased complexity of the damage mechanisms and their interactions, with respect to metals.

A wide gamut of damage mechanisms is the natural consequence of the inherent microstructural anisotropy and heterogeneity of FRPs compounded with the possible loading and environmental conditions. This complicates the design process in order to substantiate the durability and reliability of composite components. For a safety sensitive application like civil aerospace, it is paramount to understand the mechanisms that affect the damage tolerance and durability of the structure in order to validate the continued airworthiness of the vehicle.

It is commonly acknowledged that two of the most harmful conditions for composite laminates are the bearing of compressive loading following a low-energy impact and in the neighbourhood of notches [1]. This has led to two standard structural tests being widely used to measure damage tolerance, termed compression after impact (CAI) and open hole compression (OHC). The performance in both tests is matrix dominated but the requisite properties for a high score in both are incompatible: CAI is directly linked to matrix toughness [2], [3] and OHC has been shown to relate to matrix stiffness [4], [5]. Understandably, the matrix is often recognised as the Achilles heel in polymeric composites as it limits laminates from realizing the full potential of the fibre reinforcement. However, it is necessary to support the fibres and provide transverse strength which are equally important properties.

All polymers can be classified into two broad classes based on their thermal processing, namely: thermoplastics and thermosets [6]. The main distinction between them is that the former can be thermally reprocessed and the latter cannot. Thermoset polymers with a high degree of crosslinking are stiff but brittle and thus perform poorly in CAI. Conversely, thermoplastic matrices are tougher, but this is at the expense of reduced compression properties in hot-wet conditions (due to their lower glass transition temperature, T_g). Due to processing cost, manufacturing considerations and excellent mechanical and chemical resistance, epoxy resins are the most common matrix materials. In order to improve their impact strength without sacrificing the modulus and good hot-wet properties particulate fillers are added as a secondary phase [7], [8]. There is a variety of particle compositions and sizes used, but the intent is the same —to increase the polymer's toughness. For the subject materials of this work, the particles are added to the resin rich region between plies in a laminate, the so-called *interlaminar* region. This *interleaving* of toughened matrix in laminates is primarily motivated by the need to improve the low-velocity impact damage resistance, and extensive work has been performed by the industrial sponsor (Solvay Composites) on CAI of interleaved laminates [9]–[14]. The scope of this work covers instead the effect that interleaving has on OHC properties.

Referring back to the specific example of Boeing's 787 airframe, the manufacture of large integral composite components needs to be supported by increased reliability. The removal of 1,000s of fasteners only makes the remaining notches or stress raisers more critical. The same goes for damage tolerance as the increase in size of the components will evidently result in higher repair costs. Therefore, in order to achieve certification of a composite airframe, manufacturers need to demonstrate excellent understanding of the material response under normal operating conditions (mechanical and environmental fatigue) and after an overload event (mechanical, thermal or electromagnetic). This understanding has to be necessarily informed by experimental testing of representative loading conditions on representative material systems and configurations. It follows that suitable experimental techniques are required as a means of quantifying the structural response of composite components in order to identify the presence of damage and monitor its development. This constitutes the fundamental motivation for the work herein, namely to investigate the use of full-field optical techniques for the study of damage in composite laminates.

Full-field experimental techniques have the potential to capture high resolution maps of strain or stress. The techniques explored in this work are digital image correlation (DIC) [15] and thermoelastic stress analysis (TSA) [16], which will be described in more detail in chapters 5 and 6. As for the load conditions and material systems, the scope of the work presented in this thesis is limited to continuous CFRP laminates subjected to uniaxial compression loading, both static and cyclic. As such, any description of composite materials hereafter should be understood within this scope, unless otherwise stated.

1.2 Goal and objectives

The overarching goal is to demonstrate the use of DIC and TSA to study the surface damage morphology of notched CFRP laminates subjected to compressive loads. Additional to this is the aim to relate the damage state to residual properties and ultimately discriminate the effect from particle interleaving toughening.

As argued before, the reduction in fastener count will only increase the importance of the remaining stress raisers. In contrast to metals, compression loading is often the limiting condition in composite laminates and the resulting stress state is exacerbated by the presence of notches; the general case of which is a circular open hole. Hence, the importance and value of studying damage during OHC testing.

The specific materials being studied are developmental CFRP laminates manufactured by Solvay Composites. A baseline laminate containing a neat resin was compared against three interleaved systems under static compression and against a selected interleaved system under compressive fatigue.

The following list of high-level objectives has been addressed in the path to meet the project goal:

1. Design a bespoke fixture for the application of static and dynamic loading whilst providing appropriate visual access for DIC and TSA measurements. The loading conditions and failure modes are to be aligned with current industry standards.
2. Develop and optimize the DIC and TSA techniques for the observation and quantification of damage in CFRP laminates.
3. Study the mechanical response of notched laminates under compression and the resulting damage/failure modes.
4. Investigate the effects of interleaving in the static and fatigue performance of notched laminates with the aid of full-field methods.

1.3 Novelty

The choice of experimental techniques was made with the intent of gaining an insight into the damage processes of composite laminates without interrupting the test. Data in traditional standardized testing of composite laminates is typically acquired using single or point value instruments, e.g. load cells, displacement transducers, strain gauges, etc. However, damage processes in composite materials are diffuse and assuming that the useful cross section is continuous when characterizing the material is an oversimplification, which neglects the true nature of the damage.

The chosen techniques, DIC and TSA, can capture surface data maps which provide this insight through the development of deformation gradients without the need to stop the test (unlike X-ray based techniques, for example) or to de-ply partially damaged and failed specimens. Also, both techniques are non-contact and require relatively simple (although not trivial) specimen preparation. As such, they were very adept for the experimental programme intended.

DIC has been extensively used in the characterization of composite materials. However, the majority of the work published to date deals with static testing and from this a relatively small amount describes the application of DIC to the compressive loading in notched laminates. The specific challenges associated with the load axiality and the minimization of buckling in a fixture that provides a large amount of visual access has not been considered. Moreover, the optimal specimen preparation, camera and lighting configuration, and correlation parameters that enable the capture of acute strain gradients that develop the vicinity of the notch at the onset of failure also remain to be explored in detail.

It will be demonstrated in the current work how the optimized test parameters and settings can be applied to compare the static compressive response of un-notched (UN) specimens with notched ones, in order to characterize the influence of an open hole at the laminate level. After this, knowledge from the static testing is leveraged to develop a data reduction scheme in the application of DIC to capture live fatigue tests using a single camera at frequencies lower than the loading frequency. This will allow for the observation of stiffness degradation in OHC fatigue through the evolution of the strain map.

TSA relies on the temperature variation that results from changes in stress, which makes the technique an obvious choice for the observation of fatigue damage. Although TSA has also been used extensively for the study of damage in composite materials, to the authors knowledge, its specific application to study OHC fatigue has not been reported in literature thus far. Pertaining to this, the aspects reviewed in this work include:

- The identification of a characteristic damage sequence in OHC fatigue and its relationship to the specimen life.
- The influence and interaction of the paint coat, loading frequency and optics on the TSA signal attenuation and the noise floor.
- The observation of subsurface delamination and its relation to residual life.

The adaptation and development of the above techniques was motivated by the need to produce enriched datasets in order to cast light on the survivability of notched laminates and resolve if interleaving improves it.

1.4 Structure of the thesis

The thesis sets out to give an overview of the mechanics of continuous CFRP laminates in Chapter 2, as found in published literature, with a focus on their compressive response. From this stems a discussion about the ongoing lack of agreement with respect to failure criteria. This demonstrates the need for the continued development of experimental methods in order to inform and validate these criteria. Lastly, the chapter describes the effect that an open–hole (notch) has and the most relevant rationalizations found in literature.

Chapter 3 begins by describing the issues resulting from the inherent brittleness of the most conventional matrix materials, i.e. epoxy resins, which are in part a subject of the current work. This helps to warrant the research on toughening mechanisms, and the specific case of particulate fillers is set forth. The last section deals with the work done on the use of particulate filled polymeric blends in the interlaminar region to increase its fracture toughness.

Chapter 4 provides details of the materials systems studied, namely, the manufacturing process, lay-ups, toughening denotation and specimen geometry. Also, the design of a uniaxial compression fixture is described. Although in line with current ASTM standards, the fixture was designed to provide ample visual access and adapted for the application of cyclic loading. The last portion of the chapter reports on the instrumentation used, the data acquisition scheme and the steps taken to validate the loading conditions against the relevant standards.

Chapter 5 describes the application of 3D – DIC to OHC static testing. First, a description of the fundamentals of digital image correlation and stereo vision is given. Then, details of the experimental setup and its validation are provided. The chapter also emphasizes the measures taken to ensure the minimization of the measurement uncertainty and its quantification. Thus, the efforts taken to gauge the influence of specimen preparation and detector resolution are described. Lastly, results from static testing of un-notched and OHC specimens are presented and compared for the subject material systems.

Chapter 6 deals with the application of TSA and 2D – DIC to the fatigue testing of OHC specimens. The beginning of the chapter gives overview of the theoretical fundamentals and historical development of TSA, with a focus on its application to composite testing. Next, the validation of the testing parameters used for the TSA measurements is discussed. This is followed by the description of the experimental setup used and a series of validation studies performed. Next, details of the 2D – DIC setup used to capture are provided. The last portion of the chapter reports the results obtained and describes different methods to identify and assess damage in OHC fatigue.

Finally Chapter 7 lists the main conclusions and gives recommendations on further work.

CHAPTER 2 COMPRESSION OF NOTCHED COMPOSITE LAMINATES

2.1 Overview of CFRP composites

A composite material is by definition the combination of two or more macroscopically distinct constituents or phases that are mutually insoluble. The constituents are commonly classed as either *reinforcement* or *matrix* [17]. The reinforcement phase can be in the form of fibres, particles or flakes and typically exhibits very high specific properties, e.g. stiffness or strength. The matrix material serves as a binder for the reinforcement and helps to translate its properties to the composite component.

Fibrous composites are the most common and they can be classified based on the length of the fibrous reinforcement, namely, discontinuous fibres (or whiskers) and continuous. Of the two kinds, components made with the latter realise more of the fibre properties but are more expensive to manufacture. The continuous fibre materials can be manufactured from woven fabric or unidirectional (UD) tape. Cloth made from UD tape exhibits the highest in-plane properties and they can be stacked in different orientations in order to tailor the laminate properties. Laminates made from UD CFRP are the subject of this work and are considered high performance materials, evidenced by their extensive use in aerospace structures.

Aerospace grade carbon fibres have a diameter of about 5-6 μm and consist of graphite crystallites arranged in ribbons of the so called *turbostratic* structure resulting from the carbonization of different precursor filaments [17]. This graphitic form of carbon is highly anisotropic, with a theoretical Young's modulus of 1,000 GPa in the direction parallel to the basal plane and only 35 GPa in the direction normal to it. The final properties of the fibre depend on the distribution of the orientations of the turbostratic ribbons with respect to the fibre axis. This distribution is the result of a heat treatment known as graphitization which can produce a wide range of mechanical properties. Polyacrilonitrile (PAN) filaments are the most common precursor for aerospace fibres and are now typically supplied in four designations, namely, high strength (~3.5 GPa, and a modulus of < 230 GPa), intermediate modulus (265–320 GPa), high modulus (320–400 GPa) and ultra-high modulus (~440 GPa) [18]. The exceptional properties of carbon fibres are a result of the so called size effect, which is related to the inverse relationship between the fibre diameter and the probability of defects in the microstructure.

Following the choice of fibre, the strength of the matrix–fibre interface (or any other interphase for that matter) must be engineered to provide the desired properties to the laminate and make optimum use of the constituents. In order to enhance the adhesion of the matrix to the fibres, their surface is roughened by chemical etching, before applying the correct finish or sizing to control the bonding strength. The laminate transverse and out-of-plane strength, germane to this work, are controlled by the interphase properties, but so are the fracture resistance, creep compliance, and environmental degradation. Since several of these properties have competing requirements, it often the case that a compromise has to be made in order to design a balanced composite.

As aforementioned, thermoset polymers are the most conventional matrix materials for aerospace CFRPs, in particular epoxy resins. These resins are typically designed to cure in an autoclave at either 120–135 °C or 180 °C, with the latter being the preferred kind for primary structures [6]. Once cured, the high degree of crosslinking in the polymer network confers the matrix with superior mechanical properties, high resistance to solvent-attack and good thermal and dimensional stability. One of the most common forms CFRP stock is known as *prepreg*. To produce it the fibres are pre-impregnated with the epoxy resin and stored in sheets or cloth for the subsequent manufacture of laminates.

2.2 CFRP laminates

A *laminate* is formed by stacking a two or more of layers or *laminae* in different orientations to produce the desired properties. The prime purpose of lamination is to tailor the directional properties so as to match the loading conditions [19]. In the case of UD composites, each lamina or ply is orthotropic with the principal material axes in the direction of the fibres (longitudinal), normal the fibres in the plane of the lamina (in-plane transverse) and normal to the plane of the lamina (out-of-plane) [20]. The notation used for these directions is 1, 2 and 3 and their orientation is independent of the arbitrary choice of laminate coordinate system, whose axes are notated as x, y, and z. The out-of-plane directions are typically the same and thus the ply angle θ between directions 1 and x is used to define the stacking sequence or lay-up of the laminate, as shown in Figure 2-1. The angle is measured counter clockwise by convention and the reference x-axis can be selected arbitrarily but has to be reported.

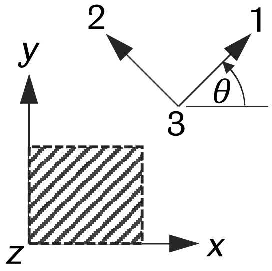

Figure 2-1. Laminate or stress (*x, y*) and material or natural (1, 2) coordinate systems. They are related by the ply angle *θ*. The out-of-plane axes (*z* and 3) are coincident and point away from the page.

The designation of a composites laminate comprises the number, type, orientation and stacking sequence of its plies [21]. The configuration of the different plies is known as *layup* whereas the detailed expansion of the ply order is referred to as stacking sequence. A layup containing only 0° and 90° plies is termed *crossply* (CP), one with intermediate angles (0°< θ > 90°) *angleply* (AP) and one with a combination of angles is known as *multidirectional.* The special case of a layup with the same number of ply angles in every direction and symmetric about the mid-plane yields a *quasi-isotropic* (QI) laminate, viz. it displays isotropic response in the laminae plane. The convention used in this work to designate laminates is, for example [+/-/0/90]$_{2S}$, which describes the layup shown in Figure 2-2, for instance.

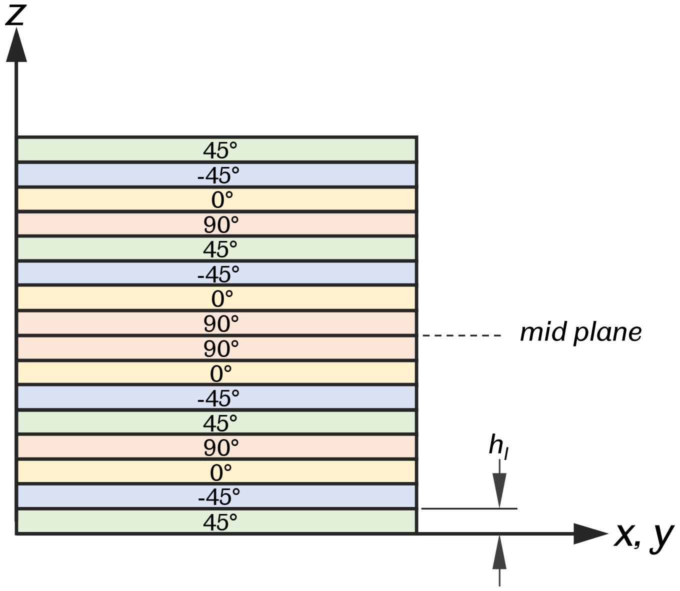

Figure 2-2. Example of a 16-ply QI laminate: [+/-/0/90]$_{2S}$.

Laminates made from prepreg cloth are produced by three basic layup processes, namely laying, winding and moulding. Only the first process is of interest here; details for the last two can be found elsewhere, e.g. [18]. Lamination performed by laying is commonly done by hand and thus the ply stack is known as a *hand layup*. After the layup operation, the prepreg stack is sealed in a bag and evacuated. Then it is consolidated at high temperature and pressure inside an autoclave in accordance to the pertinent standard. This processing method delivers a very high quality product with extremely low void formation which is the reason it is largely used for aerospace components.

2.3 Compressive response of UD laminates

Contrary to the superior tensile strength of UD FRP laminates in the fibre direction, they exhibit a significantly lower resistance to compression. This is because tensile strength is mainly dictated by the fibre properties, high strength and high modulus, whereas compressive failure is mostly driven by matrix properties, which has much higher toughness but lower strength in comparison. Compressive failure can involve the following competing mechanisms, as listed by Fleck [5]:

A. Elastic microbuckling

B. Plastic microbuckling

C. Fibre crushing

D. Splitting

E. Buckle delamination

F. Shear band formation

From these, it has been repeatedly shown that the mechanism central to compressive failure is fibre microbuckling (A and B above) [22]–[25]. Rosen [26] analysed this and assumed that an elastic bifurcation due to geometric nonlinearity gives way to two distinct modes (see Figure 2-3), namely, (a) transverse or extensional mode and (b) shear mode.

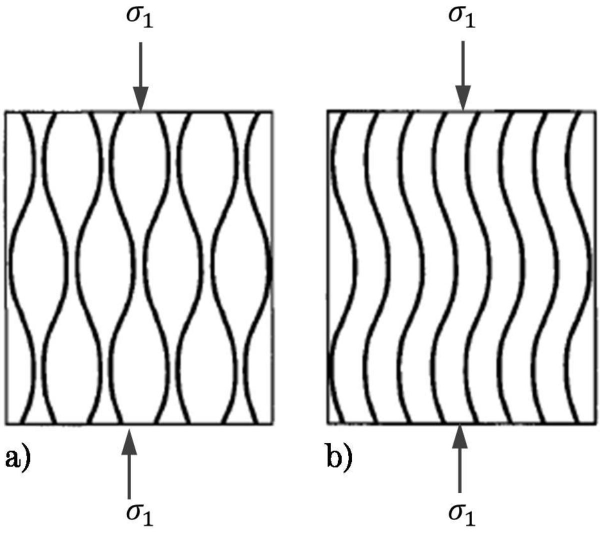

Figure 2-3. Microbuckling modes in UD laminate under compression: (a) Out-of-phase or extensional and (b) in-phase or shear. Adapted from [19].

In the first, the fibres buckle out-of-phase causing the matrix to strain in the transverse direction. In the second, in-phase buckling of the fibres leads to the formation of kink zones, which cause the fibres to break along a two parallel planes, creating a so-called *kink band*. At high fibre volume fractions V_f (which is typical of aerospace materials), the tendency of the fibres is to undergo cooperative buckling and thus the shear mode prevails. Rosen's [26] assumption of elastic buckling leads to compressive strength of the in-phase mode as being equal to the elastic shear modulus of the matrix. Soutis [27] found that the compressive strength was 25% of the shear modulus for a T800/924C prepreg $[0]_{16}$ laminate with a V_f = 0.60. Several causes of the overestimate have been offered ranging from the three-dimensional nature of the reinforcement [28] to the detrimental effect of irregular fibre spacing, matrix plasticity, fibre misalignment and poor interfacial strength [29].

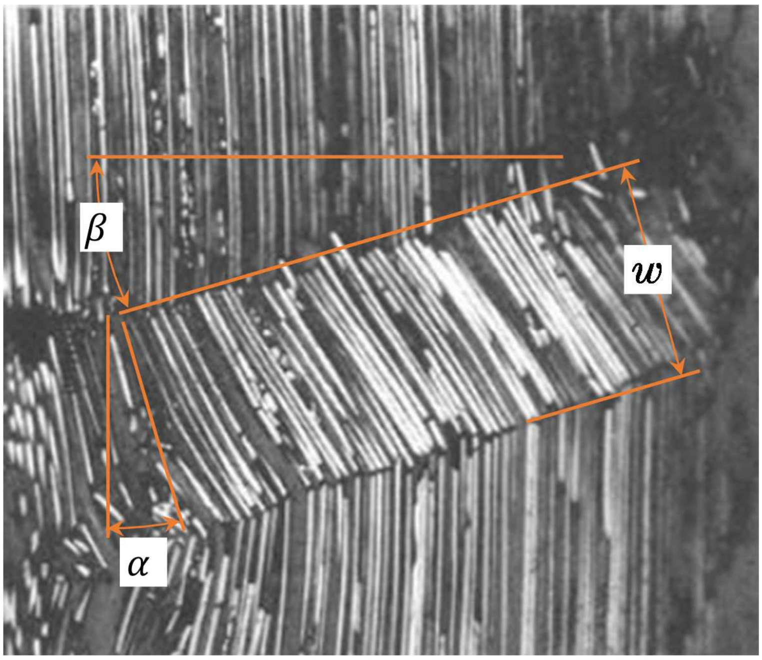

Figure 2-4. Kink band geometry. Adapted from [27]**.**

These early attempts to fit Rosen's model argued that these imperfections had a knock down effect on the compressive strength and proposed the use of empirical correlation factors. However, studies by Argon [30], Batdorf and Ko [31], and Budiansky and Fleck [32] provided evidence that the dominant mechanism in FRPs is instead plastic microbuckling. Namely, that the compressive strength is affected by initial fibre misalignment ϕ_0 in combination with plastic shearing of the matrix; ϕ_0 is defined as the angle subtended between the 0° axis and the fibres in the 0° plies. As a result, the 0° compressive strength in typical aerospace CFRPs is ~60% of their tensile strength. Figure 2-4 shows a typical kink band and the associated geometrical parameters: band width w, band angle β and fibre rotation α.

The constitutive laws that govern the sequence of events in the formation of a kink band remain under discussion [33], [34] and no single model has gained universal acceptance among researchers yet. Several studies have investigated the formation of kink bands [23]–[25], but due to the difficulty in producing pure in-plane kinking, a detailed validation of micromechanical models has not been possible. Lately, Gutkin et al. [35] made in-situ observations using a scanning electron microscope of longitudinal compressive failure in UD and CP carbon/epoxy laminates with a single notch. They found that the first damage mechanism to appear are matrix microcracks in a region close to the interface. When these microcracks accumulate they coalesce and tend to form large splits that stop supporting the fibres and allow them rotate to start forming the kink band. The role of the matrix in resisting the nucleation, propagation and coalescence of microcracks is very relevant to this work and forms the basic motivation for matrix toughening, as will be discussed in Chapter 3.

The transverse (normal to the fibres) compressive strength is also controlled by the matrix properties. Puck and Schürmann [36], [37] suggested that the orientation of the fracture surface of specimens failing under transverse compression agrees with the Mohr-Coulomb criterion, which indicates that matrix compression specimens fail by shear. Figure 2-5 shows a failure envelope for combined transverse (matrix) compression σ_2 and in-plane shear τ_{12}. The fracture modes are designated based on the crack direction, i.e. the inclination angle θ_{fp} between the longitudinal fracture plane and the thickness direction. The distinction is made between straight $\theta_{fp} = 0°$ (Mode A and B) and oblique $\theta_{fp} \neq 0°$ (Mode C) cracks. For a pure compression loading the shear failure suggests that the $\theta_{fp} = 45°$, however it is experimentally seen that the angle is typically $\theta_{fp} = 53 \pm 2°$ for glass or carbon based FRPs [36], [37]. This difference has been explained by the interaction of compressive stress at the potential fracture surface with an associated friction stress [35]. Even though there is no macroscopic interface before fracture, hence the 'potential' above, the macro-mechanical friction can be explained by the added effect of tractions at matrix microcracks before bulk failure. This underlines again the role of matrix toughness in discouraging microcrack formation.

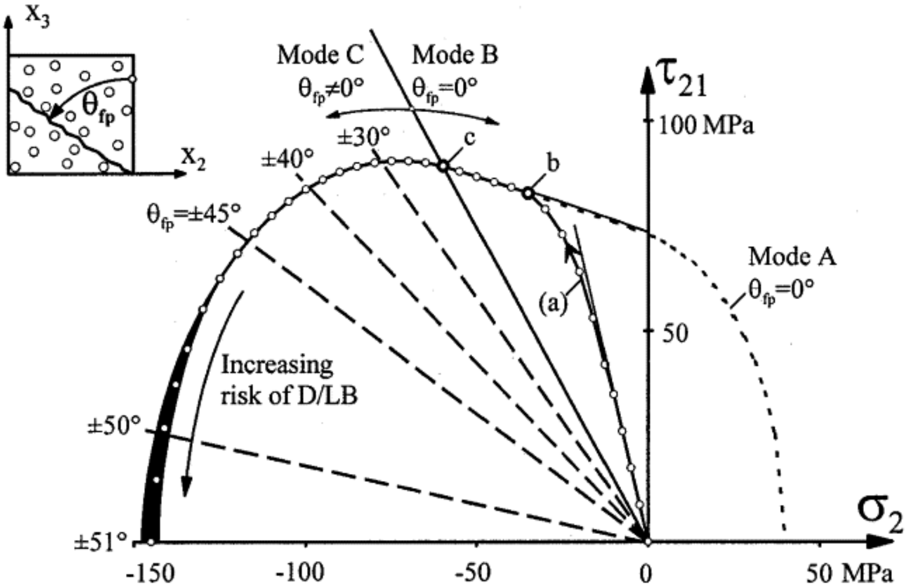

Figure 2-5. Fracture envelope for combined (τ_{12}, σ_2) stresses, the associated fracture modes (A, B and C) and the fracture angle θ_{fp}. D/LB refers to the increasing risk of delamination and local buckling due to the wedge effect in matrix compression failure [37].

For a multidirectional laminate the most damaging matrix compression failure mode is the so-called ‘explosion effect’. When subjected to pure compression, plies running transverse to the load will form a wedge upon fracture increasing the risk of delamination and local buckling as shown in Figure 2-5. This is caused by high compressive stresses $\sigma_n = \sigma_2 \cos^2 \theta_{fp}$ that act on the fracture planes at $\theta_{fp} > 45°$. With continued loading, as illustrated in Figure 2-6, the wedges will push against adjacent plies causing delamination zones and local buckling. For 0° plies this is especially harmful as it promotes macroscopic buckling.

The influence of angle-plies on the compressive strength of multidirectional laminates was studied by Berbinau et al. in [38]. The authors found that although $[(\pm\theta/0_2)_2]_S$ specimens with ±45° surface plies appeared to provide the highest resistance to fibre microbuckling, they showed a 10% reduction in strength when compared with a 0° UD laminate.

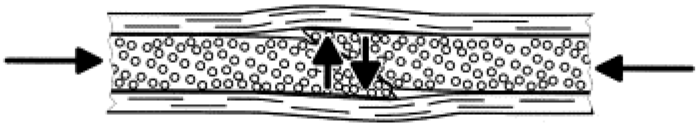

Figure 2-6. Illustration of the explosion effect due to a wedge shaped transverse compressive fracture [37].

2.4 Compressive response of laminates with an open hole

The reduction in strength under compression and the notch sensitivity of FRP laminates with an open hole has been investigated previously by several authors; notable studies are described below.

Guynn and Bradley [39], [40] and Guynn et al. [4] performed OHC tests of AS4/PEEK laminates and observed that the crush or damage zone is initiated by fibre microbuckling at the least supported locations, i.e. at the hole surface and at plies close to the free surface of the laminate. The in- and out-of-plane microbuckling preceded what they call *shear crippling* damage (kink band formation) as shown in Figure 2-7; which is in line with the compressive damage mechanics of un-notched laminates. They also noted that the local delaminations resulting from the fully formed kink bands did not propagate until bulk failure. They attempted to model damage with an elastic-perfectly plastic constitutive description but to no avail since they observed that the predicted stress at the crush zone was much higher that measured. A more realistic model was suggested that is able to capture the loss of stiffness resulting from the formation of kink bands and the resulting load transfer to the undamaged material.

Lessard and Chang [41] studied T300/976 laminates with a variety of lay-ups to investigate the influence of the stacking sequence and ply clustering on the OHC strength and damage modes. They also observed isolated damage in the 0° plies at 95% of the failure load, which was indicative of kink band development. Laminates with ply clustering exhibited lower OHC strengths, suggesting 0° clusters enhance large scale delamination due to the formation of a larger kink zone.

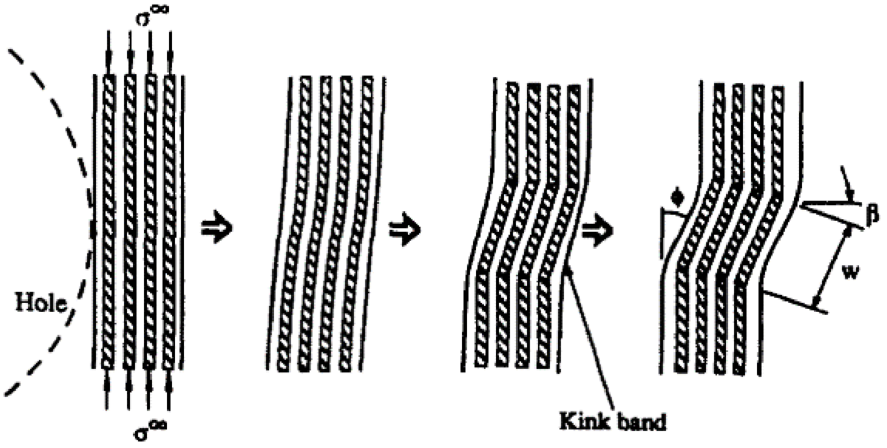

Figure 2-7. Schematic of kink band formation at the vicinity of the hole in OHC specimens [42]**.**

Soutis et al. [43] tested a $[(\pm45/0_2)_3]_S$ quasi-isotropic layup made from a T800/924C system with a variety of hole diameters D_h to investigate notch sensitivity. It is reported that the failure strain of the QI layup is not significantly different to the failure strain of UD 0° laminate, which is indicative of the relatively small influence of the ±45 plies on the microbuckling response of the 0° plies. They too conclude that the governing failure mechanism is fibre microbuckling leading to the formation of a kink band inclined at an angle $\beta = 5$ to 15°. The typical band width was equal to 8 to 10 fibre diameters (~50 μm) and the fibre rotation ~30°. The strength reduction due to the presence of the hole was of 35 to 70% for the different hole diameters. This range is due to the material system being relatively notch sensitive causing limited stress redistribution around the kink band before bulk failure. This is expected since, even though epoxies are inherently brittle, they exhibit a finite amount of ductility under compression. For this system the onset of microbuckling was 80% of the ultimate compressive strength σ_c with the resulting kink band growing in the 0° plies almost perpendicular to the load direction across the specimen. The damage in the off-axis plies was negligible at 95% σ_c. The authors claimed that large scale failure results from the unstable growth of the micro buckled zones.

In another study Soutis et al. [22] tested the same T800/924C system but varying the proportion of 0° plies from 100% to 17% in the layup. It was corroborated that the failure strain was independent of the layup and is mainly driven by the compressive stiffness of the 0° plies. The critical failure mechanism was again identified as microbuckling of the 0° plies causing the nucleation and growth of a kink band ($\beta = 5 - 20°$) that in turn leads to bulk failure. It was again observed that the ±45° plies play an important role of providing lateral support to the 0° plies to discourage out-of-plane microbuckling in order to attain a higher strain at failure. It was observed, that the off-axis plies reduce the notch sensitivity of the laminate at the expense of increased compliance and non-linearity in the stress-strain response.

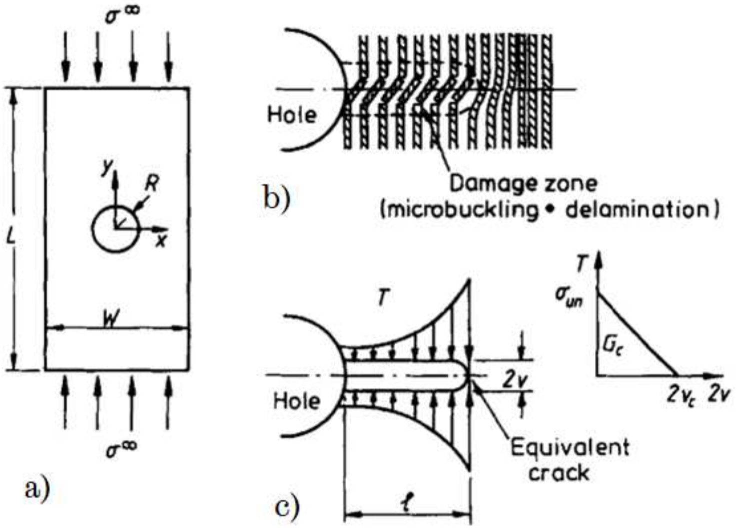

Figure 2-8. Schematic of the cohesive zone model for microbuckling of laminates with an open hole. Adapted from [22].

A crack bridging model developed by Soutis et al. [43] is able to adequately predict the compressive strength and the kink band length at the onset of failure. The damage zone due to microbuckling of the 0° plies, delamination and damage by plastic deformation of the off-axis plies is represented by a crack with a cohesive zone at its tip (see Figure 2-8), loaded on its faces by a crack opening normal traction T, set to decrease linearly with the closing displacement of the crack $2v$ from a maximum value of σ_{un} to zero at a critical crack closure of $2v_c$. The length of the crack is assumed equal to the length of the kink band and its growth is represented by the crack growth resulting from an increase in the remote stress σ^{∞}. The damage zone growth is determined by requiring that the total stress intensity factor at the equivalent crack tip is zero. One difficulty with the application of the model is the need for accurate measurements of the un-notched strength and the compressive fracture toughness of the laminates.

2.5 Compressive fatigue of CFRP laminates

Current standards for certification of the service life and damage tolerance of composite structures require large factors of safety in order to compensate for the deficiencies in the existent residual life prediction methodologies. This results in overdesigned structures and extensive and costly prototype testing to produce statistically significant confidence bounds for the component life. The need for improved accumulation and residual properties models motivates a large amount of research to achieve optimal use of composite properties, in particular, the specific (by weight) properties. Relevant precursory work on compressive fatigue of CFRPs is presented next.

Findings from a notable study by Soutis et al. [44] suggest that the causality in the damage mechanics of OHC fatigue tests is highly dependent on the load level. Notched laminates (D_h = 5mm) of a T800/924C system with a $[(\pm 45/0_2)_3]_S$ layup were loaded in compression-compression at three different maximum load levels, namely, 75, 85 and 90% of σ_c and a load ratio R = 0.1 (minimum load / maximum load). Soutis et al. [44] found that, at the 75% σ_c level, specimens displayed an increase in residual strength after 10^6 cycles of 15%. This was explained by extensive stress redistribution around the hole due to the damage sequence. For this load level, damage appeared first in the form 0° splits at the top and bottom of the holes within the first 100 cycles. This was followed by other longitudinal splits tangential to the hole after 10^3 cycles. These splits were found to arrest damage development from the ±45 plies, which was in the form of small matrix cracks. By arresting damage growth to the central band and diffusing the stress concentration, the specimens are effectively reduced to two strips of undamaged material and the laminate strength is increased. The laminate stiffness was decreased by 5% only. Damage development at 85% σ_c level was qualitatively similar to damage at the 75% σ_c, but propagated over a greater area and resulted in a 20% strength increase, likely caused by greater blunting of the stress concentration. At 90% σ_c fibre microbuckling at the 0° plies developed from the first cycle and became the driving damage mechanism, reducing the life of the specimens by at least 1 order of magnitude. This suggests the existence of a load threshold for the primary damage mechanism; namely, that above a certain load level more harmful microbuckling will appear at low cycle counts, leading to the formation and propagation of kink bands, thus accelerating bulk failure. Below this threshold subcritical damage growth will in fact attenuate the stress intensity around the notch, desensitizing the laminate to the hole to extend its life.

Analytical models have been produced for the prediction of the dynamic compressive response of FRP laminates in an attempt to capture the rate-dependent response of the microbuckling mechanism [45]–[48]. Slaughter and Fleck [45] attempted to describe the constitutive behaviour under cyclic compression using cyclic plasticity theories and found that composites with polymeric matrices are better described by a Mroz plasticity law [49] which negates plastic strain accumulation (ratchetting). In order to predict fatigue life, the same authors used a Coffin-Manson relation [50] and observed that microbuckling behaviour changed depending of the cyclic load range. They distinguished between monotonic (static) microbuckling caused by plastic collapse and fatigue microbuckling caused by progressive loss of fibre support due to matrix microcracks. This suggested that provided that the peak remote stress σ_{max}^{∞} is below the monotonic microbuckling load, the number of cycles to failure N_f is nearly independent from the fatigue ratio R. The same authors [46] modelled microbuckling of FRPs as a standard linear viscoelastic solid and suggested the existence of a critical stress level that is dependent on the fracture toughness of the material. This stress level divides failure by viscoelastic microbuckling from plastic yielding in the kink band causing plastic collapse.

A couple of studies by Slaughter et al. [47] and Fan and Slaughter [48] give consideration of the effect of load rate in the microbuckling response. Their models account for initial fibre waviness, inertial effects and nonlinearity in the constitutive relations (approximated by a Ramberg-Osgood strain hardening rule [51]). Results from the first model [47] indicate that under constant stress the inertial effects in fact decrease the dynamic compressive strength to approximately 90% of the static compressive strength for large initial fibre imperfection wavelengths. Since experimental provisions for constant load dynamic testing are difficult to realize, Fan and Slaughter [48] instead proposed a model under constant strain rate $\dot{\epsilon}$, which can be attained in a split Hopkinson bar. This second model predicts that the dynamic compressive strength increases rapidly above a certain strain rate. For a typical T800/924C carbon/epoxy system this transition occurs around $\dot{\epsilon} > 0.1\,s^{-1}$, but is dependent primarily on fibre misalignment wavelength [48]. This model also predicts a reduction in the kink band width at high strain rates down to a minimum of approximately half of that from static loading. For the current work, the most relevant conclusion from these two models is that the inertial effects from constant loading favour microbuckling, whereas loading inertia from constant strain rate resists microbuckling. Since cyclic fatigue is commonly applied in a sinusoidal manner, there is a combination of both effects. However, it is theorized that at the loading frequencies (~10 Hz) and compression levels (80% σ_c) used in Chapter 6 the instantaneous strain rate will discourage the kink band growth, thus delaying large scale delamination and extending the life of the specimens to practical test durations.

2.6 Discussion and remark on motivation

From the literature review above it can be foreseen that a substantial amount of research effort is still needed in order to understand and predict failure of composite laminates under compression. Failure criteria can be distinguished between static and dynamic. Two review papers encompass the current state of knowledge about composite laminate failure:

- A detailed view of the leading criteria in the first set can be found in an excellent review of the so-called World Wide Failure Exercise (WWFE) by Hinton et al. [52]. The mammoth exercise's aim was to evaluate and rank models for the prediction of failure envelopes for a variety of FRP laminates under biaxial static loading, as well as the stress-strain curves. No model was found to be able to capture material behaviour accurately under all loading conditions. However, from the pool of participant models, four theories (Zinoniev, Puck, Tsai and Sun) stood out as the most robust. Although a definitive model is yet to be found, the study represents a long stride towards closing the knowledge gap between theoreticians and design practitioners.
- The variety of models for fatigue life prediction and structural degradation can be reviewed in [53]. Fatigue models can be classified into three categories: (i) fatigue life or S-N models, (ii) phenomenological models for residual properties (stiffness/strength) and (iii) the progressive damage models. The most important outcome of all models is arguably the life prediction the material based on the particular criteria to define failure. The review authors argued that progressive damage models are the most promising since they can quantify the damage state of the structure and relate it to residual mechanical properties and service life.

From these review papers, it may be seen that the value of developing better experimental techniques and methodologies for composite testing is twofold. First, the certification of composite structures still depends to a large extent on expensive structural testing and so it is paramount that data collection is reliable and efficient. Second, the development and validation of analytical constitutive models depends on explicit experimental studies in order to accrue systematic knowledge of the parameters that affect damage modality and its interaction.

To date, there is a paucity of dedicated experimental studies of compressive fatigue of FRP laminates, let alone OHC fatigue. The work contained in this thesis in part aims to showcase the potential of full field experimental techniques to obtain a detailed view of the damage mechanics in composite structures.

CHAPTER 3 INTERLEAVING OF COMPOSITE LAMINATES

3.1 The need for matrix toughening

Epoxy resins display an excellent combination of mechanical properties, thermal stability and corrosion resistance. They also possess good dimensional stability, due to a relatively high creep modulus. However, the inherent brittleness caused by the high degree of crosslinking after curing results in poor fracture resistance. Although they are the most conventional matrix material in current advanced carbon based laminates their impact resistance is cause of concern to designers, in particular low velocity impact [2], [54], [55].

The shallow macroscopic dents left on the impact side left by a high mass at low velocity are defined as Barely Visible Impact Damage (BVID) [56] since it gives no indication of the internal damage extent. This poses a problem for maintainability, since significant internal damage can go unnoticed and so hinders the reliability of the structure. This internal damage typically is in the form of a network of matrix cracks and delaminations; higher energies can also cause fibre fracture at the far side [2]. Of the three damage modes delamination is the most deleterious to the residual compressive strength as it creates *sublaminates* with reduced flexural stiffness. The delamination area, typically measured by ultrasonic C-scan, has been found to correlate with the residual CAI strength [54].

Laminates with a tougher thermoplastic matrix (AS4/PEEK) developed significantly less damage [57]. However, the regular use of thermoplastic matrices in aerospace primary structures has not been realized due to relatively higher processing costs and lower hot-wet properties than the more established epoxies. Although the improvement of the CAI strength is the main driver of research on toughening of thermoset matrices and carbon/epoxy laminates, OHC strength benefits from a tougher matrix, as it serves to discourage crack initiation and coalescence [35].

3.2 Toughening of epoxy resins

Increased toughness is desirable in epoxy matrices but, ideally, this should be accomplished without sacrificing other properties. Of particular importance to the OHC and CAI performance of laminates is the modulus, since the matrix is responsible for providing lateral support to the fibres in order to resist microbuckling.

Current strategies to increase toughness of epoxies typically involve the addition of a secondary phase in particulate or liquid form. The most common liquid additives are elastomers (typically rubbers) [58]–[61] but crystalline polymers have also been shown to improve fracture toughness [62], [63]. On the other hand, a variety of particulate fillers has also been investigated, which can be classified based on the particle material compliance; this criterion is important as the resulting toughening mechanisms are different. Notable studies on “hard” particles include silica nanoparticles [64]–[66], metallic oxides [67], glass [68] and mostly thermoplastics [69]–[72], whereas softer particles are typically elastomers, mostly rubbers [59], [69], [73], [74].

Epoxy toughening is a wide and complex research field and, as such, providing a detailed taxonomy of the additives and their effects is out of the scope of this work. It is only of particular interest to discuss the toughening mechanisms that result from adding particulate fillers and how they affect other macroscopic properties. Many energy absorption mechanisms and their corresponding models have been proposed, namely crack pinning, crack deflection, crack bridging, particle yielding, particle debonding, microcavitation, crack tip blunting and particle induced localized plastic deformation [75]. The specific mechanisms and their sequence of occurring in a particular blend are a function of the base matrix and particle material as much as the interface strength [66]. It has also been shown that, not all of the mechanisms explain the increase in fracture toughness [65], [66], [74].

Studies by Kinloch [74], Johnsen [65] and Hsieh [66] concluded that the largest increase in toughness comes from the strain energy dissipation caused by plastic shear deformation due to the particulate inclusions. This plastic flow is a consequence of two deformation processes. The first is initiation and growth of multiple localized shear yield zones around the particles due to the stress concentration caused by the particle volume constraint. The second is the nucleation and growth of voids either due to cavitation of rubbery particles or debonding of rigid ones (see Figure 3-1). The energy associated with void formation is of little significance compared with the energy dissipated by the plastic deformation the voids enable. The extent of stress triaxiality is lowered due to the presence of these voids, thus lowering the stress needed for shear yielding of the adjacent matrix. This in turn further promotes the development of more localized plastic shear-bands.

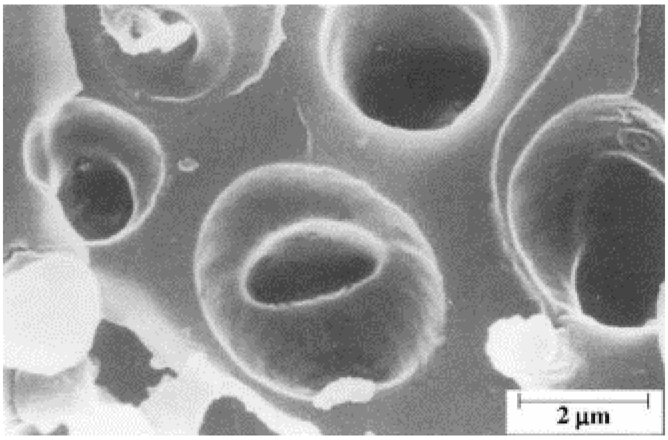

Figure 3-1. Scanning electron micrograph of the fracture surface of a rubber-filled epoxy. Cavitation of a rubbery particle can be observed [74].

Observations made on precursory work [8] performed on epoxy resins manufactured by the same industrial sponsor as this work support the thesis above as to the toughening mechanisms of particulate fillers. Details of the work can be found in [8], but an overview and most relevant findings is given next.

One control neat epoxy resin system was compared against two particle toughened systems of the same base resin. Cured resin cylinders with a diameter of 10 mm and a length-to-diameter ratio of 2:1 were tested under compression as per ASTM D695-10 [76]. Series of specimens were compressed to increasing levels of deformation and stereo-DIC was used to obtain deformation maps. Each test comprised of three stages (see Figure 3-2), namely

(A) compression to the desired level at constant displacement rate, (B) holding of the cross-head at this compression level for 10 min and (C) 30 min recovery after full load removal at the maximum admissible crosshead speed. Stress-strain curves were obtained from stage A, measures of anelastic deformation were taken from stage B and residual strain maps from stage C.

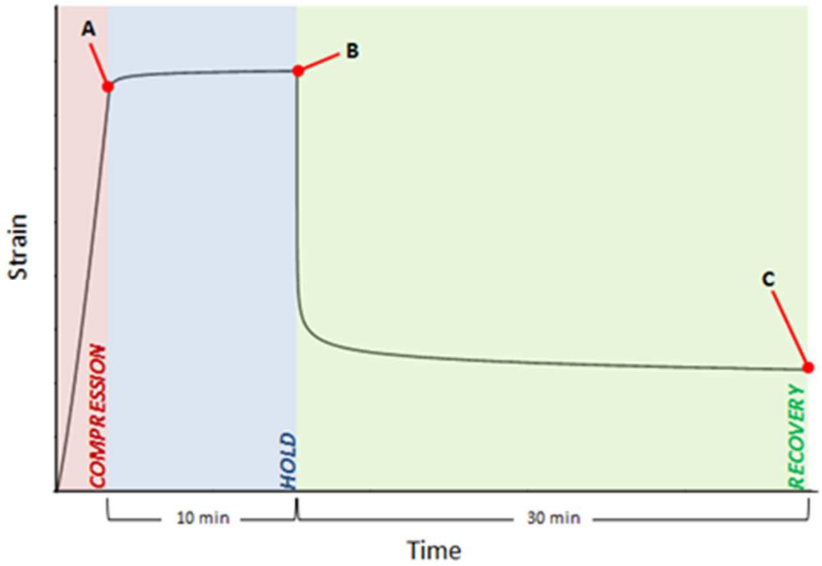

Figure 3-2. Compressive strain history showing end points of each load stage: A (compression), B (hold) and C (recovery).

Figure 3-3 shows the nominal stress-strain maps obtained from global measurements of the DIC datasets (left vertical axis) and the finding of the yield point for each system by back-extrapolation of non-zero residual strain specimens after the 30 min. It can be seen that the addition of particles lowers the strain needed to produce plastic deformation without significantly changing the elastic modulus. That is it lowers the onset of plastic flow in the matrix the energy dissipated from this translates into a tougher resin. Evidence of plastic shear band development around debonded particles was also found in one of the toughened systems as shown in Figure 3-4. The following section elaborates on how laminates are toughened by selectively filling the interlaminar regions with particles.

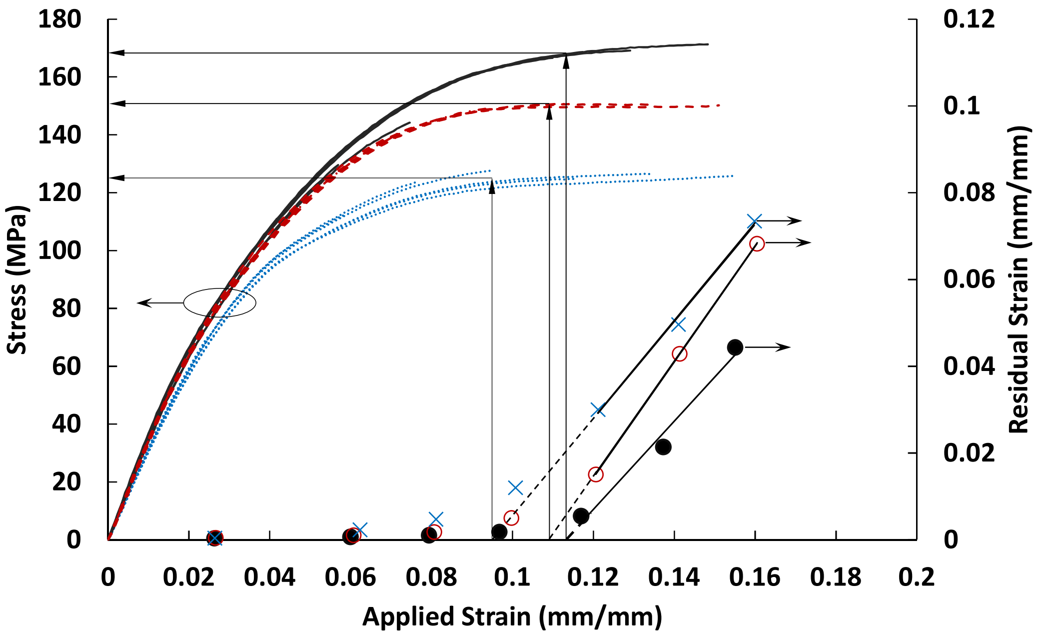

Figure 3-3. Yield point location for a neat epoxy resin (— , •) and two toughened resins (- - - , ○) and (· · · , ×) based on back-extrapolation of residual strain at 30 mins after unload [8].

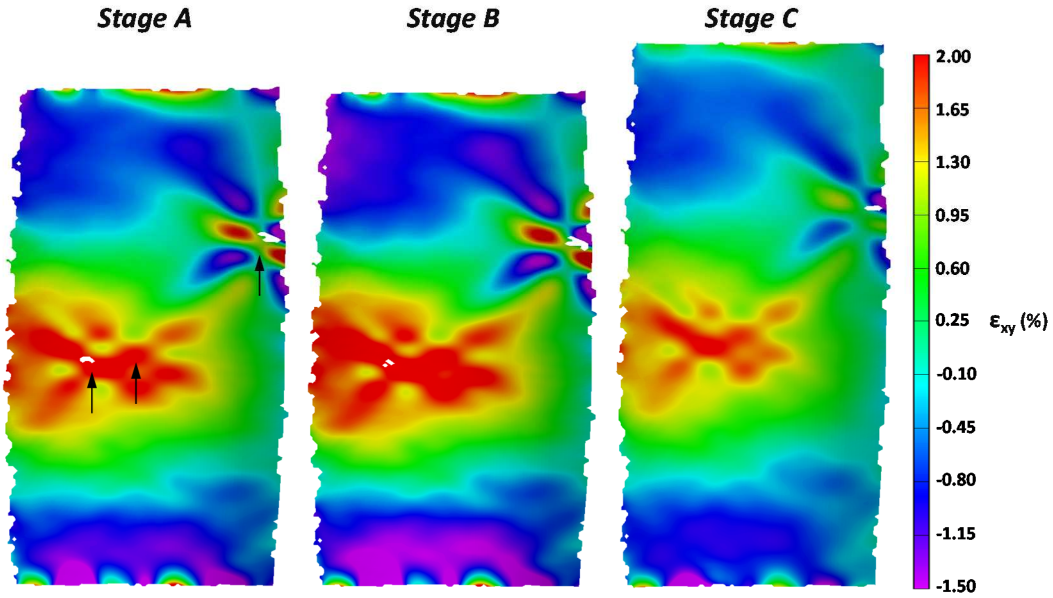

Figure 3-4. Maps of shear strain showing much localized plastic shear bands around what appears to be void growth resulting from debonded particles (arrows) in a toughened resin. Stage A corresponds to the end of loading at 18% of nominal longitudinal compression. Stage B captures the end of a 10 min hold of the compression level. Stage C shows the residual plastic shear deformation 30 min after removal of load [8].

3.3 Toughening of laminates by interleaving

The term interleaving refers to the selective inclusion of a tougher phase between plies in a laminate [77]. This is done with the intent to improve the interlaminar fracture toughness of the laminate by discouraging delamination which in turn improves the hot/wet compressive properties and the impact strength of laminates [78].

The two most conventional ways of interleave toughening in composite laminates are film intercalation [78], [79] and particulate filling of the resin rich regions [7], [80]. Latest developments have also explored the addition of nanofibers to the interlaminar regions [81], [82]. However, the focus of this work is on particle interleaving of the resin rich regions which is motivated by current development efforts of the industrial sponsor: Solvay Composites. In such systems the size of the particles (~4-30 μm in diameter) is larger than the interfibre distance when the prepreg cloth is produced. After stacking of the desired layup, the fibres act as a "strainer" during autoclaving to keep the particles in the resin rich regions. This is also the reason why particle interleaving is not a viable option for resin infusion processes as the fibres preclude the passage of the particles; the alternative for these kind of processes is the use of nanoparticles [64], [65], [67]. The effect of *micro*particle interleaving on the CAI performance of several proprietary material systems similar to the ones studied in this work have been investigated recently by researchers at the University of Southampton [9]–[14]; relevant findings are summarized next.

Studies by Bull et al [9], [10], [12] found that interleaving induced crack deflection by debonding of particles and crack bridging (ligament formation) by partially debonded ones. No apparent improvement in intralaminar matrix (splitting) cracking was found on toughened systems. The role of the particle/matrix interface in directing the crack path was highlighted by Borstnar et al. [13], namely, that a high interface strength will drive the crack into the ply instead of the resin rich region. This leverages from the low shear strength of the matrix and rather lowers the impact damage resistance. In contrast, moderate particle bonding will act to deflect the crack into the interlayer creating a tortuous path, thus increasing the energy expenditure for the crack to grow.

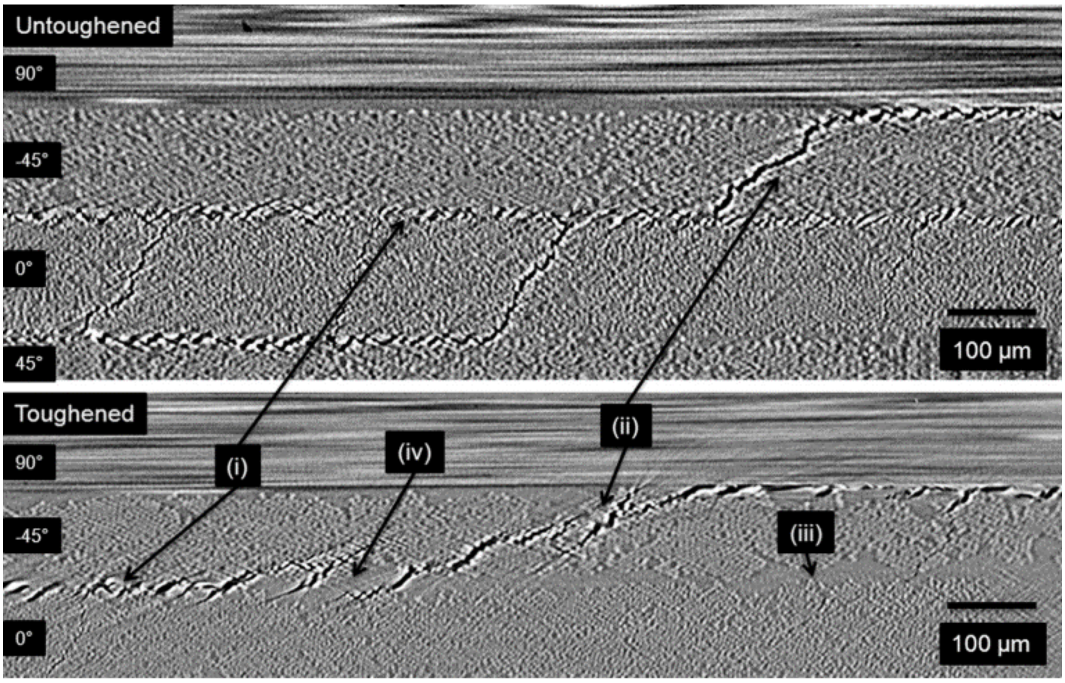

Figure 3-5. Comparison of cross-sections of low velocity impact damage in an untoughened vs toughened laminate with the same layup [+45/0/-45/90]$_{3S}$ at the same interfaces. (i) indicates delaminations, (ii) matrix crack, (iii) resin rich region and (iv) bridging ligaments [10].

3.4 Remark on motivation

This chapter discussed the advances made towards the manufacturing of more impact resistant composite laminates by means of toughening the interlayer regions. It is argued that improving the CAI performance is the principal motivation for increasing the matrix ductility. As such, most of the work found in literature concerning interleaving is related to low velocity impact. As a result there is extensive evidence of the benefits of a tougher interlayer in relation to resisting delamination, which is the driving damage mechanism of CAI.

On the other hand, findings from literature presented in Chapter 2 suggest that although OHC could benefit from a tougher matrix, delamination does not control failure of notched laminates; that is microbuckling. Moreover, since kink band formation is known to be an unstable process mainly dependent on matrix stiffness, the question arises as to what extent modifying the interlayer will affect the onset of microbuckling. Gaining this understanding is even more critical for the prediction of the durability of notched components, since impact damage is fortuitous but the introduction of notches is per design intent.

To the author's knowledge there is no study to date that addresses the effects of particle interleaving in notched laminates under compression. It is of interest to the industrial sponsor to elucidate and possibly quantify any differences in the static and fatigue performance of OHC coupons as a result of interleaving. The remainder of this thesis elaborates on the efforts made towards the satisfaction of said interest.

CHAPTER 4 MATERIALS AND TEST RIG

4.1 Material systems and specimen geometry

The materials used for this work consisted of developmental 16 ply panels with a quasi-isotropic layup $[\pm45/0/\mp45/90]_{2S}$ made from UD prepreg cloth. The primary reinforcement was a proprietary intermediate modulus carbon fibre (~5.4 μm) and the base matrix material was a thermoset epoxy resin. The panels were laid up by hand and cured by Solvay Composites using a standard 180°C aerospace autoclave cycle to produce ~3 mm laminates. One untoughened system (BL) was used as a baseline for comparison with three toughened systems (T1, T2 and T3) in static compression and with one toughened system (T3) in compression-compression fatigue.

For the toughened systems a particle-resin mixture was introduced to the surface of the prepreg following an initial wetting process of the fibres with the resin. Thus, after curing the particles were confined to the ~30 μm interlayer regions (interleaved) between each ply. The sizes of the secondary phase particles were in the order of 4 – 30 μm in diameter and the same particle to resin ratio (by weight) was used to form the matrix of the toughened systems. For all systems the same fibre to matrix (resin plus particles) ratio by weight was maintained. Also, the same carbon fibre and base resin was used for all materials. Therefore, it is sensible to assume that the lamina elastic properties are the same for all laminates; this for purposes of estimate calculations from classical lamination theory (CLT). The lamina manufacturer properties are shown in Table 4-1. Details of material composition are not provided due to proprietary restrictions.

Table 4-1. In plane ply properties from Solvay Composites. CTE is the linear coefficient of thermal expansion.

Elastic modulus (GPa)		**Shear modulus (GPa)**	**Poisson's ratio**	**CTE (10^{-6} K^{-1})**	
E_1	E_2	G_{12}	ν_{12}	α_{11}	α_{22}
163	8.4	4.7	0.33	0.42	39.50

Specimens for each system were cut to size from single panels to the geometry shown in Figure 4-2 using a precision circular saw and the loading ends were ground parallel within 70 μm. For the OHC coupons a circular hole of 6.35 mm diameter was machined at the centre of the specimen with a precision drill bit and liquid coolant to minimize machining damage. The same sizing was used for un-notched specimens of systems T1 and T2, which were used to validate the loading and extract laminate elastic properties to compare against classical lamination theory (CLT) predictions.

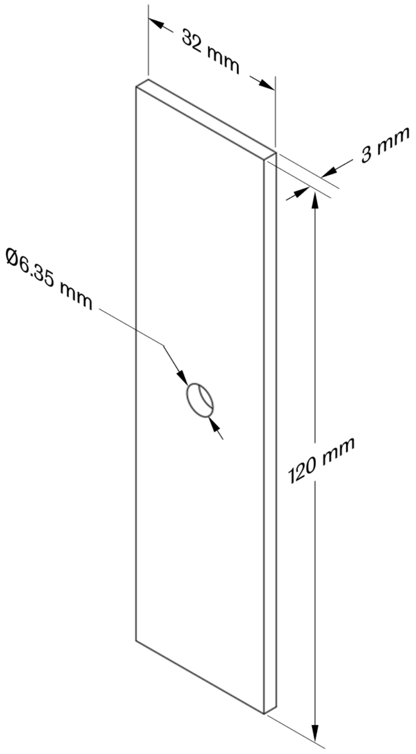

Figure 4-1. OHC specimen geometry

Although great care was taken during machining of the specimens it was found upon inspection under a microscope that the hole edges displayed damage at the 90° and 180° locations (as shown in Figure 4-2), which have been shown to be the most critical for OHC. No effort was made to characterize this damage or to quantify its contribution to experimental variability as it was out of the scope of the work. That is not to say that machining damage should be neglected, as it will be shown in Chapter 5 that hole quality, as visually gauged, has significant impact on the OHC strength.

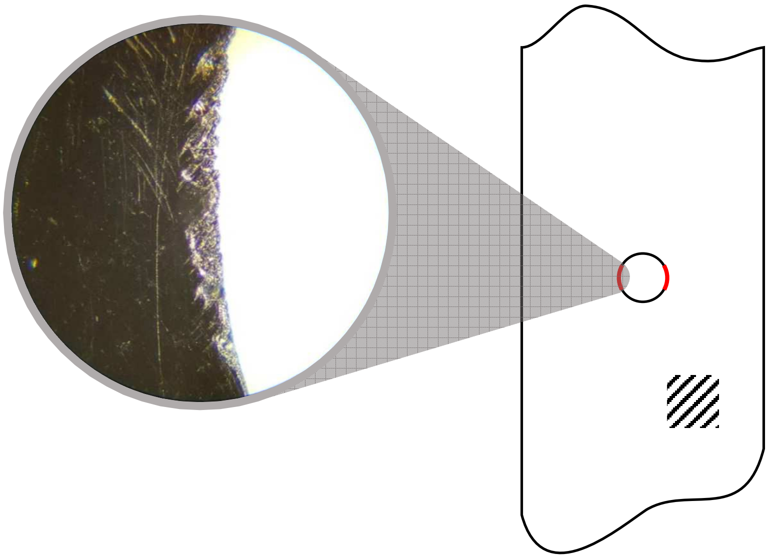

Figure 4-2. Micrograph of machining damage at the hole edge (120x).

4.2 Design of a compression fixture

A sizeable amount of effort was invested in the design of a fixture that would provide sufficient visual access to take advantage of the full field experimental techniques whilst still producing adequate loading conditions and acceptable failure modes. To meet this requirements, the following design criteria were defined for the desired fixture:

1. Provide unrestricted visual access to the whole width of the specimen.
2. Provide sufficient support to prevent Euler buckling of the gauge length, without the need for end-tabbing of the specimen.
3. Possess the ability to adjust and fix the clamping force on the specimen.
4. Maintain the alignment (parallelism) of the loading surfaces of at most the machining tolerances of the specimens.
5. Possess the capacity to support cyclic loading for extended periods.
6. Provide access for load-train independent instrumentation.

An assortment of test fixtures was investigated to find a potential base design; the most conventional fixtures are shown in Figure 4-3. It was found that established fixtures failed to provide sufficient visual access or had too many moving parts for dynamic testing to be viable.

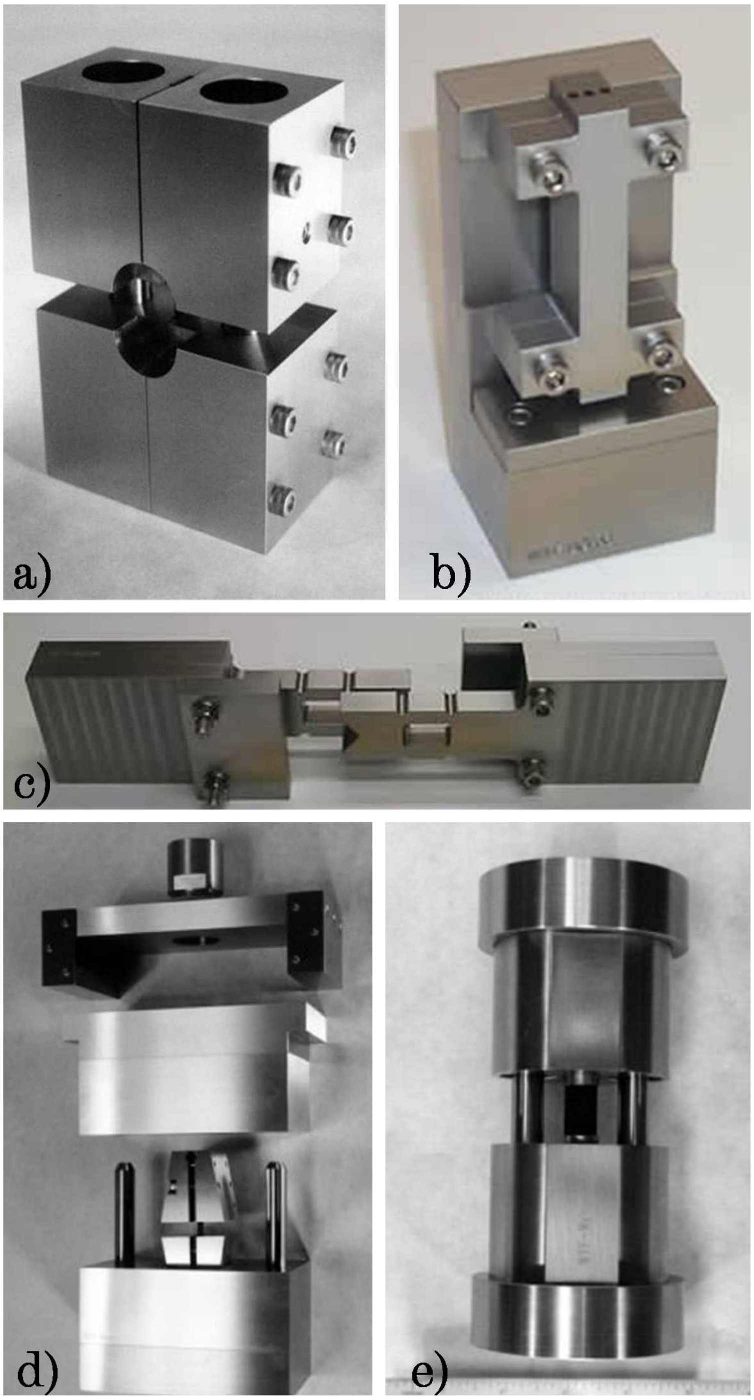

Figure 4-3. Conventional compression test fixtures[2]: a) CLC fixture as per ASTM D6641, b) Modified ASTM D695 fixture, c) OHC test fixture as per ASTM D6484, d) IITRI Compression Test Fixture as per ASTM D3410 and e) Wyoming Modified Celanese Fixture as per ASTM D3410.

The final design was based on Airbus standard AITM 1.0008 rev 3 (2004), which has been now superseded. Figure 4.4a shows the final design iteration with a

---

[2] All images are from https://www.wyomingtestfixtures.com/

specimen mounted. The fixture is comprised of a top and bottom loading plates guided by an assembly of 4 hardened shafts running on linear ball bearings. The specimens are simply supported to prevent Euler buckling by two sets (top and bottom) of clamps with polished faces, compression is applied by end loading and the visible specimen area is 32 mm^2 (see Figure 4-4b). Each clamp features a slotted tab that runs on square grooves machined on the loading plates and assembles a grounding screw. Clamping force can be adjusted by tightening a pattern of screws on each clamp set. The top plate is kept parallel by 4 linear bearings running on hardened shafts assembled to the bottom plate. All parts are made from 316 stainless steel, except for the hardened shafts which are 17-4 PH. Machining specifications for surface finish and dimensional tolerances are in accordance with ASTM D6484; detail drawings of the fixture can be found in Appendix A.

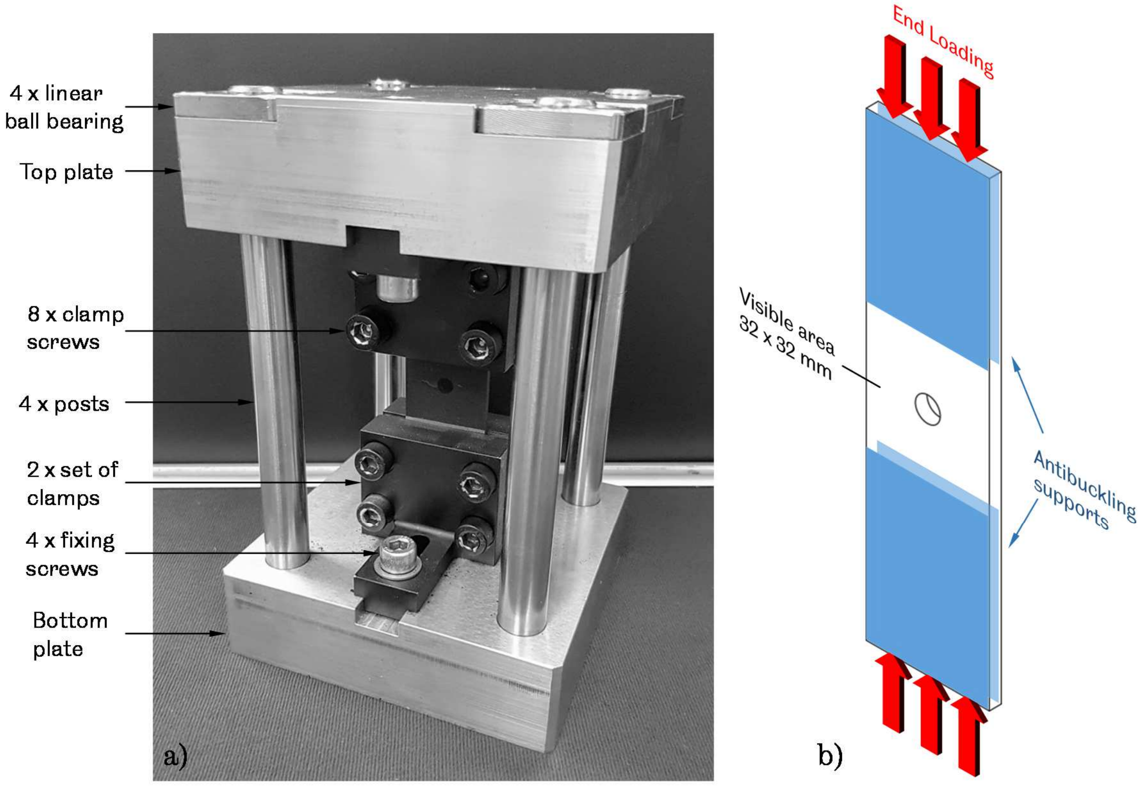

Figure 4-4 a) Compression fixture with specimen mounted; b) Loading conditions

4.3 Instrumentation and data acquisition

Testing was monitored and controlled using a 4 kHz servo-hydraulic controller connected to a 4-post single-actuator MAND machine fitted with a 100 kN load cell. Analogue data was captured from the load cell, a 100 mm LVDT attached to the actuator and a high accuracy (< 0.25% linearity) 3 mm LVDT mounted directly on the fixture. Thus, this last instrument was independent of load-train compliance. Analogue data was nominally acquired at 100 Hz for static tests and at each load cycle turning point, i.e. peak and trough for dynamic tests. Only data from the 3 mm LVDT and the load cell was used for the reporting of results.

CHAPTER 5 STATIC TESTING OF COMPOSITE LAMINATES

This chapter describes the application of 3D-DIC to static compression testing of notched laminates. The first section (5.1) provides an overview of the theory of digital image correlation. Then, details of the experimental arrangements and validation studies to obtain measures of uncertainty are provided in Section 5.2. Lastly, results from static testing of un-notched laminates are presented and compared against OHC specimens from the 4 systems investigated.

5.1 Principles of digital image correlation

Promoted by wider access to high-resolution digital cameras and low-cost computing power, the last three decades have seen DIC become an established noncontact experimental technique [83]–[87]. Although the technique has not displaced traditional instrumentation, e.g. strain gauges and extensometers, it has been increasingly favoured in material characterization testing due to its full field nature and set-up flexibility.

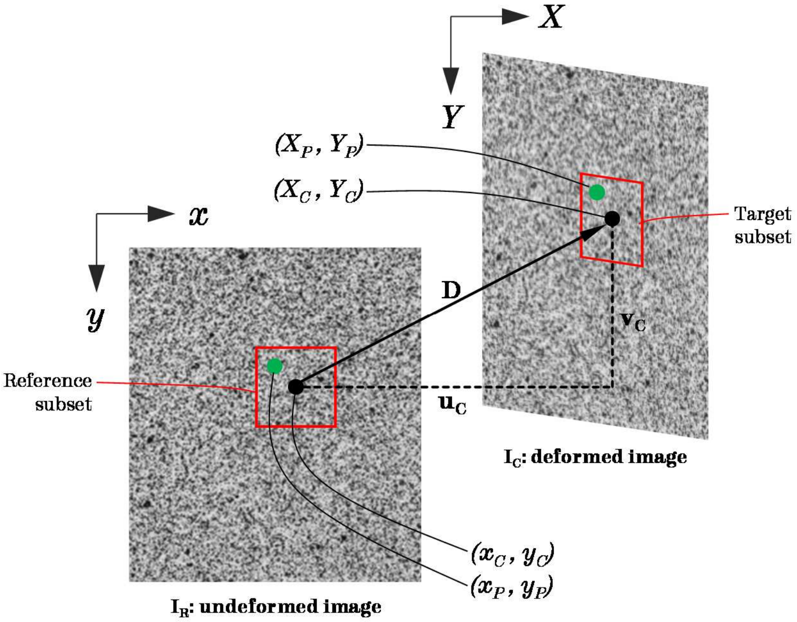

Figure 5-1. Basic principle of digital image correlation.

DIC refers to a collection of algorithms that use intensity variations in grey-value images to encode unique descriptors for particular image subsets in order to match the same points in image pairs and thus obtain a displacement field [88], as schematically illustrated in Figure 5-1. The intensity variation can be due to natural texture in an object, but more commonly it is from a random speckle pattern that is applied to the specimen before testing. The displacement gradient is then obtained by tracking the motion of image subsets between a reference image and current configurations (deformed) via cross-correlation of the subset pairs.

Table 5-1. Commonly used cross-correlation criterions

Cross-correlation criterion	Definition
Cross-correlation	$\mathrm{CC} = \sum_{i=-M}^{M}\sum_{j=-M}^{M}\left[f(x_i,y_j)g(X_i,Y_j)\right]$
Normalized cross-correlation	$\mathrm{NCC} = \sum_{i=-M}^{M}\sum_{j=-M}^{M}\left[\frac{f(x_i,y_j)g(X_i,Y_j)}{\bar{f}\bar{g}}\right]$
Zero normalized cross-correlation	$\mathrm{ZNCC} = \sum_{i=-M}^{M}\sum_{j=-M}^{M}\left\{\frac{\left[f(x_i,y_j)-f_m\right]\times\left[g(X_i,Y_j)-g_m\right]}{\Delta f\Delta g}\right\}$

Table 5-2. Commonly used sum of squared differences criterions

Sum of squared differences criterion	Definition
Sum of squared differences	$\mathrm{SSD} = \sum_{i=-M}^{M}\sum_{j=-M}^{M}\left[f(x_i,y_j)-g(X_i,Y_j)\right]^2$
Normalized sum of squared differences	$\mathrm{NSSD} = \sum_{i=-M}^{M}\sum_{j=-M}^{M}\left[\frac{f(x_i,y_j)}{\bar{f}}-\frac{g(X_i,Y_j)}{\bar{g}}\right]^2$
Zero normalized sum of squared differences	$\mathrm{ZNSSD} = \sum_{i=-M}^{M}\sum_{j=-M}^{M}\left[\frac{f(x_i,y_j)-f_m}{\Delta f}-\frac{g(X_i,Y_j)-g_m}{\Delta g}\right]^2$

In principle, it is desired to compute the displacement vector D of an arbitrary point C inside the region of interest (ROI) to be analysed. Thus, a particular subset of $(2M+1)\times(2M+1)$ pixels[2] and centred at (x_C, y_C) in the reference or undeformed image is selected and used to track the corresponding position of P in the deformed image (X_C, Y_C). The tracking is realized by maximization of a cross-correlation coefficient or minimization of a sum of squared differences coefficient [89]. Common definitions of correlation scores are shown in Table 5-1, where

$$f_m = \frac{1}{(2M+1)^2} \sum_{i=-M}^{M} \sum_{j=-M}^{M} f(x_i, y_j), \qquad g_m = \frac{1}{(2M+1)^2} \sum_{i=-M}^{M} \sum_{j=-M}^{M} g(X_i, Y_j),$$

$$\bar{f} = \sqrt{\sum_{i=-M}^{M} \sum_{j=-M}^{M} [f(x_i, y_j)]^2}, \qquad \bar{g} = \sqrt{\sum_{i=-M}^{M} \sum_{j=-M}^{M} [g(X_i, Y_j)]^2},$$

$$\Delta f = \sqrt{\sum_{i=-M}^{M} \sum_{j=-M}^{M} [f(x_i, y_j) - f_m]^2}, \qquad \Delta g = \sqrt{\sum_{i=-M}^{M} \sum_{j=-M}^{M} [g(X_i, Y_j) - g_m]^2}.$$

and f and g refer to the reference and target subsets, respectively.

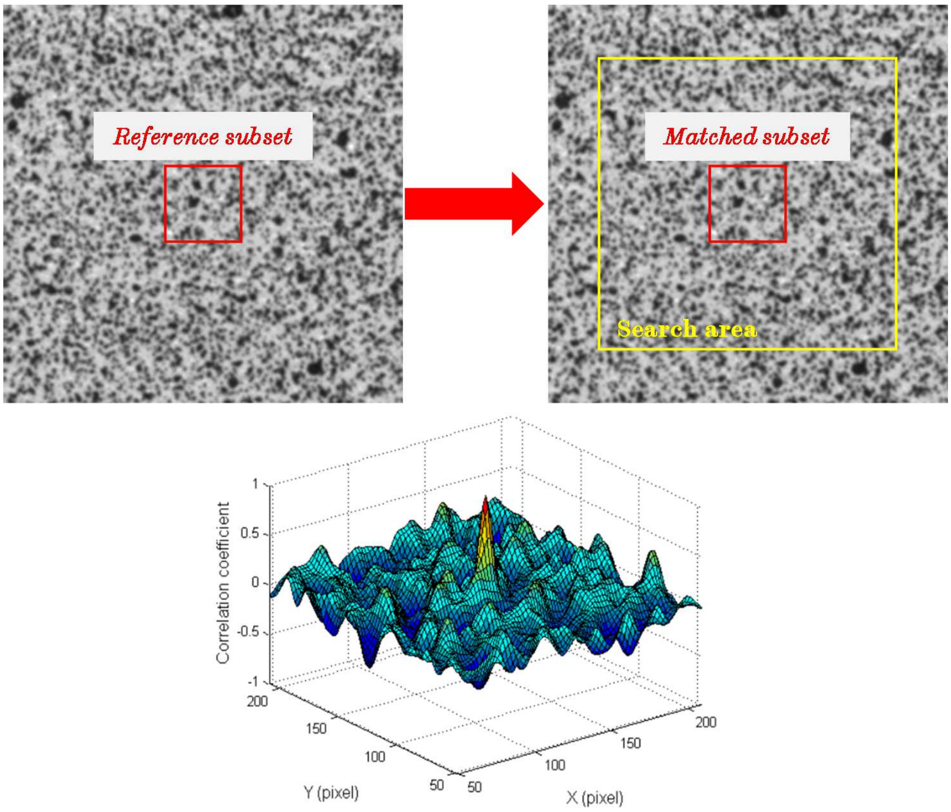

Figure 5-2. Example of cross-correlation coefficient distribution over the search area surrounding the reference subset.

Typically one of the criteria in Tables 5-1 and 5-2 is selected based on experimental conditions (e.g. illumination) and processing cost; the criteria are listed by increasing robustness and, consequently, processing time. The in-plane displacement components are then computed from finding the position of the extremum of the predefined coefficient within a search area comprised of several candidate subsets (see Figure 5-2).

In order to map a set of neighbouring points in the reference subset to their corresponding positions in the target subset a so-called shape or displacement mapping function is used; this is based on the assumption of a continuous deformation field [15]. Consider then a point P around the subset centre (x_C, y_C) in the reference image. The coordinates (x_P, y_P) can then be mapped to the target subset as:

$$X_P = x_P + \xi(x_P, y_P) \qquad (1)$$
$$Y_P = y_P + \eta(x_P, y_P)$$

where the mapping functions ξ and η can be prescribed with increasing order depending on the complexity of the deformation field. Namely, zeroth-order functions can only map rigid body translations, i.e.

$$\xi_0(x_P, y_P) = u \qquad \eta_0(x_P, y_P) = v \qquad (2)$$

Then, the more common first-order or affine functions allow translation and rotation displacements, and shear and normal strains and linear combinations of these, as:

$$\xi_1(x_P, y_P) = u + \frac{\delta u}{\delta x}\Delta x + \frac{\delta u}{\delta y}\Delta y \qquad (3)$$
$$\eta_1(x_P, y_P) = v + \frac{\delta v}{\delta x}\Delta x + \frac{\delta v}{\delta y}\Delta y$$

For finite deformations the affine shape functions may be insufficient and higher-order mapping functions may be necessary to accurately resolve the displacement field. Thus, a second-order shape function is defined as:

$$\xi_2(x_P, y_P) = u + \frac{\delta u}{\delta x}\Delta x + \frac{\delta u}{\delta y}\Delta y + \frac{1}{2}\frac{\delta^2 u}{\delta x^2}\Delta x^2 + \frac{1}{2}\frac{\delta^2 u}{\delta y^2}\Delta y^2 + \frac{\delta^2 u}{\delta xy}\Delta x\Delta y \qquad (4)$$
$$\eta_2(x_P, y_P) = v + \frac{\delta v}{\delta x}\Delta x + \frac{\delta v}{\delta y}\Delta y + \frac{1}{2}\frac{\delta^2 v}{\delta x^2}\Delta x^2 + \frac{1}{2}\frac{\delta^2 v}{\delta y^2}\Delta y^2 + \frac{\delta^2 v}{\delta xy}\Delta x\Delta y$$

The nomenclature of above equations is that u and v are the directional displacement components, $\Delta x = x_P - x_C$ and $\Delta y = y_P - y_C$.

As it may be the case that the coordinates of (X_P, Y_P) in the target subset locate between pixel centres, a sub-pixel interpolation algorithm is needed in order to resolve the displacement accurately. Details of commonly used interpolation algorithms are given in Schreier et al. in [90]. Thus, the matching of subsets in the image sequence yields the sub-pixel displacement field for which common algorithms for the initial guess of deformation and the calculation path are described by Pan et al. in [89]. In order to obtain strain measurements, the displacement gradient is calculated via numerical differentiation according to the strain definition that is deemed appropriate for the deformation levels of the image sequence. However, as numerical differentiation of the displacement field tends to amplify noise, displacement maps are typically smoothed before calculating strains by use of penalty finite element method as proposed by Sutton et al. [91] or a pointwise least squares algorithm advocated by Pan et al. in [92]. Additional to the smoothing of displacements, a strain window (virtual strain gauge or VSG) needs to be defined to further reduce noise from the spatial differentiation operation and this is done at the expense of the capacity to resolve strain gradients. Therefore, a compromise between noise and strain resolution always needs to be made.

The set of high-level steps laid out above describe the general procedure for in-plane or 2D-DIC. However, 2D-DIC requires high parallelism of the imaging sensor with the test surface and negligible out-of-plane displacements to minimize the systematic error in the measurements making its use relatively limited. Sutton et al. [93] show that one way to circumvent these limitations, if there is only access to a single camera, is to use a telecentric lens. However, since the cost of a telecentric lens will normally outweigh the procurement of an additional camera with sufficient resolution for most applications making the use of stereo- or 3D-DIC a better option, this, with the added benefit of being able to measure out-of-plane displacements.

A 3D-DIC system features at least two synchronized cameras registering images of the same area in an object (scene). This is known as a stereovision system, whereby, setting the cameras non-coincident, a 3D description of the scene can be obtained. As shown in Figure 5-3, two imaging sensors are set at a angle in the world coordinate system (y_W, z_W, x_W) to register a particular point P_W at each optical (or sensor) centre, O_{c1} and O_{c2} with coordinates (x_{c1}, y_{c1}, z_{c1}) and (x_{c2}, y_{c2}, z_{c2}), respectively. Then based on a pinhole model [15], each camera performs perspective projection to transform the world coordinates of P_W into the corresponding image points P_1 and P_2, and thus, the collection of points registered from the scene make up each image I_1 and I_2. It is therefore possible to recover the position of P_W triangulation [94] of P_1 and P_2 after calibrating the camera set.

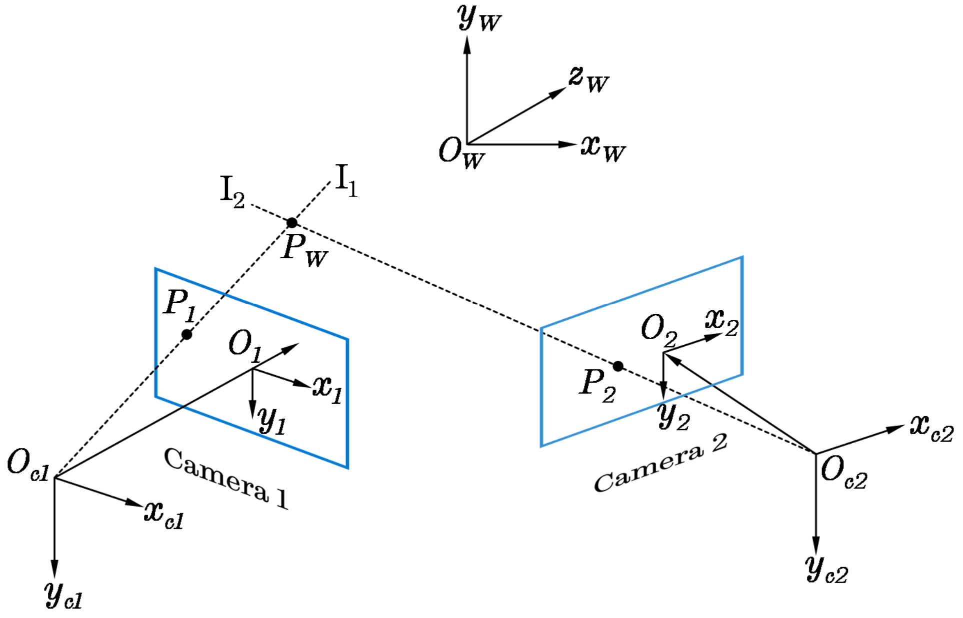

Figure 5-3. Schematic of a stereo vision model.

Calibration is the process of orienting and scaling the image planes relative to the world. This is accomplished by determining the *intrinsic* and *extrinsic* parameters for every pair of cameras. The former relate each camera to the world, and the latter relate the cameras to one another. The extrinsic parameters are needed for triangulation of world point positions with reference to the camera coordinate system. Intrinsic parameters include: sensor centre coordinates, focal length, image skew and lens geometric distortion. Extrinsic parameters are the camera world coordinates and relative orientation. Calibration is typically done by acquiring several images of a pattern with known geometry to find the camera parameters using a minimization method [95].

After calibration of the camera set, the first capture is used to recover the 3-dimenstional surface of the object to be tracked to create the reference image, as illustrated in Figure 5-4. Temporal tracking of subsequent (target) image stereo-pairs is then performed using the chosen correlation algorithm and the 3-dimensional reconstruction is done by triangulation of each capture.

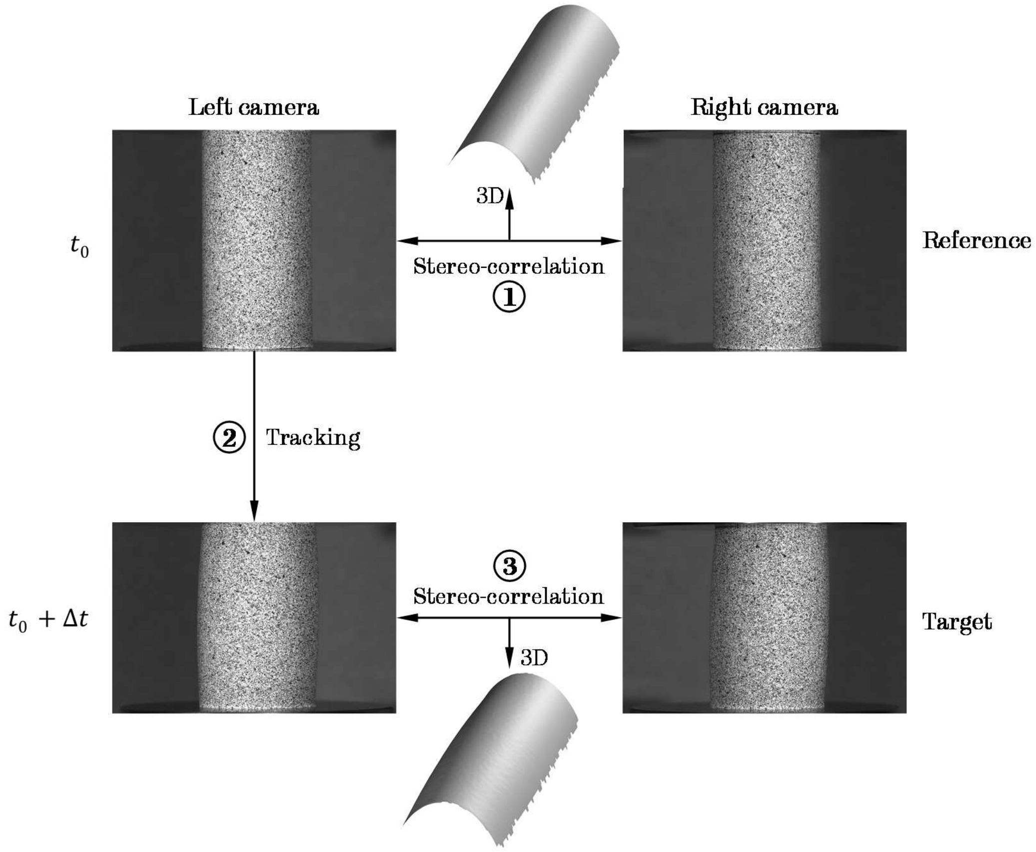

Figure 5-4. Schematic of typical 3D-DIC process.

The tracking algorithm to be used depends on the application. For objects undergoing small deformation at each capture, the use of an initial reference image is appropriate. However, if the surface being tracked undergoes large finite deformation, e.g. granular media or elastomers, errors can result from poor correlation [96] or pattern degeneracy [97]. In this instances, an incremental method is more appropriate, using each capture as a reference for the next [97], [98].

5.2 Experimental Setup

5.2.1 3D – DIC rig for static testing

The rig used to perform static testing is shown in Figure 5-5 and the specifications and settings of the DIC system are given in Table 5-3.

Two 5 Megapixel (pixel size = 3.45 μm^2) monochrome CCD cameras with a grey-depth of 2^8 levels were fitted with f2.8 50 mm lenses and set at an angle β facing the specimen. The cameras were connected to a computer via an IEEE 1394b interface. Analogue data was acquired from the servo-controller and synchronized to the image capture using a National Instruments USB-6211 DAQ.

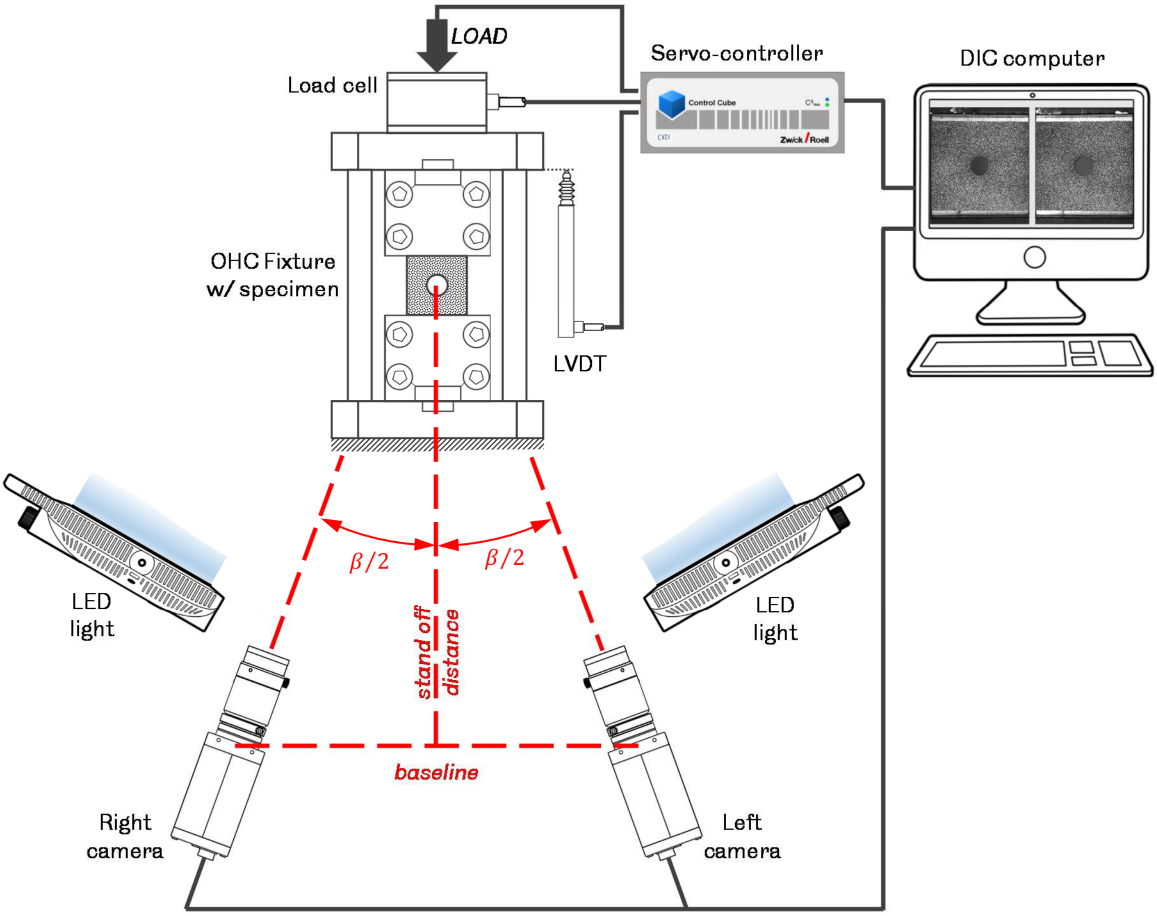

Figure 5-5. Schematic of stereo-rig used for static OHC tests.

The visible specimen area was illuminated via a pair of high-intensity LED panels with the colour temperature set the closest possible to the CCD sensor's peak quantum efficiency wavelength (~500 nm). The depth of field was increased as much as possible to make full use of the sensor's dynamic range whilst keeping a low exposure time (< 50 μs) to minimize motion blur. Magnification was set so that the ROI was 80% of the sensor, maximizing spatial resolution but preventing optical distortion due to vignetting.

The DIC software used was VIC-3D, version 8.0.4 from Correlated Solutions Incorporated[3]. The subset and step sizes were specified to maximize displacement resolution with a mean uncertainty interval of 0.01 pixel [95] after correlation of 10 static captures. Cross-correlation was performed by minimization of a normalized sum-of-squared-differences criterion using an affine shape function to map subset deformation. An optimized 8-tap interpolator was selected to approximate subpixel intensities. The strain computation was performed using the Green-Lagrange tensor since the largest strain level is $\epsilon < 1\%$ and filtering displacement data with a 15 × 15 window. This corresponds to a virtual strain gauge size of 1.81 mm.

Table 5-3. Stereo-rig specifications and DIC settings.

Cameras and digitization	2 × AVT Pike F-505 (8-bit, 2452 × 2054)
Lenses	2 × Schneider Apo-Xenoplan 2.8/50
Lighting	2 × Alphatron Tristar 4
Magnification	~ 55 px/mm (18.2 μm/px)
Subset size	29 × 29 px
Step size	7 px
Strain window size	15 points
Virtual strain gauge	99 px (1.81 mm)
Spatial resolution	127 px (2.32 mm)
Shape function	Affine
Interpolation	Optimized 8-tap
Correlation function	NSSD

Calibration was performed using 50 images of random translations and rotations of a planar dot pattern with a size ~90% of the sensor. The typical calibration parameters for the static tests are shown in Table 5-4, were C_x and C_y are the centre locations of the image plane in pixels, $f\lambda_x$ and $f\lambda_y$ are the scaled focal lengths in pixels, skew is the deviation from orthogonality

---

[3] Correlated Solutions, Inc., 121 Dutchman Blvd., Irmo, SC 29063 – USA; url: www.correlatedsolutions.com.

between the row and column directions in the sensor plane, κ_1 is the radial distortion coefficient and κ_1^{norm} is the normalized distortion factor. More rigorous definition of this parameters can be found in [88].

The right-most columns of Table 5-4 are the extrinsic parameters that relate the cameras. Most notably, a stereo-angle of $\beta \approx 20°$ was used as it offers a good balance of in-plane and out-of-plane displacement resolution [95].

Table 5-4. Typical calibration parameters of stereo-rig.

Parameter	Camera 1	Camera 2	Camera 1 → 2 transformation	
C_x	1214 px	1208.86 px	α	-0.264°
C_y	1051.89 px	978.783 px	β	19.354°
$f\lambda_x$	17326 px	17320.7 px	γ	-0.200°
$f\lambda_y$	17326 px	17320.7 px	T_x	-107.022 mm
Skew	0	0	T_y	0.277 mm
κ_1^{norm}	-1.634e-5	-2.144e-2	T_z	17.5947 mm
κ_1	1.2898	4.0778	Baseline	108.459 mm

5.2.2 Optimization of the speckle pattern

The characteristics of the speckle pattern applied to the objects tracked with DIC have substantial impact on the uncertainty of the measurements [99] and thus it is paramount to understand how to tailor it insofar as the requirement for uniqueness of the subsets is still met. The most conventional form of application of speckles is via spray painting as it is deemed more convenient than speckling by hand or using an airbrush. However, great care must be exerted in producing the best possible speckle pattern for the current calibration to obtain high quality measurements, i.e. high displacement resolution with low uncertainty.

Several authors have proposed metrics that attempt to quantify the quality of the speckle patterns, as recently reviewed by Dong and Pan [100]. However, in practice, the random nature of spray painting and the large number of variables influencing paint deposition, e.g. user experience, distance to object vs paint atomization, ambient temperature and humidity, make the application of a consistent pattern, let alone optimal, very difficult.

It was therefore desirable to investigate different patterns, as shown in Figure 5-6 with their grey level histograms, to arrive at the best practicable application of speckles. To get a variety of patterns, an assortment of spray caps from Montana Cans[4] was tested. A thin coat of matt white spray paint was applied on flat steel plates of the same dimensions as the ROI in the composite specimens and 8 different spray caps were used to produce 16 patterns, 2 from each cap to evaluate consistency between applications of the pattern. Then, 10 static images of each pattern were acquired and correlated using the same settings selected for the composite tests.

The following guidelines were used to produce and judge the candidate speckle patterns obtained with different spray caps, as shown in Figure 5-6:

- The speckle size distribution should tend to 5×5 pixel^2, with speckles of no less than 3×3 pixel^2.
- Speckle density should be homogeneous across the ROI.
- The speckle-to-background coverage ratio should be 1:1.
- The grey level distribution should be bimodal, indicating good contrast between speckles and background.
- Application of the pattern with the same cap should be consistent.

Noise floor statistics were obtained from the correlation of the static image sets. This is widely acknowledged as a heuristic metric that can provide a good approximation of the error in the DIC measurements [101], [102]. Thus, the mean and standard deviation of the displacements and strains from each ROI was extracted for the 16 datasets, as shown in Figure 5-7. Patterns SKA and LC6 were found to be the best based on the guidelines described above and due to producing the lowest standard deviation, which is taken here as the noise floor. From this, measures of displacement and strain resolution were obtained (see Table 5-5) without the consideration of the additional bias error likely to be introduced during actual testing.

---

[4] url: https://www.montana-cans.com/

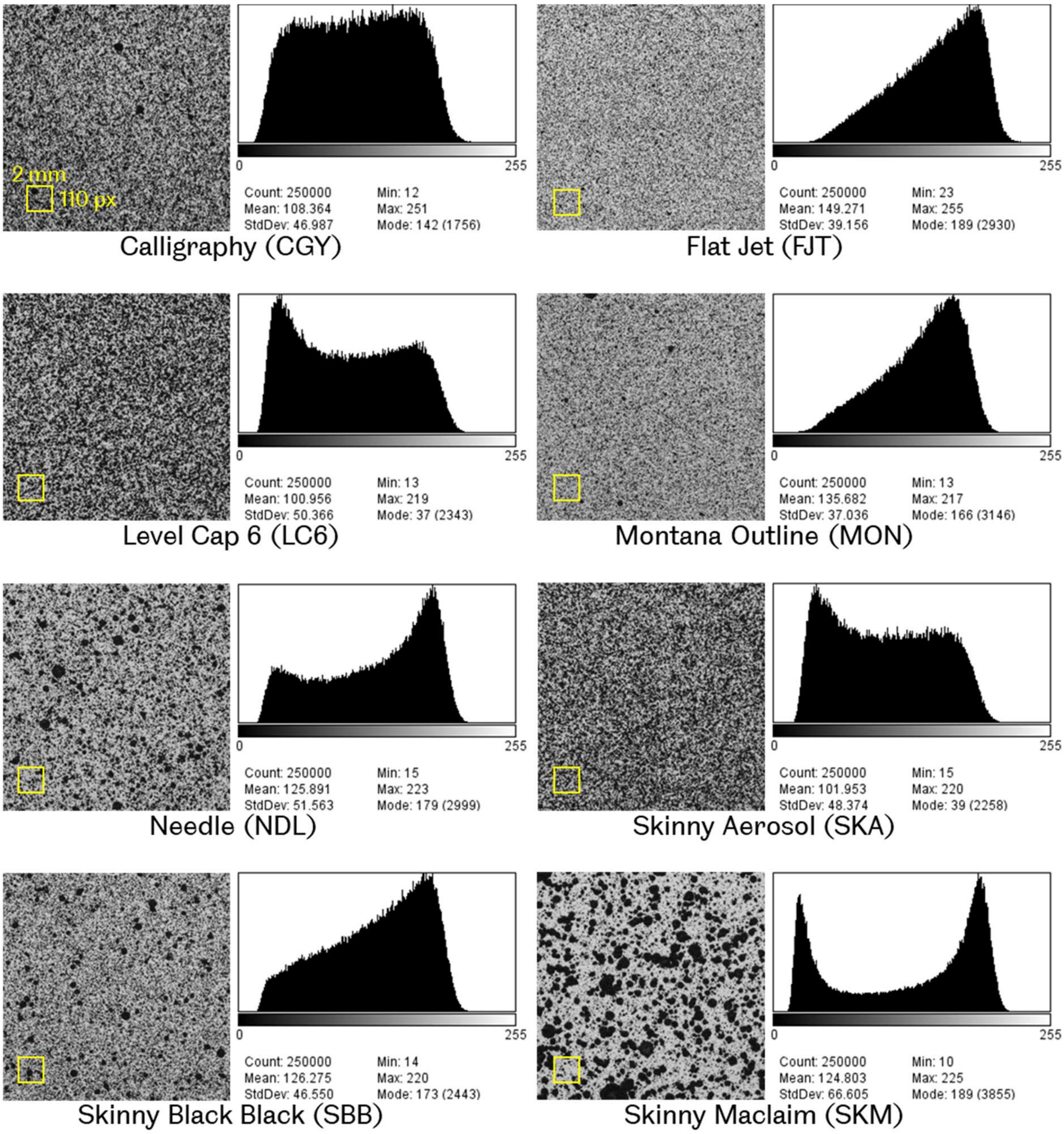

Figure 5-6. Speckle patterns investigated and their corresponding grey level histograms. Scale and magnification is indicated by the inset squares. The patterns are identified as in the Montana Cans catalogue.

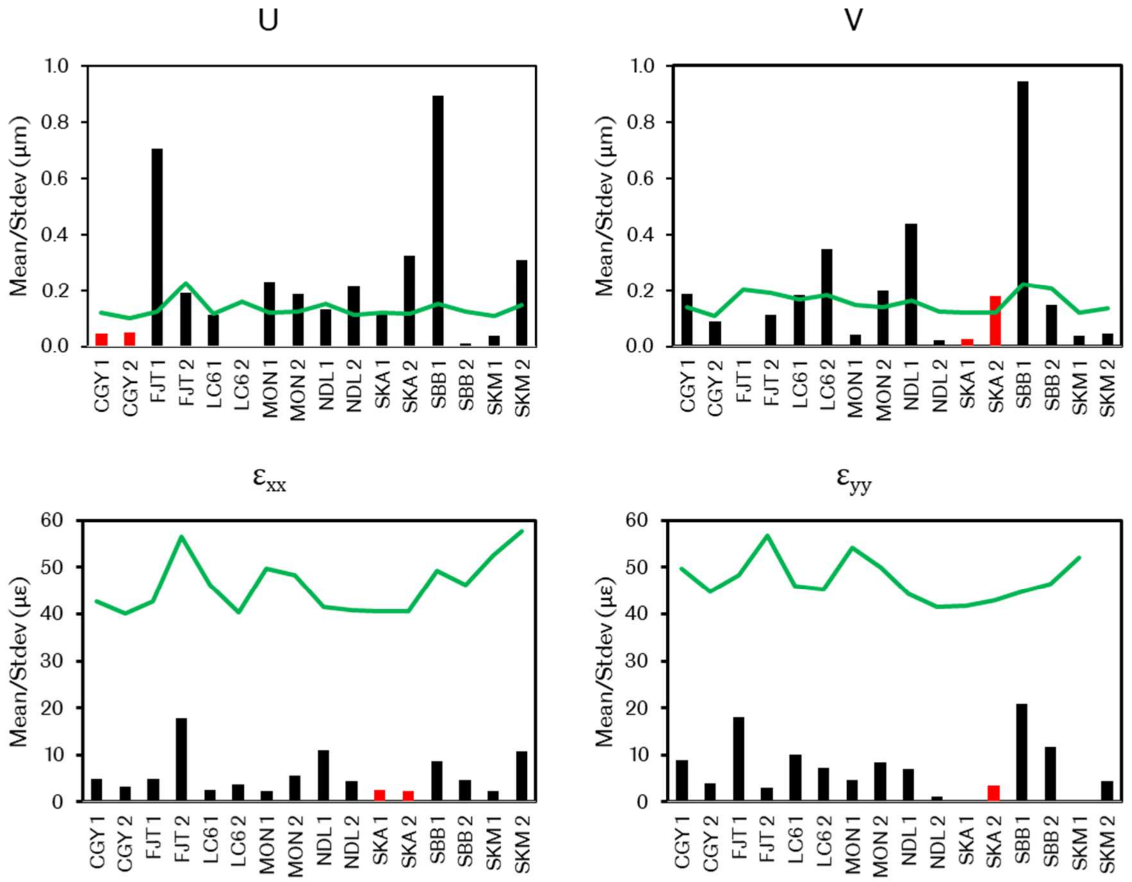

Figure 5-7. Average noise floor of 10 static images of each candidate speckle pattern. The bars indicate mean values and lines standard deviation.

Table 5-5 Displacement and strain resolution of typical SKA speckle pattern

Resolution	10-image noise floor
Displacement	$< 0.15\ \mu m$
Strain	$< 45\ \mu\epsilon$

5.2.3 Validation of the OHC test rig

Loading conditions were validated in accordance with ASTM standard practices E4 and E467 and from this the error in the load application was found to be less than 0.2% of the full scale of the load cell for both static and dynamic loading. Displacement maps were obtained with 3D-DIC from static tests of notched and un-notched specimens to observe the development of Euler buckling of the specimens and to verify that load application was even in the transverse direction.

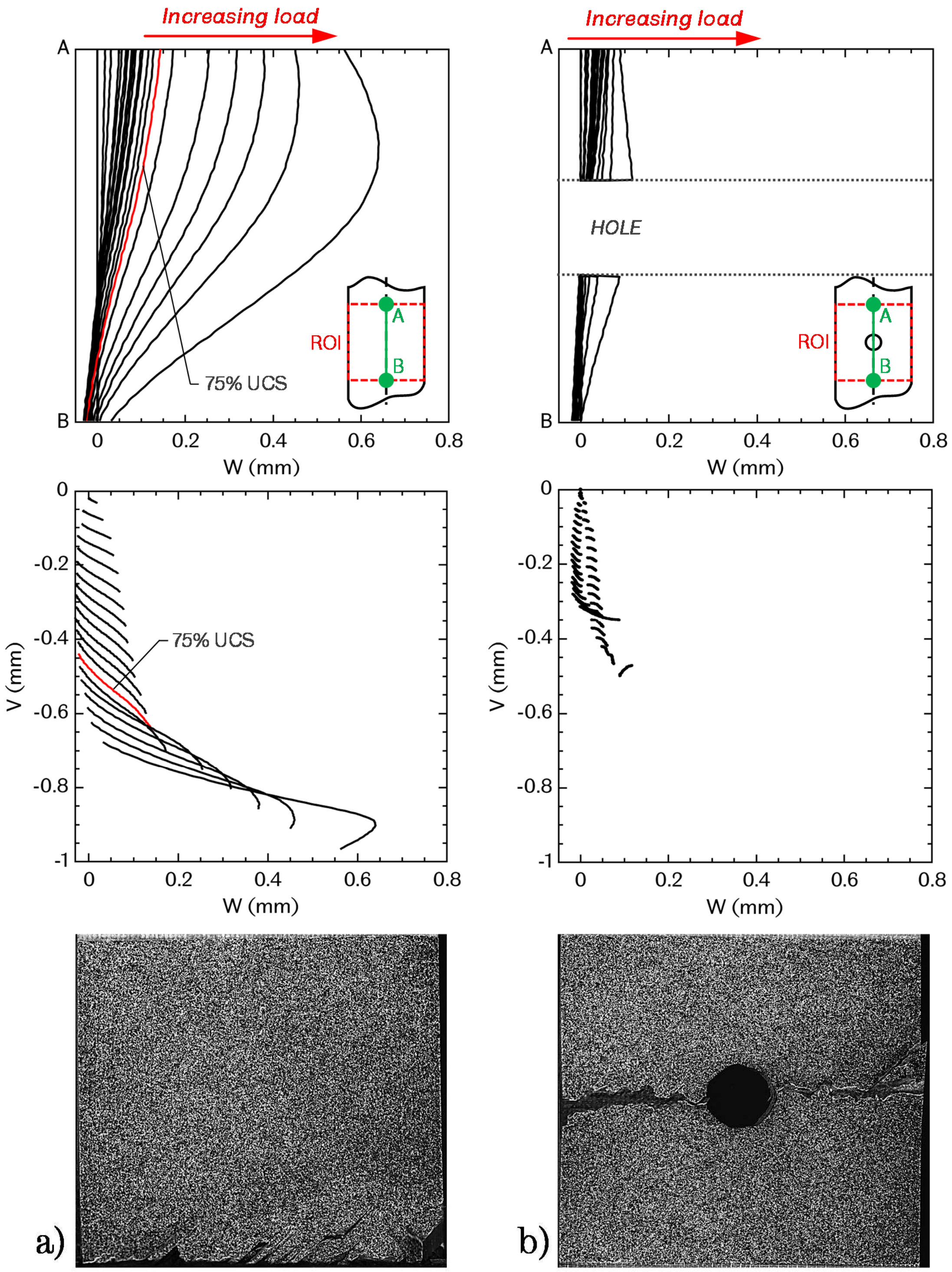

Figure 5-8. Out-of-plane displacement W profiles (top) of the ROI median line (inset), axial V vs out-of-plane W displacement plot (middle) and failed specimens (bottom) for an un-notched (a) and a notched (b) specimens.

Specimens were loaded to failure at a nominal displacement rate of 1 mm/min, in accordance with ASTM D6641 and D6484. After correlation, 200 points sampled from a median line (*AB*) parallel to the load axis were used to construct profiles of the out-of-plane displacement W, as shown at the top of Figure 5-8. The middle row of Figure 5-8 shows plots of axial (parallel to load axis) displacement V vs. W for each sample point on the *AB* line. Failed specimens are shown at the bottom row of Figure 5-8.

It can be seen then that the un-notched specimen undergoes large Euler buckling at loads F above ~75% of the failure load F_{ult}, with W becoming large in comparison with V. This may be caused by a small mismatch between the top and bottom clamps due to accumulated manufacturing tolerances which facilitates buckling, forcing the specimen to fail at the bottom clamp due to concentration of flexural stresses. Conversely, the notched specimen displays almost in-plane deformation along *AB* and fails laterally across the centre of the hole, which is an acceptable failure mode under ASTM D6484. It is concluded then that loading conditions are valid for OHC tests up to failure, but only at $F < 0.75F_{ult}$ for un-notched specimens.

5.2.4 Experimental method

Due to material availability, only un-notched specimens of the T1 and T2 systems were tested under static compression. It is assumed that since specimens from all systems have the same layup and the same base resin, the elastic response is the same. Further, it has been shown in [8] that the effect of the similar particulate fillers on the base resin's modulus is negligible. Also, as the particles are contained within the interlayer regions, the in-plane properties of the plies are left relatively unchanged across laminate systems. As such, it is argued that the aforementioned assumption is valid.

The UN static tests were performed on 6 specimens, 3 from each system, in accordance with ASTM 6641. In turn, 16 open-hole specimens, 4 from each material system, were compressed to failure in accordance to ASTM 6484. Load for all tests was applied in displacement control and analogue data was acquired from the load cell and the 3mm LVDT. The DIC capture rate for static tests was set to 0.5 fps at loads below 90% of the anticipated failure point, as obtained from preliminary testing, and increased to 5 fps until failure.

5.3 Results

5.3.1 Compression of un-notched specimens

A typical axial stress σ_{yy} vs axial strain ϵ_{yy} curve is shown in Figure 5-9 left plot, with

$$\sigma_{yy} = \frac{F}{A_0} \qquad\qquad \epsilon_{yy} = \frac{E_L + E_0 + E_R}{3} \tag{5}$$

where A_0 is the unloaded area at the centre of the specimen, E indicates a virtual extensometer used to extract axial strain and the subscripts L, 0 and R denote the position along the width of the ROI.

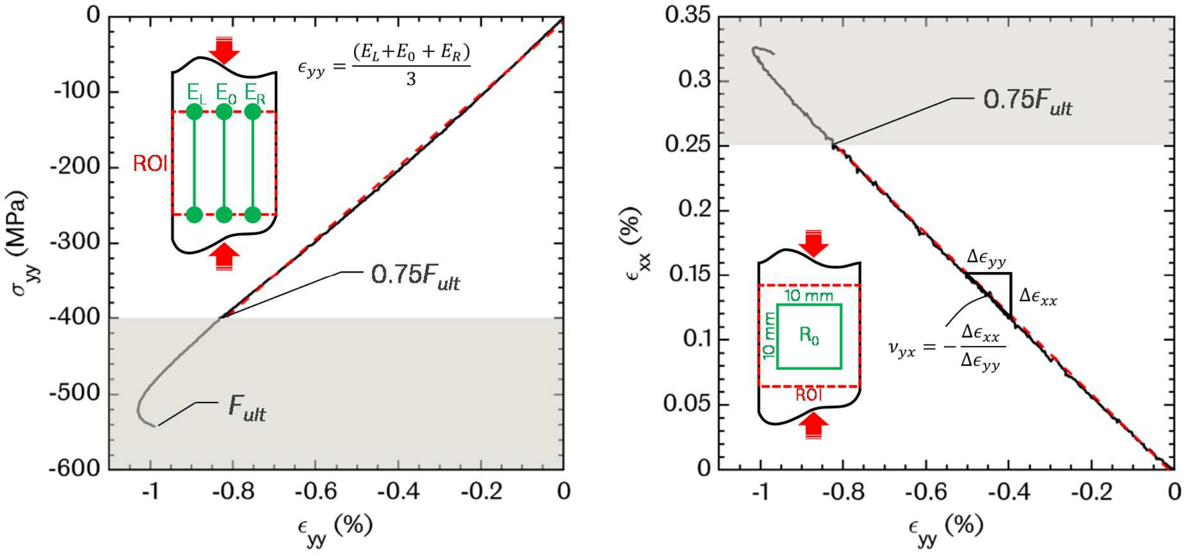

Figure 5-9. Typical stress-strain response (left) and Poisson's ratio (right) of an un-notched coupon under compression. The insets describe the interrogation methods to extract the curves, namely, an average of 3 virtual extensometers (E_L, E_0 and E_R) for σ_{yy} vs ϵ_{yy} and an average of a rectagular area R_0 for ν_{yx}.

It can be seen that although specimens undergo some deflection, the response is linear up to ~$0.75F_{ult}$ but for a slight concavity of the curve likely caused by the flexural deformation softening the in-plane compliance. As a result, a robust linear least squares fit of $0 < F \leq 0.75F_{ult}$ may underestimate the in-plane axial modulus. Conversely, Poisson's ratio ν_{xy} remained nearly constant over the same interval, as shown in the right plot of Figure 5-9. The average of a 10×10 mm^2 area at the centre of the ROI was used to extract and fit ν_{yx} to avoid the acute transverse strain ϵ_{xx} gradients at the edges due to ply ν_{yx} mismatch. Figure 5-10 shows ϵ_{yy} and ν_{yx} maps where it can be seen that the strain state is relatively homogeneous up to $0.75F_{ult}$. The acute strain gradients at the edges of the specimen can be seen from the Poisson's ratio, hence the use of the central area R_0 of the ROI to extract data. The in-plane strain softening caused by gross flexure of the laminate at imminent failure can also be seen.

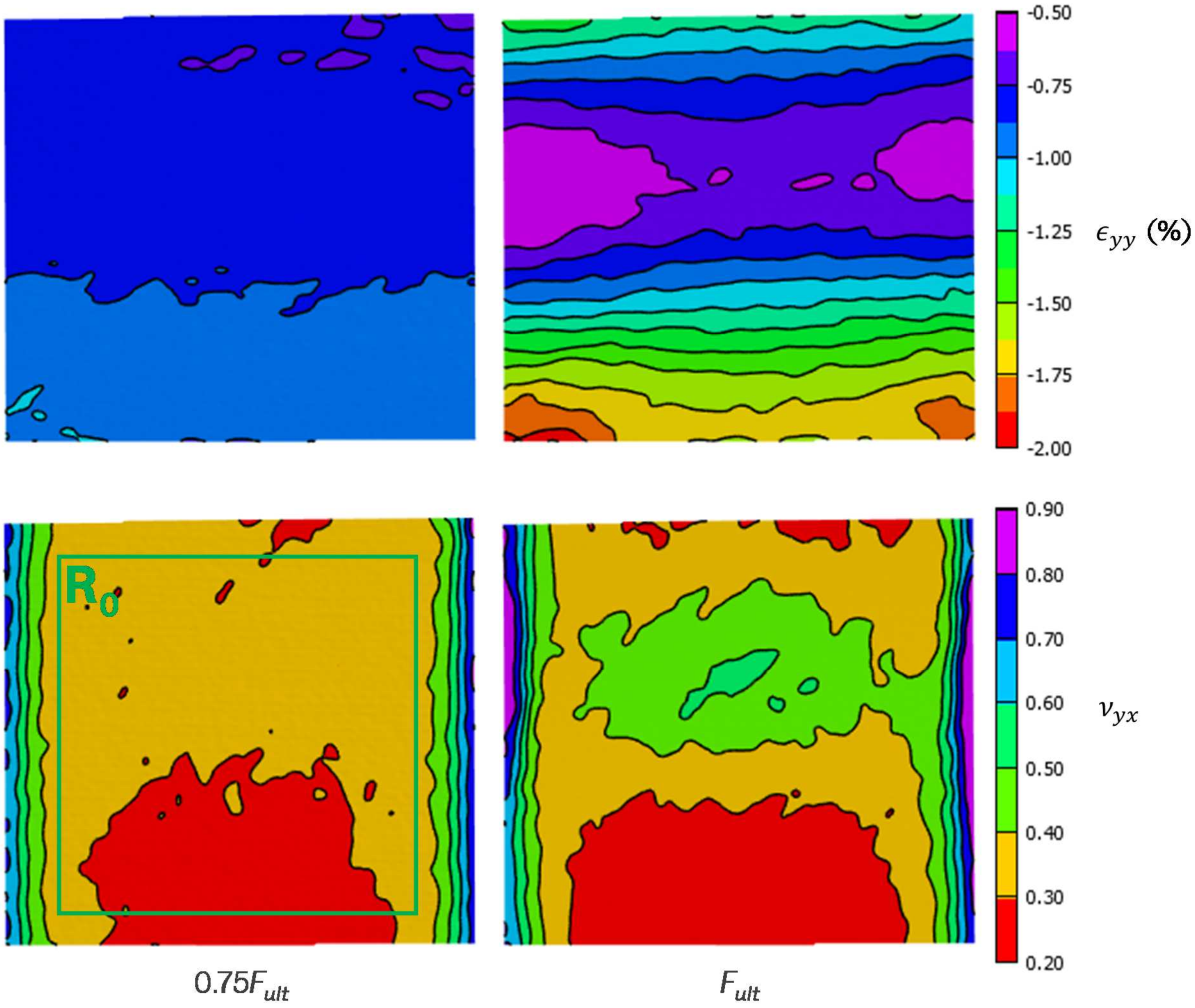

Figure 5-10. Maps of strain and Poisson's ratio in an un-notched specimen at 75% of failure and at imminent failure.

Figure 5-11 shows a comparison of CLT predictions from data in Table against the experimental measurements for modulus and Poisson's ratio. The bars for the experimental measurements indicate the mean of the 6 datasets and the "error" bars are the 95% confidence intervals (CI) assuming a t-distribution of the data, which is more appropriate for this sample size. As expected, the experimental modulus is significantly lower that the CLT estimate, but the narrow CI supports the assumption of the elastic response being independent of the material system. Also as expected, the CLT prediction of ν_{yx} is within the experimental CI, which is also narrow.

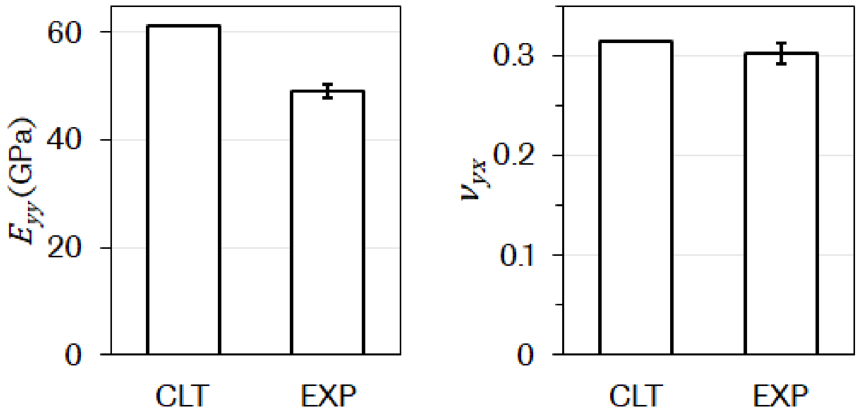

Figure 5-11. Comparison of CLT predictions against experimental measurements.

Measurements of ultimate axial stress σ_{ult} and strainϵ_{ult}, and ultimate load F_{ult} were also made but not compared against a theoretical prediction since the loading conditions deviate from a purely in-plane state and the compressive strengths of the constituents were not known. Nonetheless, these properties serve as a comparison basis for the OHC tests.

Table 5-6. Experimental properties of un-notched specimens.

	E_{yy} (GPa)	ν_{yx}	F_{ult} (kN)	σ_{ult} (MPa)	ϵ_{ult} (%)
$MEAN_{CLT}$	61.04	0.314	-	-	-
$MEAN_{EXP}$	49.13	0.302	49.77	528.77	1.01%
SD_N	1.22	0.010	3.83	34.71	0.05%
CI_t	1.28	0.011	4.03	36.43	0.05%

This data is shown in Table 5-6, where SD_N indicates the standard deviation assuming normally distributed data and CI_t is 95% confidence interval from a t-distributed dataset. It is worth noting that, again, both spread measures are narrow and of the same order of magnitude. This may indicate that pure compressive failure of un-notched laminates is controlled by ply properties rather than interlaminar strength, which would be consistent with observations from previous workers [32], [35], [103].

5.3.2 Compression of notched specimens

The typical stress-strain response from OHC tests is shown in Figure 5-12. Note that σ_{yy} is based on the gross cross-sectional (i.e. disregarding the hole) at the specimen centre length and ϵ_{yy} is again the average of 3 virtual extensometers along the ROI width.

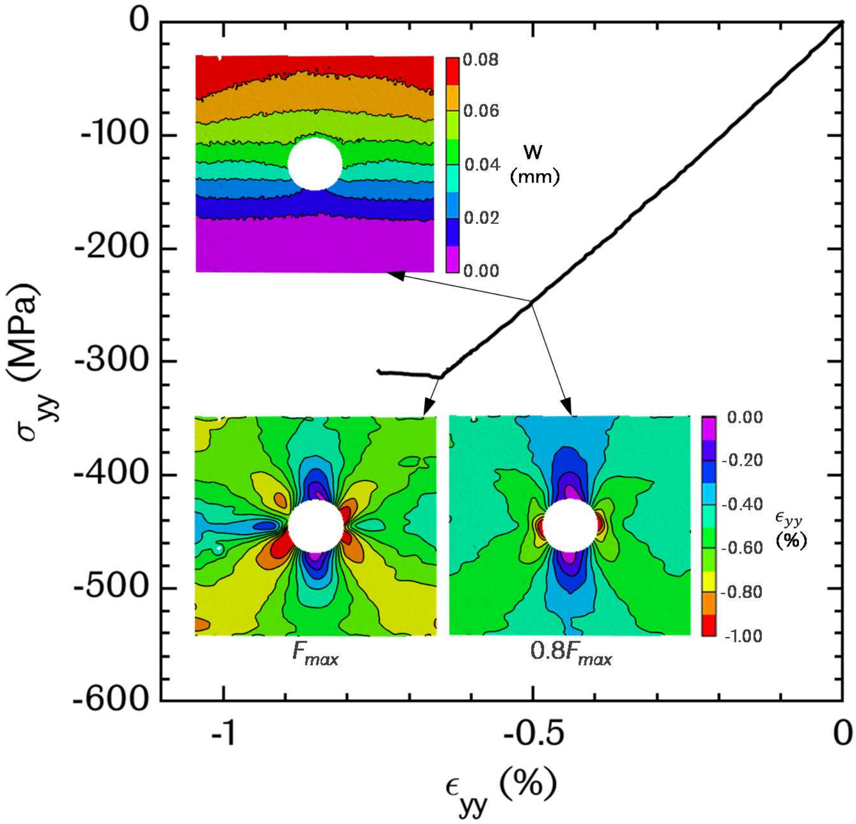

Figure 5-12. Typical compressive response of an OHC specimen. Insets show corresponding of maps of out-of-plane displacement W and ϵ_{yy}.

The compressive response is nearly linear up to the maximum load F_{max} and then load is maintained relatively constant until failure. From the W map at the top inset of Figure 5-12 it can be seen the out of plane displacement at the half-length of the specimen remains relatively small at $0.8F_{max}$. Also, load application across the width of the specimens was observed to be even up to loads of $0.8F_{max}$, as can be reasoned from the symmetry of the inset maps in Figure 5-12. At maximum load at least one of the locations next to the hole (left or right) will display a sudden an very localized softening, suggesting the full development of a crush zone in the 0° plies which, in turn, gives way to delamination. These delamination zones grow towards the edges of the specimen, perpendicular to the load axis before bulk failure by buckling.

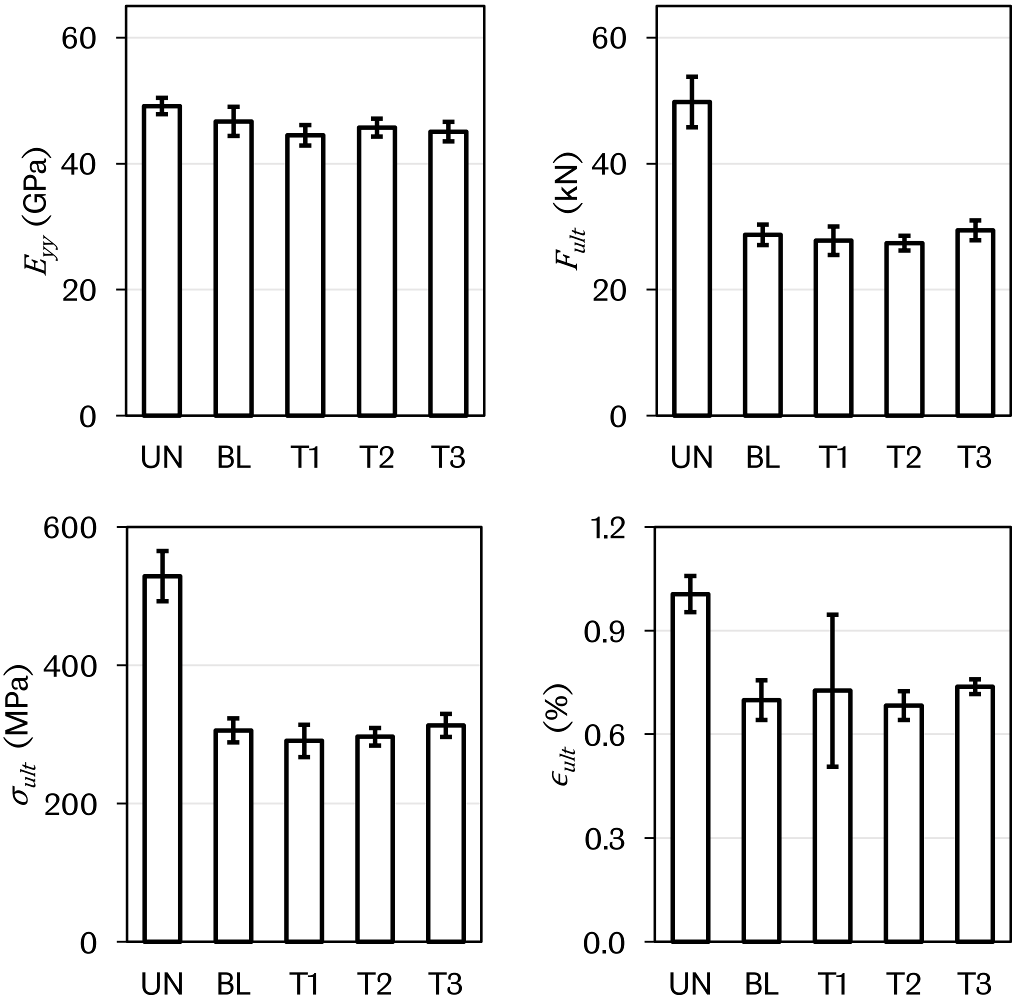

Figure 5-13. Experimental measurements from the OHC tests compared against UN results.

A comparison of the measurements made in the 4 material systems is shown in Figure 5-13 and listed in Table 5-7 with measures of spread. The bars in Figure 5-13 indicate the mean from each specimen set and the error bars are the 95% confidence intervals from assuming a t-distribution of the results. Notable findings on the measured OHC properties tests are as follows:

E_{yy} – for comparison, measurement of the modulus in OHC specimens was obtained using the same method as the UN specimens. Namely, the average strain from 3 virtual extensometers set over the width of the ROI was plotted against σ_{yy}. Then the modulus was obtained from a linear least squares fit of the $0 < F \leq 0.8F_{max}$ interval. It was found that the presence of the notch does not decrease the stiffness of the specimens significantly and does not change as a result of interleaving.

F_{ult} and σ_{ult} – the presence of the hole significantly reduces the compressive strength of the laminate by up to 50%, which is in agreement with previous observations from Soutis et al [43] and Lessard and Chang [41]. Also, the addition of interleaving did not impact the strength significantly. The T1 and T2 systems showed a slightly lower mean strength than the BL laminate with T4 showing a small increase. However, these differences are not conclusive since all means fall within the CI_t band.

ϵ_{ult} – the ultimate strain was also obtained as for the UN specimens. The mean reduction in failure strain due to the hole was ~25% and, again, interleaving did not appear affect this property. The large spread observed in the T1 systems was likely due to the visibly lower quality of the holes in these specimens and could also be the reason of the larger spread in strength of this system.

Table 5-7. Experimental measurements from OHC tests.

		BL	**T1**	**T2**	**T3**
E_{yy} (Gpa)	$MEAN$	46.69	44.52	45.72	45.08
	SD_N	1.46	0.65	0.88	0.98
	CI_t	2.32	1.63	1.41	1.56
F_{ult} (kN)	$MEAN$	28.72	27.78	27.40	29.42
	SD_N	1.03	0.90	0.74	0.99
	CI_t	1.63	2.24	1.18	1.57
σ_{ult} (Mpa)	$MEAN$	305.39	290.32	296.38	312.50
	SD_N	10.91	9.43	7.99	10.47
	CI_t	17.36	23.43	12.72	16.66
ϵ_{ult}	$MEAN$	0.70%	0.73%	0.68%	0.74%
	SD_N	0.04%	0.09%	0.03%	0.01%
	CI_t	0.06%	0.22%	0.04%	0.02%s

5.3.3 Damage morphology under (quasi) static loading

In order to observe and quantify damage development in OHC specimens from the DIC data, interrogation points were set at the locations were damage was more likely to initiate, i.e. left and right of the hole. Plots of the average axial strain against pointwise W displacements were produced for every specimen and distinct stages in the damage development were identified.

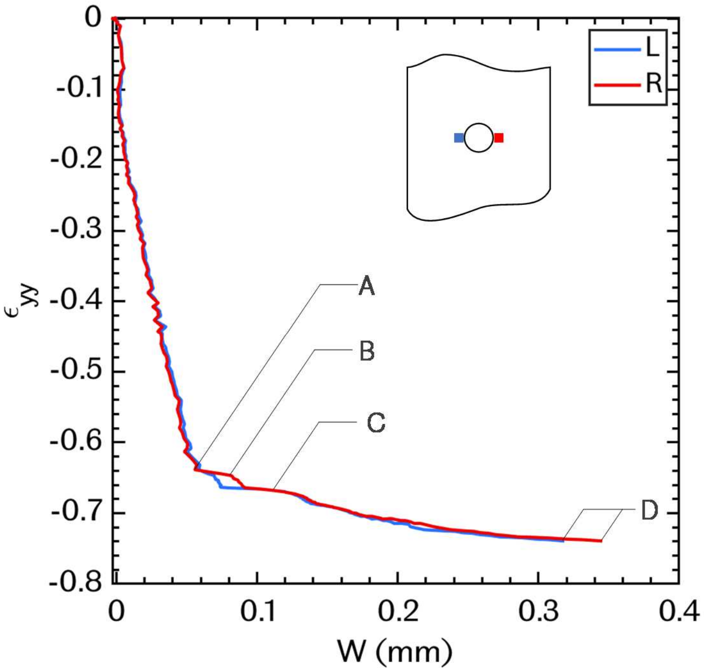

Figure 5-14. Plot of average strain vs. pointwise measurements of W near the left and right edges of the hole.

These stages can be seen in Figure 5-14, where the response of W at the L and R locations is linear below 85% of the failure strain but this deformation is a result of the specimen deviating from perfect in-plane conditions. Point A indicates the maximum strain without observable damage. Corresponding maps of W and ϵ_{yy} are shown in Figure 5-15. Then, point B denotes the axial strain level at which damage can be first observed with DIC next to the notch in the form of a localized gradient of W and strain relaxation, suggesting that the collapse of kink bands in the 0° plies causes localized delamination. Point C is the onset of the second crush zone, which shows the same response of W and ϵ_{yy}. Lastly, point D marks the stage where large scale delamination lead to bulk failure of the specimen.

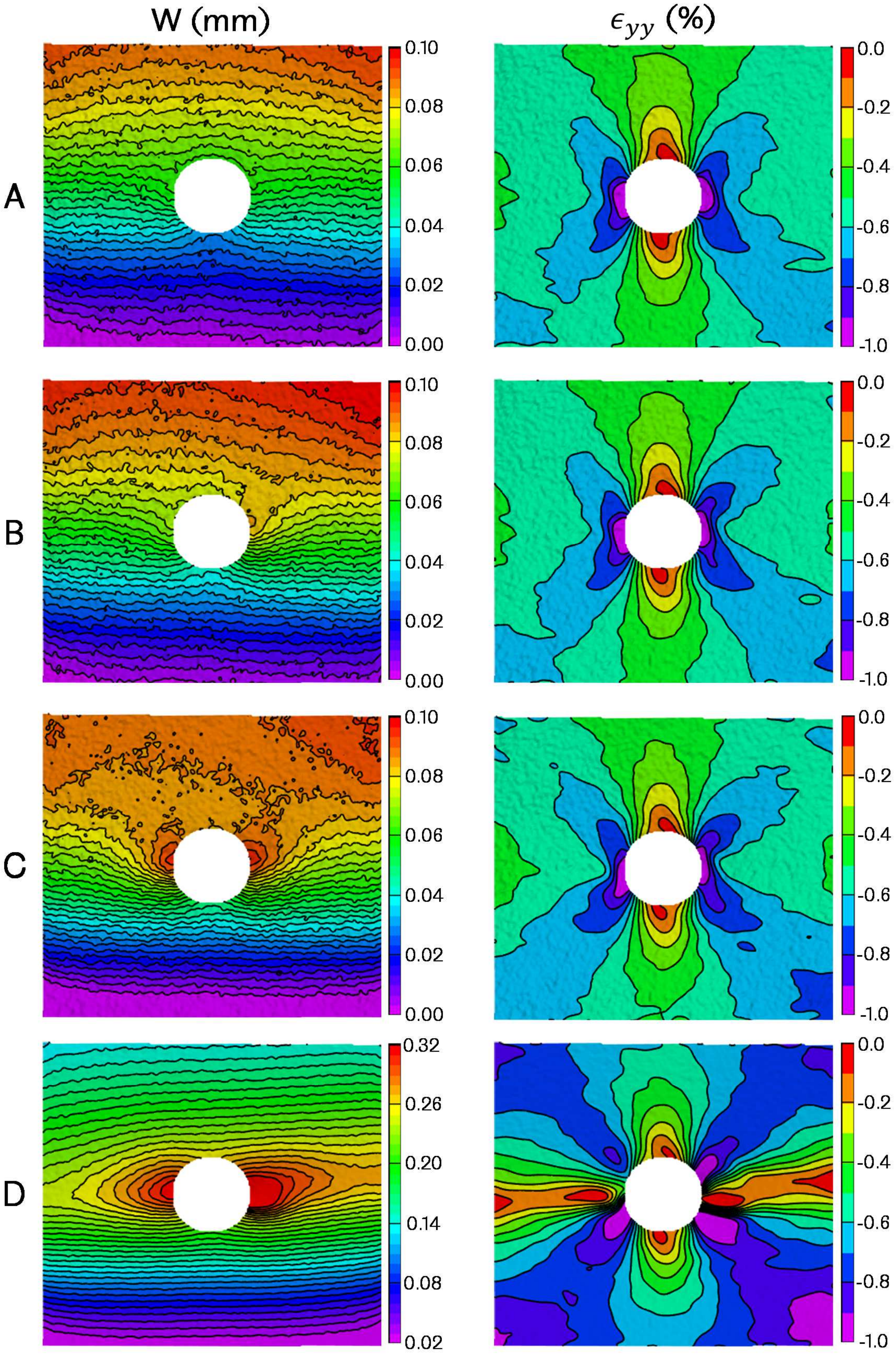

Figure 5-15. Maps of out-of-plane displacement W at (A) load before development of observable damage, (B) onset of delamination, (C) development of 2nd crush zone and (D) imminent failure

It may be reasoned then, that a measure of damage resistance may be obtained from extracting the local strain and corresponding load at which these localized gradients of W first appear, under the assumption that hole quality (i.e. machining damage) is consistent between specimens.

5.3.4 Effect of interleaving on the OHC damage resistance

Comparisons of the local strain at the onset of the first crush zone, denoted ϵ_{CZ}, and the corresponding load are shown in Figure 5-18, where the bars indicate the mean values for each set of specimens and error bars the range of measured values. In contrast with global measurements, a difference between the systems can be observed suggesting that interleaving affects the onset of delamination and may contribute to control damage development around the notch. However, only the T3 interleaved system was seen to improve the resistance to the initiation of delamination of the BL laminate. The load required for the creation of the first crush zone was comparable for the BL and T3 systems, but the interleaved system sustained larger local strains in average. If compared with global measurements in Figure 5-13, the local data appears to have the same hierarchy between the systems but the differences are more marked. More tests would be required to reduce the statistical confidence intervals and make these differences more definite in order to draw statistically sound conclusions on the effect of interleaving.

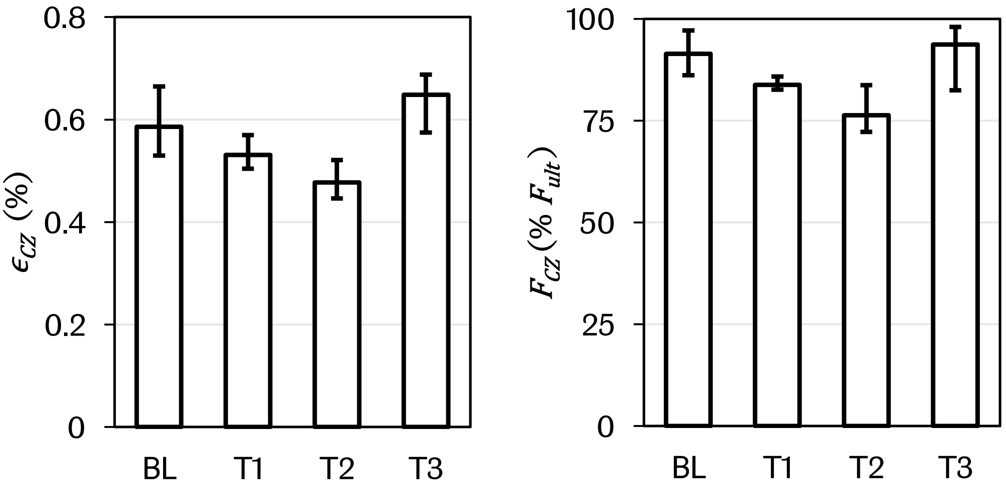

Figure 5-16. Graph of local strain and load at the onset of delamination in the hole vicinity.

5.4 Summary

The experimental findings presented in this chapter showcase the potential of stereoscopic digital image correlation to study the development of damage at the vicinity of stress raisers in composite laminates. As a caveat, great care must be exercised to optimize the rig configuration and settings, as well as the speckle pattern, to reduce the noise floor while maximizing the spatial resolution. The necessity for the latter cannot be overstated as being able to use a smaller subset size, and consequently a smaller VSG, allows to resolve the very acute gradients that reveal the initiation of damage. Nonetheless, a trade-off between noise and the ability to resolve damage will remain and the experimentalist must make a judicious decision to get the best balance.

Concerning the effect of interleaving on the static performance of un-notched CFRP laminates, it was found that the addition of two different particles did not have a significant effect on the elastic properties of the specimens, i.e. modulus and Poisson's ratio. This is relevant to designers as it desirable to toughen the laminate without sacrificing the specific stiffness of the base material. In order to approximate the loading conditions to pure in-plane deformation, either a modification of the specimen geometry (shorter or thicker) or an adjustment of the loading fixture is needed. This would be needed to obtain valid data from failure properties.

Lastly, testing of OHC specimens showed first that the bulk stiffness of the undamaged laminate is not significantly decreased by the presence of the hole. Conversely, there is a marked reduction in the compressive strength of the notched specimens. Again, the interleaved systems did not show any clear differences against the baseline laminate, within the results spread. The significantly larger variation in the T1 system data is believed to be a consequence of visibly lower hole quality, thus highlighting the need for a metric to assess initial damage. In contrast to global measurements, pointwise data extracted from the highest strained region showed a marked difference between the materials, with T3 being the only interleaved system to sustain larger ϵ_{yy} before the onset of delamination at the hole edge.

CHAPTER 6 OHC FATIGUE TESTING

This chapter describes the application of TSA and DIC to the study of OHC fatigue. Details of the history and development of infrared thermography and thermoelastic stress analysis are given at the outset in Sections 6.1 and 6-2. Then the particular application of TSA to study composite laminates and the considerations necessary for a correct interpretation of the results is detailed in Sections 6.3 and 6.4. The experimental arrangements and validation studies for TSA are described in Section 6.5; details of the 2D-DIC setup are also provided. Lastly, the results section (6.6) comprises a description and comparison of findings made from the experimental measurements (analogue, TSA and DIC) and statistical analyses of the fatigue tests.

6.1 History and overview of TSA

Analogous to the advent of DIC as an established technique for experimental mechanics, the last 3 decades have seen an increase in the use of TSA, albeit to a lesser extent than DIC. The slower growth can be explained by the significantly higher cost of thermal cameras (particularly photon detectors) in comparison with visible light cameras. However, the ability of TSA to obtain maps of stress or strain in real time make it a superior technique for damage monitoring and, due to the requirement for varying load (typically cyclic), also for fatigue testing. The full-field nature of TSA compounded with noise rejection from *locking-in* the thermal signal with the loading signal of the structure, enable the technique to resolve surface gradients at the pixel level. Further, capturing the temperature distribution and its evolution facilitate the observation of damage process zones. Thus, concerning this thesis, it was recognized that TSA could help to shed light on the damage mechanisms of OHC fatigue and the impact of interleaving on the fatigue performance of the specimens.

TSA works by measuring the small temperature variations in a structure when it is subjected to load, which needs to be applied such that adiabatic and reversible conditions hold; this is typically achieved by applying a cyclic load at a sufficiently high frequency to minimize heat conduction in the specimen. When these conditions hold, the cyclically loaded structure will undergo in-phase temperature variations that, for an isotropic elastic solid, are proportional to the change in the first stress invariant on the surface of the solid, i.e. the sum of the orthogonal direct stresses.

The thermomechanical coupling in elastic media is known as the *thermoelastic effect*. The phenomenon was first recognized by Weber in 1830 [104] and given a theoretical foundation by Thomson [105] in 1853, whose treatment was confirmed experimentally by Compton and Webster [106] in 1915. The next major development was made by Biot during the 1950s who extended the theory to account for anisotropic, viscoelastic and plastic material response [107]–[110] based on irreversible thermodynamics.

A general expression derived by Potter and Graves [111] that accounts for anisotropy and, mean stress and temperature dependent material properties under adiabatic and reversible conditions can be expressed as

$$\dot{T} = \frac{1}{\rho C_\epsilon}\left[\frac{\partial C_{ijkl}}{\partial T}(\epsilon_{kl} - \alpha_{kl}\Delta T) - C_{ijkl}\left(\alpha_{kl} + \Delta T\frac{\partial \alpha_{kl}}{\partial T}\right)\right]\dot{\epsilon}_{kl} \tag{6}$$

where ρ is the material density, C_ϵ is the specific heat under constant strain, T is the temperature, C_{ijkl} is the fourth-order stiffness tensor, α_{kl} is the thermal expansion coefficient tensor and ϵ_{kl} is the strain tensor. Note that the dot accent indicates a direct differential and hence the rate of change. Special forms of Eq. (6) have been derived to account for non-zero mean stresses [112], cyclic plasticity [113], residual stresses [114] and temperature dependent properties [115]. Most practical measurements with TSA seldom require the use of the full form of Eq. (6). Often many of the terms aforementioned are small quantities or within the noise, and can be neglected. The particular expressions used for TSA of composite materials will be described later, but it is first needed to detail the equipment used for IR thermography.

6.2 Infrared thermography

All physical bodies at a temperature above absolute zero will emit electromagnetic radiant energy across a wide spectral range. The nature of this radiation depends mainly on the body's temperature, but is a function of both temperature and wavelength. This relationship was first expressed analytically for a *blackbody* by Max Planck [116] in 1900 as

$$\Phi_{\lambda,b} = \frac{2\pi c^2 h}{\lambda^5 \left(e^{\frac{ch}{k\lambda T}} - 1\right)} \tag{7}$$

where $\Phi_{\lambda,b}$ is the spectral radiant emittance of a blackbody, c is the speed of light, h is Planck's constant, λ is the wavelength, k is the Boltzmann constant and T is the absolute temperature of the blackbody. A blackbody is an idealised object that can absorb all incident radiation, regardless of frequency, polarisation or angle of incidence [116]. When a blackbody is in thermal equilibrium, i.e. at a constant temperature it emits back all the radiation absorbed. Thus, by setting T constant in Eq. 7 a series of isothermal curves can be constructed as shown in Figure 6-1. The infrared spectrum can be divided into three wavelength bands, namely: near infrared from 0.75 to 2.5 μm, mid infrared from 2.5 to 25 μm and far infrared from 25 to 1000 μm [116]. The amount of thermal energy (heat) transferred as radiation increases with temperature and for the order of magnitude around ambient temperature this peaks in the wavelength range of 2 to 15 μm. For this reason, most thermal detectors are designed to operate within this range [117] at the wavelengths of two atmospheric windows: $3 - 5\ \mu$m or $8 - 14\ \mu$m. The lower wavelength window is more adept for high temperature measurements, but is suboptimal for room temperature.

Practical application of thermography requires knowledge, primarily, of the subject matter's emissivity in order to relate the detector signal to the objects temperature. The perfect radiation absorption of blackbodies are unattainable by real materials and can only be a fraction. Hence, the ratio between the emitted radiation of a real object and blackbody radiation at a particular temperature is known as the *emissivity* and is defined as

$$\varepsilon(\lambda, T) = \frac{\Phi_\lambda}{\Phi_{\lambda,b}} \tag{8}$$

where Φ_λ is the object's emittance. As Kirchoff's Law states that the absorbed energy by a surface is equal to its emittance, surface preparation is important for thermographic measurements [118]. Thus, based on its spectral emissivity, a real source can be defined as a *graybody* when its emissivity is constant, independent of wavelength and has the same spectral shape as a black body. The alternative kind of real source are selective radiators for which ε is an explicit function of λ [118].

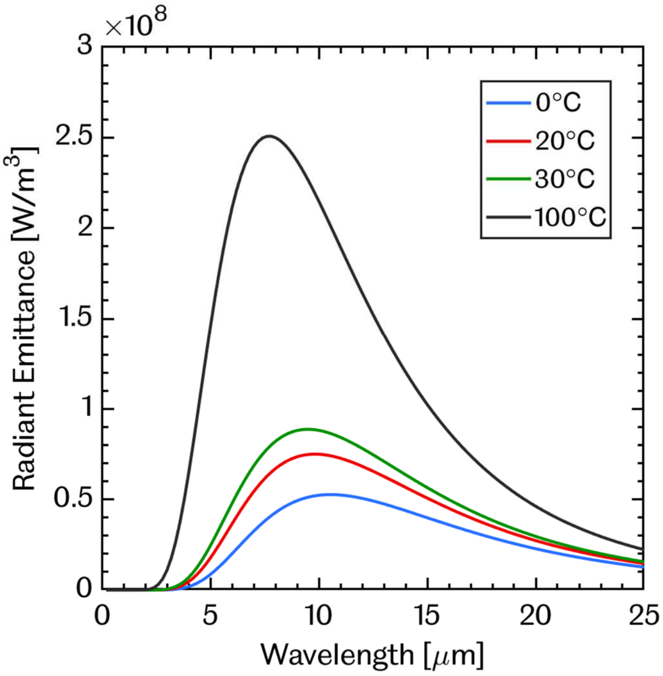

Figure 6-1. Isothermal curves of blackbody radiation.

The main component in a TSA system is an infrared detector used to measure the small temperature changes that result from the thermoelastic effect. An infrared sensor is therefore a transducer as it converts radiant energy into an electrical signal. Based on the physical mechanism of this conversion, infrared detectors can be classified into either thermal or photon detectors.

Thermal detectors respond to incident radiation by changing the electrical or mechanical properties of the sensor materials as a result of the input heat flux and these changes are then measured by an external electrical circuit. The thermal effects on the sensor are independent of the spectral properties of the incident radiation and, thus, their sensitivity is only limited by the heat capacity of the sensor elements or the spectral properties of a protective filter in front of the sensor. The most common kind of thermal detector used for TSA are bolometers. However, their application is limited by the slower capture rates possible due to the sensors time constant, i.e. the time needed for the absorptive element in the sensor to heat up.

Photon detectors use a semiconductor sensor that works by converting incident photons into conducting electrons. That is, when incident photons have an energy larger than the bandgap energy of the semiconductor element, the electrons in the sensor with be raised from their valence bands to the mobile conduction band. Therefore, the sensor will only respond to photons of a maximum wavelength and less, in order to output a voltage that is proportional to the radiant emittance of the source. In contrast with thermal detectors, photon detectors offer higher sensitivity and are capable of much higher sampling rates. For this reason, they are more widely used for TSA measurement.

Although the first practical use of an infrared radiometer to perform TSA measurement was made by Belgen in 1967 [119], it was not until the late 1970s that the use of the technique became more widespread due to the development of the first commercial system dedicated to TSA by Mountain and Weber [120]: SPATE (Stress Pattern Analysis by Thermal Emission). The SPATE system featured a single-detector sensor that produced rasterized images by use of two independently positionable mirrors. The detector was designed to respond to a peak photon wavelength of 12.4 μm and over a range of 8 – 13 μm, making its application optimal for room temperature.

Modern photon detectors use 2-dimensional focal plane arrays (FPAs) that, in contrast to single-detector sensors, are comprised of multiple detector elements that cover the image field of view and determine the resolution of the image [121]. They are commonly known staring arrays because they capture an image by sampling all detectors at once instead of doing line-scanning. Due to the greatly improved signal-to-noise ratio and higher attainable frame rates, staring arrays are extensively used in TSA. The system used for this thesis features a 256 × 256 pixel^2 DeltaTherm camera developed by Stress Photonics [122], which will be described in detail in Section 6.2.2. Another characteristic of photon detectors is that they need to be cryogenically cooled to minimize noise resulting from background radiation and thus improve the signal-to-noise ratio of the sensor's output.

The primary goal of TSA is to obtain a measure of stress (or strain) from the change in the thermoelastic signal. To achieve this, the detector's output (temperature) needs to be calibrated by one of the following standard methods [123]:

A. Direct calibration using the detector properties, TSA system variables and, specimen surface emissivity and material properties

B. Calibration against measured stress or strain

C. Calibration against calculated stress or strain

Method A requires that the detector is radiometrically calibrated against a measured temperature, i.e. the output voltage as a function of temperature. However, this method is seldom used as it requires accurate knowledge of many individual factors, such as the detector and signal conditioning circuitry sensitivities, and the thermal and mechanical properties of the subject material. Uncertainty in these quantities will compound and yield measurements with greater degree of error.

Methods B and C are more commonly used, whereby using a calibration specimen of the same material and the same surface preparation, loaded at the same frequency and ambient conditions as the test specimen. The geometry and loading of calibration specimens is prescribed so that their stress (or strain) state can be calculated from theory or determined by experiment. Common examples of calibration specimens include uniaxial tensile coupons, a diametrically compressed disc or a beam under four-point bending [123].

6.3 Application of TSA to composite laminates

The anisotropic behaviour of UD composite laminates requires the explicit description of directional material properties in the derivation of TSA expressions. Recalling the convention given in Section 2.2 and shown in the context of a laminate coupon under compression in Figure 6-2, three frames of reference are used to define the mechanical response of a composite specimen. The (1, 2) set defines the principal material axes, the (x, y) set are the principal stress directions and the (*L*, *T*) is an arbitrary frame of reference for which the angle θ relative to the principal material directions is typically of interest in TSA.

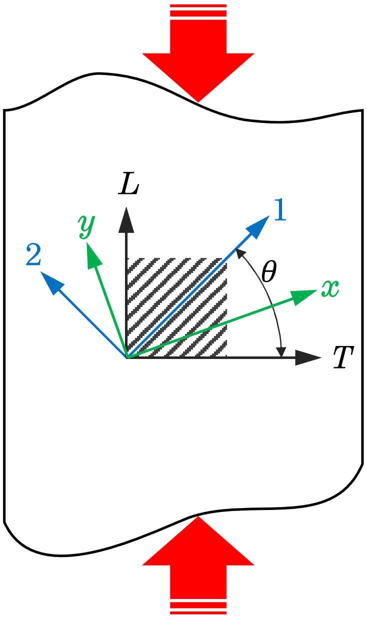

Figure 6-2. Coordinate frames of reference in a composite laminate defining the principal material axes (1, 2), principal stress directions (x, y) and an arbitrary coordinate system (*L*, *T*).

One of the early applications of TSA to the study of composite materials was by Stanley and Chan [124] who derived an expression for the temperature change in terms of stress for a homogeneous orthotropic material as

$$\Delta T = \frac{T_0}{\rho C_p}(\alpha_1 \Delta\sigma_1 + \alpha_2 \Delta\sigma_2 + \alpha_6 \Delta\sigma_6) \tag{9}$$

where ΔT is the change in temperature, T is the reference absolute temperature, C_p is the specific heat at constant pressure, α indicates coefficients of thermal expansion (CTE), $\Delta\sigma$ is the change in stress and, subscripts 1 and 2 refer to the principal material directions and 6 to in-plane shear. It can be seen from Eq. 9 that the change in stress is scaled by the respective directional CTE and, therefore, the thermoelastic response depends on the relative magnitudes of the orthogonal stresses. As for the shear term, Potter [125] noted that α_6 is not a material property and, hence, the thermoelastic response from shear deformation is zero. A reformulation of Eq. 9 in terms of the laminate strains can also be obtained from [125] and more recently from Emery et al. in [126], given as

$$\begin{aligned}\Delta T = \frac{T_0}{\rho C_\epsilon}\{&[(\alpha_1 Q_{11} + \alpha_2 Q_{12})m^2 + (\alpha_1 Q_{12} + \alpha_2 Q_{22})n^2]\Delta\epsilon_L \\ &+ [(\alpha_1 Q_{11} + \alpha_2 Q_{12})n^2 + (\alpha_1 Q_{12} + \alpha_2 Q_{22})m^2]\Delta\epsilon_T \\ &+ [(\alpha_1 Q_{11} + \alpha_2 Q_{12})mn + (\alpha_1 Q_{12} + \alpha_2 Q_{22})mn]\Delta\gamma_{LT}\}\end{aligned} \tag{10}$$

with respect to the coordinate system of interest (L, T), where $m = \cos\theta$, $n = \sin\theta$, $\Delta\epsilon$ and $\Delta\gamma$ are the change in direct strains and shear strain respectively, with the subscripts L and T denoting the arbitrarily defined longitudinal and transverse directions, and Q_{11}, Q_{22} and Q_{12} are the reduced stiffnesses defined as

$$\begin{aligned}Q_{11} &= \frac{E_1}{(1 - \nu_{12}\nu_{21})} \\ Q_{22} &= \frac{E_2}{(1 - \nu_{12}\nu_{21})} \\ Q_{12} &= \frac{\nu_{21}E_1}{(1 - \nu_{12}\nu_{21})}\end{aligned} \tag{11}$$

with E is the elastic modulus, ν is the Poisson's ratio and the subscripts 1 and 2 denote the principal material axes.

This treatment in terms of strain is more adept to study composite laminates since at the mesoscopic scale strain can be considered to be constant through the laminate thickness whereas stress changes acutely at the interface of plies with different orientation. However, a more practical form of Eq. 10 uses a calibration constant A^* such that

$$A^* S \equiv \Delta T \frac{\rho C_\epsilon}{T_0} \tag{12}$$

where S is the detector output signal. Assuming a homogeneous thermoelastic response from the subject material, the calibration constant, also known as the thermoelastic coefficient, can be easily obtained by measuring L and T surface strains in a coupon under uniaxial loading, if the elastic properties are known. The assumption of a homogeneous thermoelastic coefficient is highly dependent on the length scale, i.e. at small scales the heterogeneity of the composite becomes significant in the thermoelastic response, manifested as temperature gradients, and causes the assumption to breakdown.

Temperature gradients result in heat conduction which, in turn, attenuate the thermoelastic signal. This attenuation effect can be seen in an expression derived from first principles by Biot [110] that describes the thermoelastic response of an isotropic body allowing non-uniform temperature distributions, as

$$\frac{\partial T}{\partial t} = \frac{1}{\rho C_p}\left[k\nabla^2 T - T_0 \alpha \frac{\partial \sigma_{I1}}{\partial t}\right] \tag{13}$$

where the instantaneous change in temperature $\partial T/\partial t$ depends on the proportion of the two quantities inside the brackets. The first is the spatial heat transfer resulting from finite temperature gradients as described by $k\nabla^2 T$, where k is the material conductivity and $\nabla^2 T$ is the Laplacian of the temperature field. Then, the second is the adiabatic change in temperature due to the change in stress as described by $T_0 \alpha(\partial\sigma_{I1}/\partial t)$ where σ_{I1} is the 1st invariant of the stress tensor.

It can be seen from Eq. 13 that, at best, quasi-adiabatic conditions are attainable since k is never zero, albeit small for some materials. For the particular case of an undamaged composite laminate, the main sources of non-adiabatic temperature change are the stress gradients at (i) the interlaminar region, (ii) the micro-constituents interface and (iii) any stress raisers, e.g.

notches. Non-adiabatic heat transfer is seen in the TSA capture as a shift in the phase angle between the detector's output signal and the reference loading signal, whereas for perfectly adiabatic conditions the phase angle is uniform over the whole specimen and shifted by 180° for regions where the stress is reversed. Namely, for a fully thermalized specimen under fully reversed cyclic loading the TSA signal would be in-phase with the load signal during the compression excursions and shifted by 180° during the tension half-cycle. It follows then, that the phase angle is useful to validate loading conditions and identify sources of non-adiabatic behaviour. To best approximate adiabatic and reversible conditions, a sufficiently small time scale ∂t is prescribed by the user, the most practical way of doing so is to increase the loading frequency of the test. The adequate time-scale is particular to material properties and architecture, and the length-scale at which the TSA measurements are made.

6.4 Causes of signal attenuation in TSA of composites

6.4.1 Heterogeneity of composite laminates

Bakis and Reifsnider [127] showed that the local thermoelastic response in nominally equal global strain fields is highly dependent on the orientation of the surface lamina and that accurate prediction of the thermoelastic emission requires consideration of the material parameters, namely, fibre volume fraction, layup and thermoelastic properties of the micro-constituents. With respect to heat transfer at the micro-constituents interface, Wong [128] showed that for the typical fibre and matrix used in CFRPs thermal equilibrium is attained in a time interval two orders of magnitude smaller than that of a quarter-cycle at 30 Hz. Consequently, a UD lamina can be treated as homogeneous for the purposes of TSA.

However, Wong [128] also showed that at the typical loading frequencies used for TSA (5 – 30 Hz) the thermoelastic process in multidirectional laminates cannot be treated, in general, as homogeneous nor adiabatic due to the effects of stress gradients at the interlaminar regions of plies with different orientations. Heat diffusion between plies occurs at a time scale comparable to the loading frequency and this prevents the laminate from fully thermalizing through its thickness. In Ref. [128] Wong shows that for frequencies up to 30 Hz, the temperature response at the surface of a multidirectional carbon-epoxy laminate is the combination of at least the two outermost plies. The ply-depth until which the contribution to the surface thermal distribution is significant depends on mainly on frequency, but is also affected by stacking sequence. It follows then, that the train of subsurface materials must be accounted for in the interpretation of TSA data for composite laminates. This is inclusive of any coating on top of the outermost ply, which is typically in the form of a paint coat or resin layer. A paint coat can be applied to increase and homogenize the surface emissivity, whereas the surface resin layer is a natural consequence of the manufacturing process.

6.4.2 Paint coating

It is widely acknowledged that depending on its characteristics, coatings applied to the test surface, can significantly modify the thermoelastic response [129]–[131]; a coat of matt black paint is typically applied to specimens in preparation for TSA. Although polymers used as composite matrix have a naturally high emissivity, the surface finish from manufacturing can be uneven or reflective. For laminates consolidated using an autoclave, it is common for the surface at the tool side to be highly specular which causes artifacts in the TSA capture. To minimize the specularity, a coat of high emissivity paint is applied to the test surface but since the influence of the paint coat on the surface emittance is non-trivial, care must be taken to characterise it.

A study by Robinson et al. [131] details the attenuation of the thermoelastic emission by the paint coat as a function of thickness and loading frequency. Namely, that the thermoelastic response of a painted surface can be divided in four regions based on frequency vs. thickness, termed as follows:

A. High emissivity region, where the temperature distribution of the painted surface matches that of the substrate.

B. Opacity limited region, where the paint thickness is not sufficient to cover the test surface entirely and thus the emissivity is not homogeneous.

C. Coating diagnostic region, where the loading frequency is too high for the respective coat thickness so that the heat cannot be transferred quickly enough through the paint layer and reproduce the temperature change of the substrate.

D. Strain witness region, where the thermal emission at the surface is entirely from the paint coat alone due to the coat being too thick or the loading frequency too high.

To obtain a paint coat that falls in the high emissivity region, the authors in [131] suggest the use of RS matt black spray paint as the best commercially available option, with an estimated emissivity of 0.92. The recommendation for specimen preparation is to apply 2 to 3 'passes' of paint for loading frequencies between 5 and 15 Hz. This recommended paint coat should be equivalent to a thickness of 15 to 25 μm. However, through the development the work in this thesis, it was found that in practice the application of the paint coat by spraying is highly subjective and dependent on environmental factors that are hard to control. That is, the particular amount of paint that is deposited on any one specimen depends, among other things, on the operator skill, distance to target surface, ambient conditions (temperature and humidity), remaining volume of paint in the can and the level of atomization of the paint by the spray cap.

These conditions combined cause, to a varying extent, a suboptimal paint coat in thickness, homogeneity and coverage. Arguably, the paint coat could be characterized by measuring it, but the precision and resolution needed for such measurements render the effort impractical because the factors affecting the paint coat cannot be controlled. It rests then with the researcher to acquire sufficient skill in order to apply the paint and gauge the coat quality of the specimens consistently, following the guidelines found in literature. Details of a parametric study done to optimize the paint application for the work in this thesis are given in Section 6.6.

6.4.3 Surface resin layer

The influence of the surface resin layer has also been object of substantive investigation in TSA of composites. Above a certain thickness the resin layer can act as a strain witness, masking the orthotropic thermoelastic response and instead displaying isotropic behaviour. This effect was explicitly studied in [130] for polycarbonate coated metallic specimens, where the authors found that at thicknesses > 0.5 mm loaded at frequencies of minimum 5 Hz the coating acts as a strain witness. However, typical thicknesses in composite laminates are of the order of $< 50\ \mu$m and depending on the fibre and matrix material properties the surface resin layer can produce an isotropic thermoelastic response.

For glass – epoxy laminates with a surface resin layer thickness of $25\ \mu$m, Emery et al. [126] found that the surface emission was isotropic at frequencies around 10 Hz. However, more recent work by Sambasivam et al. [132] suggests that the treatment of the resin layer as a strain witness is not always reliable since the isotropy assumption fails to agree with experimental measurements of E-glass and epoxy prepreg laminates with resin layer thickness of $30\ \mu$m loaded at 10 Hz. The findings in [132] suggest instead that treating the surface response as orthotropic yields better results.

6.4.4 Damage

TSA is a technique adept to the study of damage in composite materials because the detector typical sampling rates are high enough to allow for observations of damage in near real-time. Also, since the spatial resolution is equal to the pixel size at the selected magnification, acute strain gradients in damaged laminates can be observed with good detail provided that motion of each material point is negligible or compensated for.

For these reasons the technique has been used to study damage development by several authors. Cunningham et al. [133] found that the presence of damage in a notched glass – epoxy specimen modified the thermoelastic signal as a combined effect of stress redistribution and localized heating resulting from the damage processes. Horn et al. [134] used TSA to calculate a modified stress concentration factor (mSCF) in dogbone specimens of an injection moulded glass – polyurethane with impact damage. The mSCF was then used to estimate the residual fatigue life by scaling the nominal stress amplitude and locating the modified value in the baseline stress-life cycles (S-N) curve for the material. Also in [134], the temperature maps were shown to have sufficient detail to resolve and track crack growth in the specimens. The same authors [135] also used TSA and the mSCF method to study machining damage in glass – polyurethane specimens with an open hole subjected to tensile fatigue.

Although TSA readily allows for the observation of damage in composite laminates, even subsurface damage [136], the relationship between the surface thermal emission and the structural response is much more complex than for an undamaged laminate. From Eq. 9 it can be seen that since ΔT depends on the reference temperature, local increases in temperature due to damage processes will offset the thermoelastic signal as a natural consequence of the increased surface emittance as per Eq. 7. Dulieu-Barton et al. [137] developed a calibration methodology that can correct the offset in the TSA signal caused by local heating. The methodology was then successfully used by Emery and Dulieu-Barton [138] to monitor damage in a glass – epoxy prepreg laminate with an open hole subjected to tensile fatigue.

In the current work, the ΔT maps are normalized by the direct temperature maps obtained from the TSA software. Since specimen motion is not compensated in the TSA data due to reasons given in Section 6.6, the normalization by the reference temperature can only partially correct for offsets in the thermoelastic signal. However, the corrected ΔT and direct temperature maps can provide a quantitative measure of damage and allow to observe the different damage processes under compressive fatigue. Although localized heating due to damage processes is unavoidable, the resulting thermal gradients can be used to identify initiation and causality in these processes.

6.4.5 Motion

Significant attenuation in the TSA signal can result from motion of material points that is greater than the detector pitch at the selected magnification [139]. When motion is not compensated for, the temperature difference mapped to a pixel position is the result of subtracting two different material points at a distance equal to the total displacement vector between the load extremes (peak and trough), thus introducing error in the ΔT maps. As a consequence, the amount of signal attenuation is proportional to the thermoelastic gradient, i.e. zones with the largest deformation levels (acute gradients) will increase motion blur.

There is several ways to minimize error due to motion of the test surface, namely:

i. Subtract a constant displacement vector taken from prescribed features in the test surface. The features are selected so that motion is apparent between load peaks and troughs, e.g. an edge or a mark with thermal contrast. The vector is then calculated between each pair of peak and trough frames and subtracted from the pixel positions. However, the motion compensation algorithm is typically embedded in the TSA software and therefore varies in complexity depending on the company that developed it.

ii. Acquire the deformation map via an additional technique, like DIC, and use the deformation maps to compensate for specimen motion. This method is an extension of the first (i) and has been shown by several authors to minimize the error due to motion in complex deformation fields [140]–[142].

iii. Select a magnification level whereby the pixel size is larger than the deformation level. This is the simplest way to circumvent motion blur in TSA, but with the caveat that the reduction in spatial resolution will result in lesser capacity to resolve gradients.

In the current work the DeltaTherm TSA system used lacks a robust motion compensation method for continuous monitoring, as the only option available is to manually compensate for simple edge motions by subtracting user selected points at each capture. Due to the TSA software not allowing for continuous capture of ΔT and temperature maps whilst having the motion compensation option on, the magnification was selected so that motion levels were comparable to the pixel size to minimize motion blur. The ability to automate data capture at set intervals was a priority for the fatigue tests—given that a single test could last more than a full working day, thus rendering manual captures impractical.

6.5 Experimental setup

6.5.1 TSA rig and setup for fatigue testing

The TSA setup used in the current work was comprised of a DeltaTherm 1410 camera head controlled by a PC and connected to a signal processing unit, which is in turn connected to the servo-controller, as shown schematically in Figure 6-3; the system is manufactured by Stress Photonics[5] . The camera head features a 256 × 256 pixel^2 Indium-Antimonide (InSb) staring array, also known as a focal plane array (FPA). The sensor is cryogenically cooled to 73K using a liquid nitrogen deposit to achieve its nominal temperature resolution of 10 to 18 mK for wavelengths 3 to 5 μm. The detector can acquire 14 bit digital images via an IEEE 1394 interface at a maximum frame rate of 140 frames per second with a minimum exposure time of 200 ns. The saturation exposure time at room temperature is ~2ms. The software used for data capture and TSA processing is DeltaVision version 19 and system specifications are listed in Table 6-1.

---

[5] Stress Photonics, 3002 Progress Rd. Madison, Wisconsin 53716, USA. url: http://www.stressphotonics.com/

Table 6-1. TSA system specifications

Camera	DeltaTherm 1410
Detector	256 × 256 pixel InSb cooled FPA
Sensitivity wavelength	3 – 5 μm
Detector pitch	30 μm
Max frame rate	140 fps
Minimum integration time	200 ns
Saturation integration time at RT	~2 ms
Sensor operating temperature	73 K
Nominal temperature resolution	10 – 18 mK
Digitization and interface	14 bit, IEEE 1394

In the current work only 2 lenses were adequate to the FOV and thus were evaluated to optimize the magnification; details of this are shown in Section 6.5.2. The selected lenses were a 25mm focal length with f/2.3 fixed aperture and a two position zoom lens. However, the camera head can be paired to a variety of lenses with bayonet mount. To perform measurements the camera is positioned perpendicular to the test surface at the standoff distance needed to focus the desired FOV. An estimate of the magnification can be calculated by counting the pixels needed to resolve a physical feature of known dimensions.

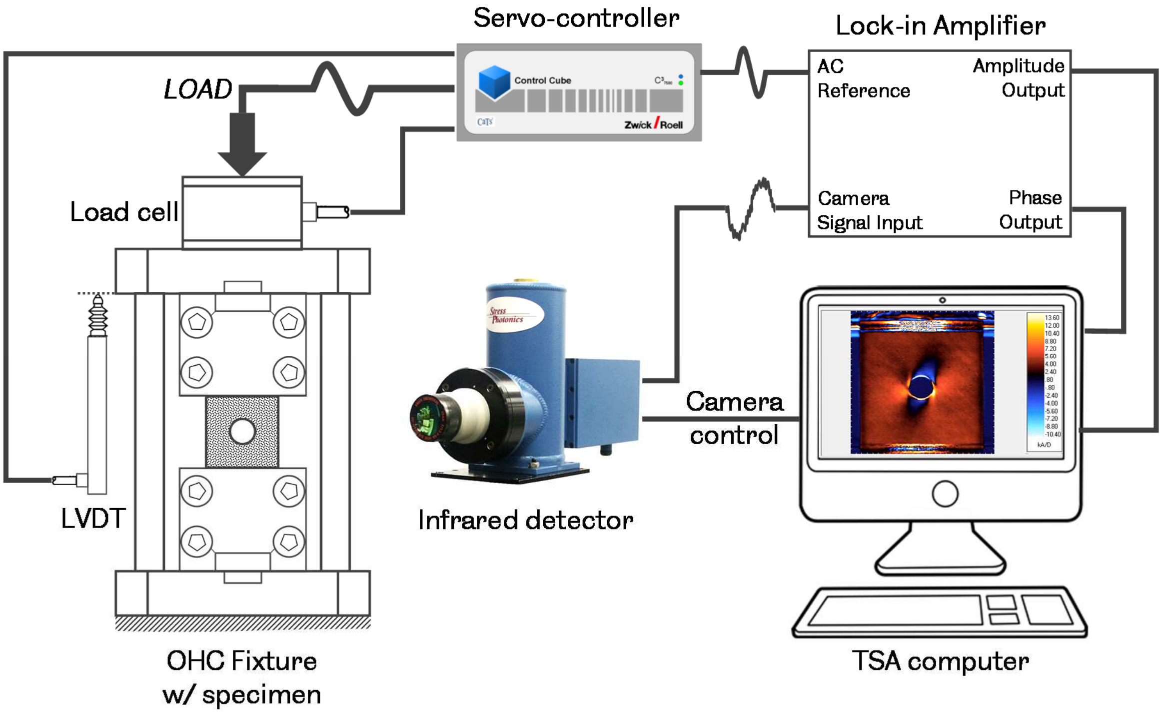

Figure 6-3. Schematic of TSA experimental setup

Once the magnification is set, the detector shutter settings can be adjusted to maximize the TSA signal-to-noise ratio, namely exposure (or shutter speed) and capture rate or frames per second. The exposure is typically set so that enough dynamic range is available to capture the thermoelastic temperature change (ΔT) and avoid saturation of the detector pixels. Conversely, the capture rate is typically set to maximum to fully capitalize on the noise rejection algorithm of DeltaVision.

The detector signal outputs to the signal processing unit which consists, mainly, of a lock-in amplifier [16], [143] that extracts the thermoelastic signal from the inherently noisy detector output. Signal changes associated with thermoelastic response of composite materials are typically embedded in large-bandwidth noise with amplitude up to 40 times larger [16]. To extract the ΔT signal, the lock-in amplifier multiplies a reference signal, with the same frequency and high signal-to-noise ratio, by the detector output signal and integrates the product over a number of periods to obtain a DC voltage level that is proportional to the amplitude of ΔT component [16]. The lock-in amplifier can be described, in a simple manner, as a signal mixer and a low-pass filter connected in series. To further reject noise the detector can be set to record longer durations, proportional to the time-constant of the low pass filter, which narrows the frequency band pass. The selection of the capture duration or integration time is arbitrary and depends on the application. A longer capture integration produces a “cleaner” image but smooths out transient events.

As shown in Figure 6-4a, the ΔT signal is generally not in-phase with the reference signal. To avoid interference, the lock-in amplifier separates the detector output S in two components by using the reference signal and its quadrature (90° out-of-phase), as illustrated in Figure 6-4b. Since adiabatic structural response is expected to be in-phase, heat conduction will cause a phase shift that will be apparent as an out-of-phase component in the detector signal.

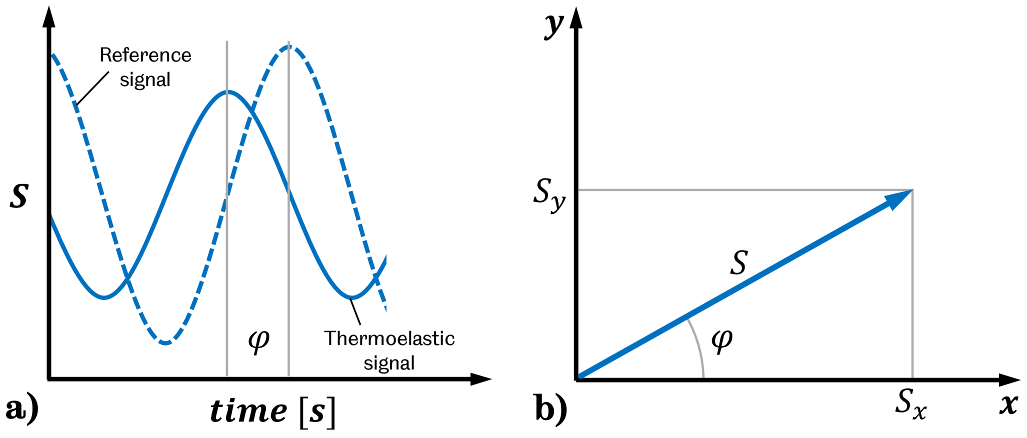

Figure 6-4. TSA data acquisition format

It should be clarified here that the phase angle between the reference signal and the detector signal can be set arbitrarily by the user. Therefore to validate adiabatic conditions, or perhaps to observe non-adiabaticity, it is common to adjust the phase so that regions of uniform stress, i.e. far-field zones away from stress gradients are in-phase with the TSA image; which is commonly known as “phasing-in” the data. It can then be seen how two descriptions of the TSA signal are equivalent, namely the Cartesian (S_x, S_y) and polar (S, φ) shown in Figure 6-4b.

The different responsivities of individual pixels, which are a natural consequence of variations in the doping of the semiconductor elements [118] and electronic architecture of the sensor array, cause systematic errors in the measurements. Thus, before taking measurements the FPA sensor needs to undergo a non-uniformity correction (NUC). To perform the NUC, a body of constant thermal illumination, e.g. a blackbody or a gray body with constant emissivity, is captured and used to normalize the whole sensor against a known temperature.

The calibration object is typically a flat metallic plate with the same emissivity as the test surface. To correct for both offset and sensitivity variations, two captures at different temperatures are needed; this is known as a two-point correction. By correcting the offset in the array (first capture), the detector signal can be related to the temperature of the test surface. Then, by correcting for sensitivity (second capture), a proportionality constant is obtained to relate the change in detector signal to the change in temperature of the test surface, i.e. ΔT. However, the response of the infrared detector to temperature is not, in general, a linear function. To compensate for this, manufacturers offer multi-point radiometric calibrations for each lens. This was not an option for the DT1410 system, since degradation in the electronic A/D channels of the sensor changed the initial detector signature at every start-up of the camera head. To minimize sensitivity errors, the two-point correction was done over a temperature range comparable with the expected variation of the specimens, namely, 25 – 35 °C for the current work.

6.5.2 Optimization of TSA capture for CFRP laminates

In order to improve the quality of the TSA data, parameters such as (i) test surface preparation, (ii) loading frequency and (iii) magnification were investigated. A single un-notched specimen with a $[-45/0/+45/90]_{2S}$ quasi-isotropic layup was used to investigate the effect of the paint coat on the specimens, loaded at 20 kN with $R = 0.1$. It was assumed that no damage developed during the parametric studies, as these load levels realize less than 30% of the average compressive strength as found by static testing (see Section 5.3). To arrive at the optimal parameters, the specimen was tested at increasing loading frequency whilst acquiring TSA data. Then the effect of frequency, paint coat thickness and magnification on the TSA signal magnitude and phase was evaluated. For consistency, measurements were taken at the central 25 mm^2 square area of the specimen.

The specimens used in this work had a highly reflective surface so that it was not possible to use them unpainted for TSA testing. Therefore, a coat of RS matt black spray paint had to be applied to improve and make the surface emissivity even. As discussed in Section 6.4.2, a *coat* of paint can only be defined in relation to the person applying it and, in doing so, it is argued that consistency between applications is paramount to prevent introducing significant variation in the measurements.

A full characterization of the thermal response of the paint coat, i.e. the thermal response of measured paint thicknesses at various frequencies for the subject substrate against theoretical predictions, as per Robinson et al. [131], was out of the scope of this work. Instead, a *coat* of paint is defined for the purposes of this work as the least amount of paint needed to completely wet the test surface when spraying at a standoff distance of 20 – 30 cm as gauged visually by the operator. It is also worth noting that the standard cap of the RS spray paint was prone to producing an uneven finish, instead a LC6 cap, as described in Section 5.2.2 was found to produce a more consistent finish.

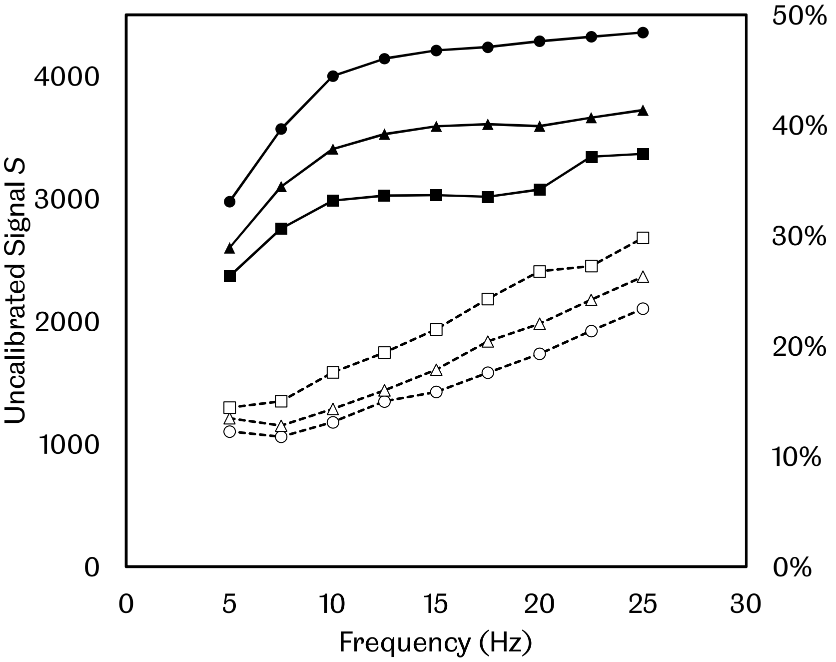

Figure 6-5. Average uncalibrated TSA signal S (——) and standard deviation as a percentage of S (- - -) for different paint thickness levels vs loading frequency. Measurements were taken from the central 25 mm^2 area in an un-notched specimen loaded in compression at 20 kN with R = 0.1. Thickness levels are 1 coat (●/○), 2 coats (▲/△) and 3 coats (■/□).

The specimen was loaded at frequencies of 5 – 25 Hz in steps of 2.5 Hz. To prevent transient effects from the change in frequency, TSA measurements were taken 1 min after the increment. To minimize noise, 10 captures with a 30 seconds integration time were taken at each frequency. The process was repeated for 2 more paint applications, maintaining the same orientation of the specimen in the fixture. The average and standard deviation of the total

TSA signal at the central 25×25 mm^2 area was taken from each capture, to avoid thermal gradients due to edge effects of the laminate and from heat conduction at the fixture clamps. Then, the averages of each 10 frame capture set were used to construct the curves shown in Figure 6-5.

It can be seen that the change in temperature is significantly affected by both paint thickness and frequency. More than one application of paint is found to attenuate the TSA signal and the response to frequency appeared to be asymptotic, with the TSA signal increasing rapidly up to 12.5 Hz and then more gradually; the same trend was observed at all coat thicknesses. The standard deviation of the measurements is seen to increase with paint thickness and to increase linearly with frequency.

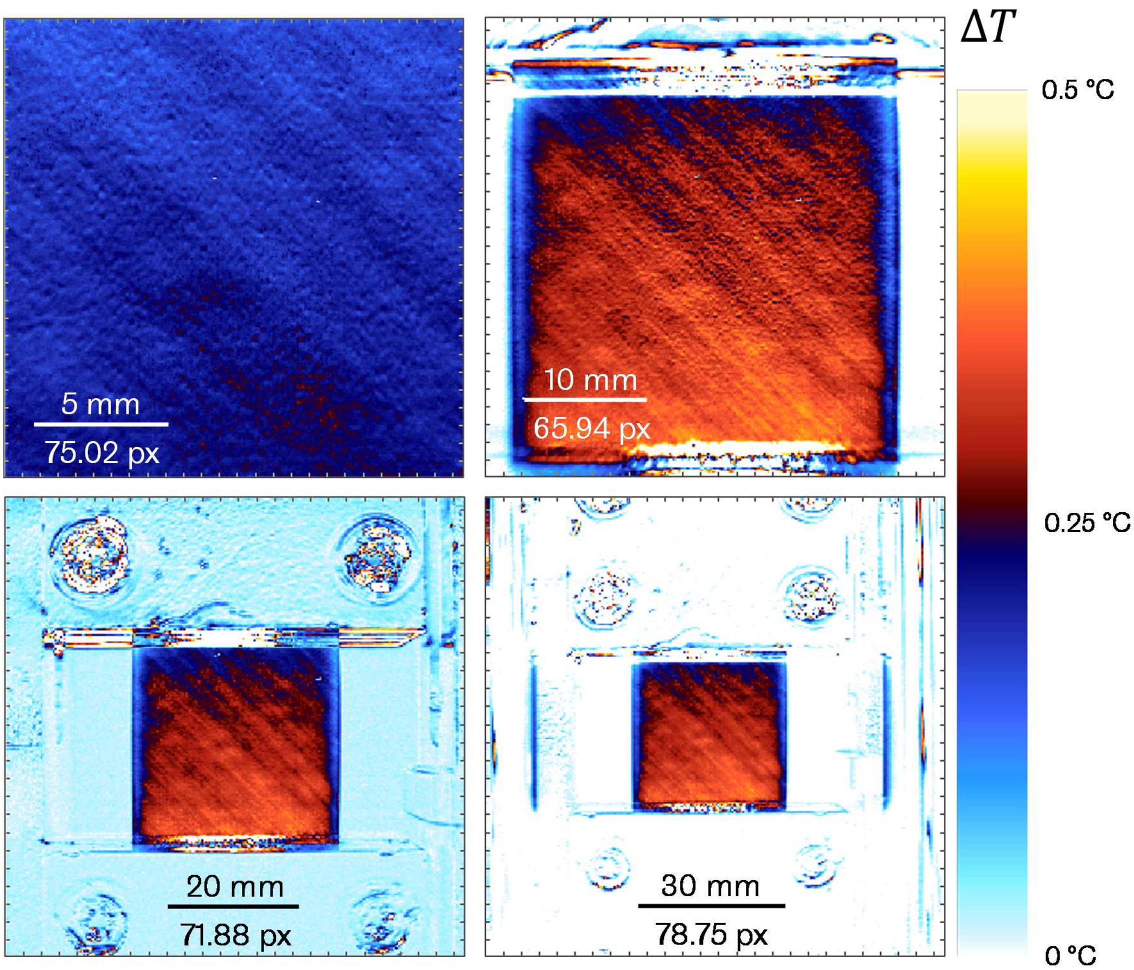

Figure 6-6. Absolute temperature change maps with different magnification in un-notched specimen loaded in compression at 20kN with R = 0.1. The highest magnification (top left) is from a zoom lens and the other 3 from a 25 mm f2.3 lens at different standoff distances.

Next, the effect of motion blur on ΔT from 4 levels of magnification was investigated, as shown in Figure 6-6. A zoom lens was used to capture a 17 × 17 mm^2 FOV, i.e. 15 px/mm, at the centre of the specimen and a 25 mm lens to capture the whole specimen visible area at 6.6 px/mm, 3.6 px/mm and 2.6 px/mm. Average and standard deviation measurements were obtained using the same procedure as in the coat thickness vs. frequency study, with the exception of averaging the whole FOV of the zoom lens captures. The curves obtained are shown Figure 6-7.

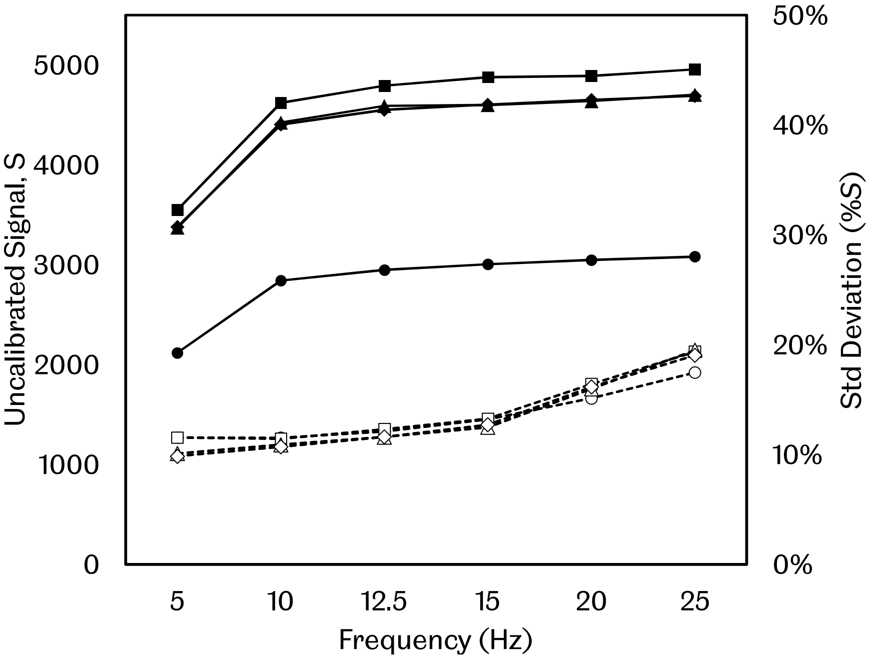

Figure 6-7. Average uncalibrated TSA signal S (——) and standard deviation as percentage of S (- - -) for different magnification levels vs loading frequency. Measurements were taken from a 25 mm^2 centre area in an un-notched specimen loaded in compression at 20 kN with R = 0.1. Magnification levels are 15 px/mm (●/○), 6.6 px/mm (■/□), 3.6 px/mm (▲/△), 2.6 px/mm(◆/◇).

It was found that the zoom lens attenuated the TSA signal considerably in comparison with the 25 mm lens. This was expected due to the lower transmittance of the zoom lens, which is a consequence of the longer optical path. For the three magnifications with the 25 mm lens the magnitude of ΔT remained relatively unchanged, with only the 6.6 px/mm marginally larger. The standard deviation was found to be independent of magnification. It should be noted that the specimen was repainted with one coat of paint for this study, with the intent to verify the frequency response. The same trends of ΔT and standard deviation with increasing frequency as in the paint coat study were observed.

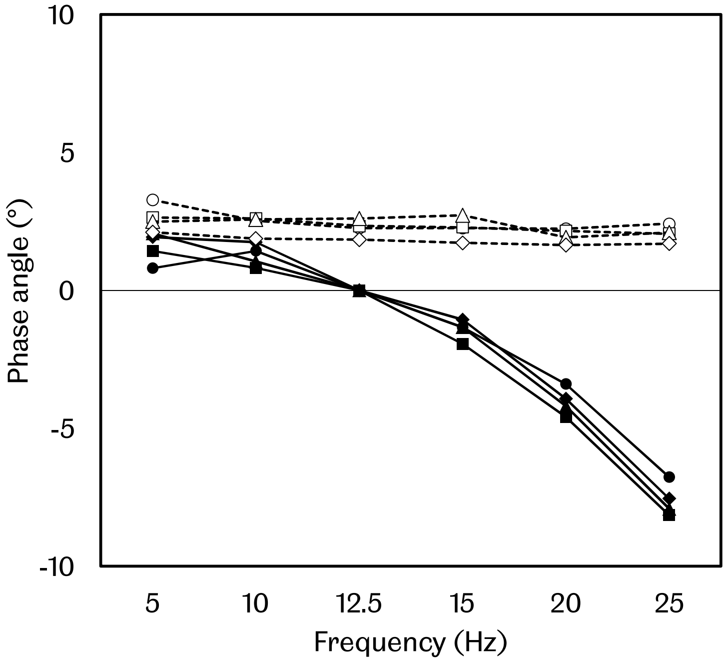

Figure 6-8. Average phase angle (——) and standard deviation (- - -) for different magnification levels vs loading frequency, relative to phase at 12.5 Hz. Measurements were taken from a 25 mm^2 centre area in an un-notched specimen loaded in compression at 20 kN with R = 0.1. Magnification levels are 15 px/mm (●/○), 6.6 px/mm (■/□), 3.6 px/mm (▲/△), 2.6 px/mm(◆/◇).

Lastly, the effect of magnification and frequency on the phase angle was investigated as shown in Figure 6-8, which contains curves of average phase and its standard deviation for the 4 magnification levels vs frequency. The 12.5 Hz frequency is used as the reference phase. The phase angle was observed to depend only on frequency with the standard deviation remaining constant. A 10 degree difference from 5 to 25 Hz was observed, which would translate into a relative change of ~17% in the out-of-phase component. These trends in combination with the monotonic increase of ΔT with frequency, as shown in Figures 6-5 and 6-7, suggest that the loading frequency is not sufficiently high to avoid significant interlaminar heat transfer, as predicted by Wong in [128]. Since a 25 Hz loading frequency is near the maximum attainable operating conditions of the servo-hydraulic frame used in the current work, interlaminar heat transfer was unavoidable. However, the subsurface thermal gradients can be used to observe damage propagation, as will be shown in the results presented in Section 6.6.

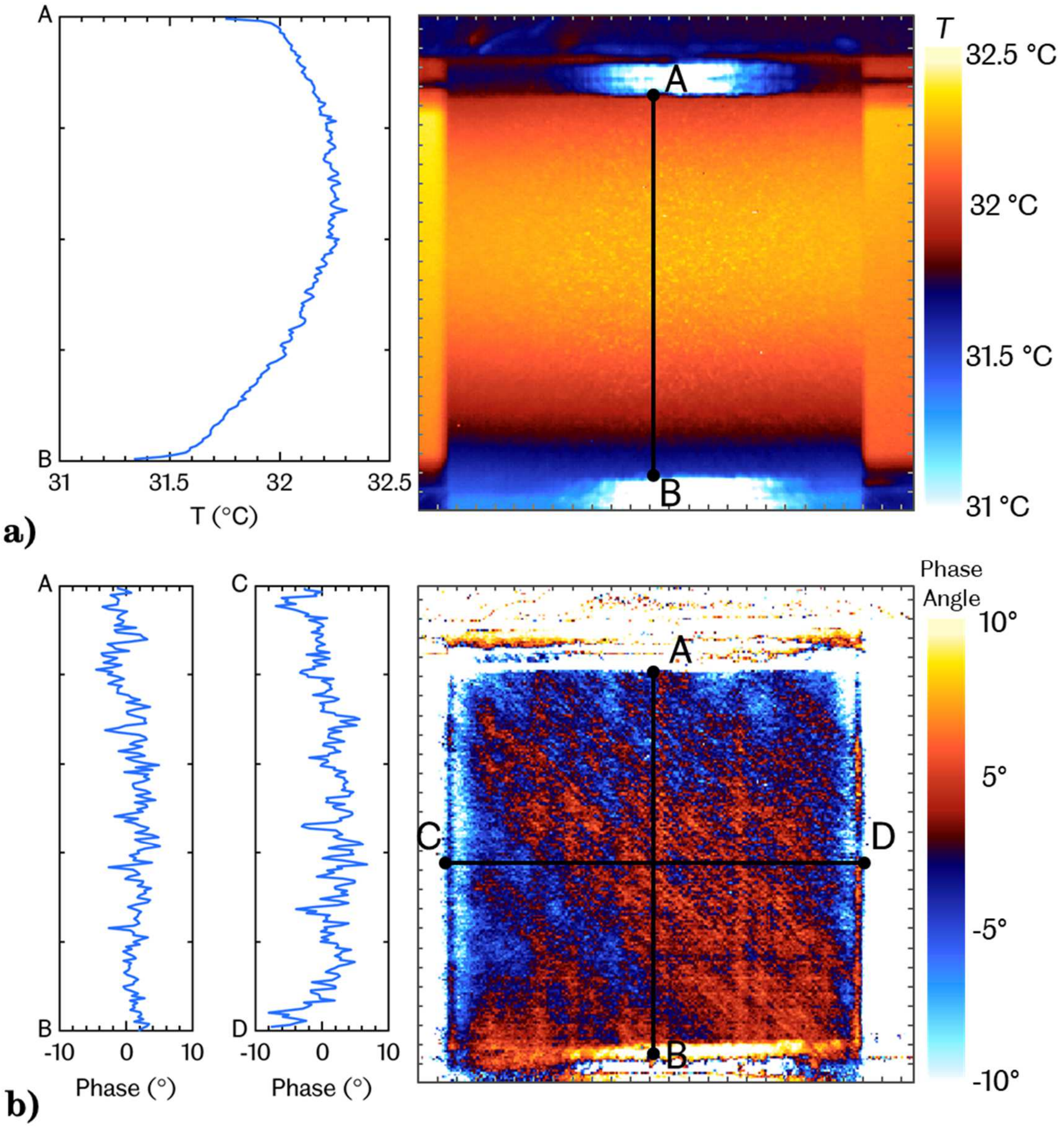

Figure 6-9. (a) Map of temperature distribution from an un-notched specimen with the vertical midline interrogated to show the thermal gradient due to contact with the fixture clamps. (b) Phase map from an un-notched specimen after it has been phased-in using the average of the central 25 mm^2 area. A 12.5 Hz loading frequency was used for these captures.

To quantify the effect of heat transfer from the fixture clamps and interlaminar stresses, profiles of temperature and phase were obtained from the validation specimen loaded at 12.5 Hz, as shown in Figure 6-9. Datasets were phased-in with the 25×25 mm^2 central area. A difference of up to 2 °C can be observed between the centre of the specimen and the clamping area, as shown in Figure 6-9a, which caused the phase offset seen at the vertical profile (AB) of Figure 6-9b, albeit partly obscured by what appeared to be variation due to material heterogeneity. This latter variation can be seen as 45° and vertical bands in the phase image of Figure 6-9b. This further supports the theory that the surface thermoelastic signature is a combination of the 2 outer plies.

Due to the need to refill the camera with liquid N_2, it was desirable to use a high frequency to accelerate failure enough for a practical test duration but without introducing spread in the measurements. Supported by findings of the validation studies described above, it was decided to:

- Apply a single coat of spray paint to prepare the specimens,
- load the specimens at 12.5 Hz and
- use the 25mm lens at a magnification of 6.6 px/mm.

The magnification is equivalent to a spatial resolution 0.152 mm/px. The maximum displacement observed from static tests of the OHC specimens at ~80% of the failure load is approximately twice the pixel scanning area. Thus, a compromise was made between spatial resolution and thermal gradient resolution. The decision to use this magnification was made based on the expectation of low signal intensities at the locations where damage was expected to nucleate, i.e. east and west of the notch.

6.5.3 Dynamic 2D–DIC setup

In order to recover a continuous signal from discrete-time samples, Shannon's theorem [144] states that the sampling frequency should at least be twice that of the signal to be recovered, this is known as the Nyquist or critical sampling frequency. When the sampling frequency is less than Nyquist, the original signal cannot be recovered and is instead aliased. The 1st harmonic of the aliased folding frequencies $f_{perceived}$ can be found as

$$f_{perceived} = f \pm \left| f - f_s \cdot \mathrm{nint}\left(\frac{f}{f_s}\right) \right| \tag{14}$$

where f is the signal being recovered, f_s is the sampling frequency and nint indicates the nearest integer function.

Since CCD cameras used in conventional DIC systems can only attain sampling rates of the order ~$10^{0.5} - 10^{1}$ frames per second, their application to capture dynamic tests poses a challenge. In the context of the current work, most fatigue tests in composite testing are run at frequencies in the range of 5 to 30 Hz, so it can be seen how meeting the requirement of Shannon's theorem is often not possible. Nonetheless, there is the possibility of using subsampling of the loading signal to recover oscillations of the deformation field capture with DIC. This is possible because both the loading and sampling frequencies are known. Therefore, by judiciously selecting the capture rate, the recovered signal can sample the peaks and troughs of the deformation cycles, which are the points of most interest.

The use of relatively low frame rate cameras to capture constant amplitude cyclic tests with DIC has been reported in the literature before. Giancane et al. [145] used subsampling of a 9.5 Hz loading signal at 5 fps to capture images at an aliased frequency of 0.5 Hz and obtain DIC deformation maps of E-glass/epoxy laminates under tensile fatigue. Fruehmann et al. [146] used a lock-in amplifier to capture a so-called Brazilian disc (i.e. a flat disc in diametrical compression) loaded at 7.1 Hz and 21.1 Hz at a capture rate of 2 fps The same technique was also used in [146], [147] to observe crack growth in a metallic T-shaped specimen under tensile fatigue.

Of the two approaches aforementioned, the use of a lock-in amplifier is the most robust and was demonstrated to improve the strain resolution of static tests at corresponding load levels. This was achieved by integrating a number of images in a similar manner to TSA and comparing the integrated strain fields between cycle intervals throughout the fatigue test. By using this integration scheme, the authors in [146] show that there is a trade-off between the quality of the obtained strain fields and the ability to resolve damage growth. Thus, the fatigue test frequency can be increased insofar damage growth is slow enough during the DIC integration period to avoid introducing error due to poor correlation of the image set pairs. For cracks in metallic specimens, damage growth is relatively steady and self-similar, making the application of a lock-in amplifier for DIC an effective solution to the low capture rate of conventional CCD cameras in DIC systems.

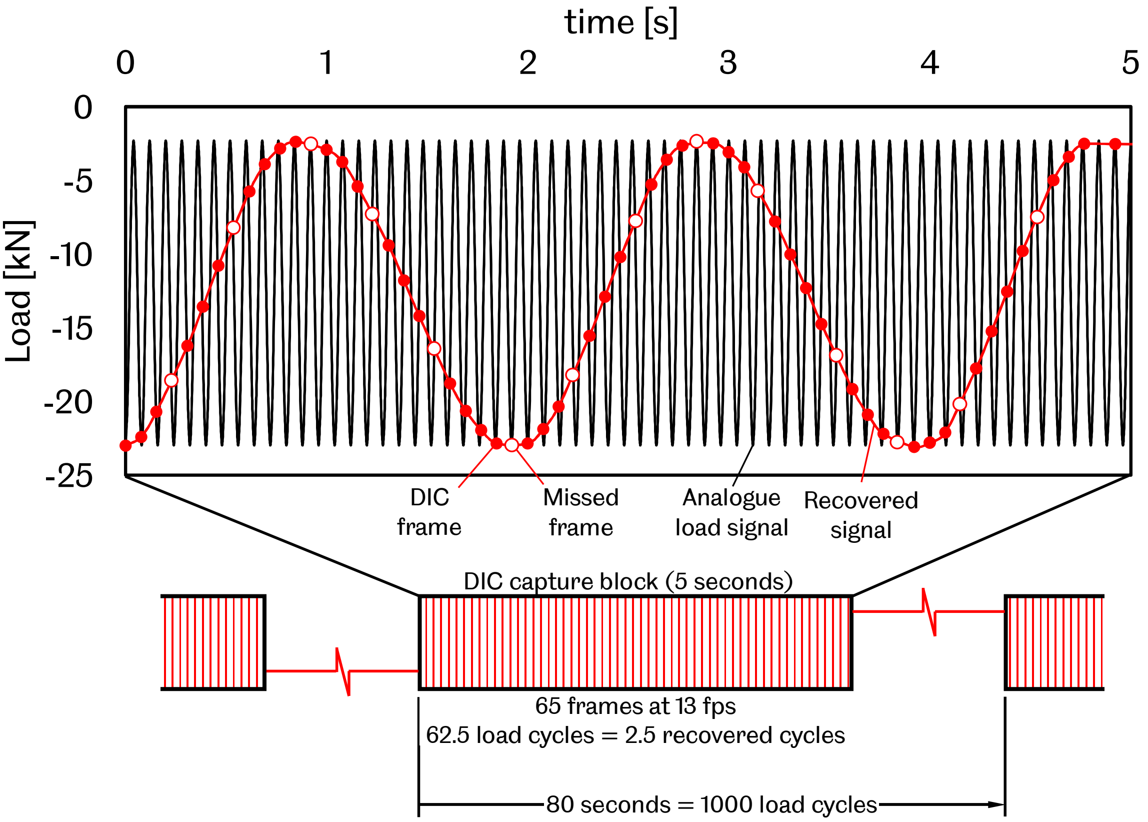

Figure 6-10. Illustration of DIC capture procedure use to recover deformation cycles in OHC fatigue tests by use of subsampling. Blocks of 50 frames acquired at 13 fps are triggered every 80 seconds, which is equivalent to 1000 loading cycles at 12.5 Hz. Each capture block comprises 62.5 loading cycles, from which 2.5 oscillations of the deformation field are recovered.

Compressive damage in composite laminates is diffuse and grows irregularly as reported in literature review (Chapter 2) and observed from static testing (Chapter 5) of the subject systems in this work. Also, the damage growth rate is discontinuous and depends on the occurrence of different damage mechanisms and their interactions. The results from Section 5.3.3 suggest that the collapse of kink bands in the 0° plies lead to the development of crush zones that precede delamination in the laminate. Thus, the sudden changes in the deformation field of the OHC specimens preclude the use of the integration scheme presented in Fruehmann et al. [146] without introducing significant error in the measurements.

To enable the observation of damage formation in OHC fatigue tests, an alternative capture method was proposed, as shown in Figure 6-10. Namely, the highest attainable capture rate of the AVT Pike F-505 CCD cameras, i.e. 13 fps, was used to subsample the 12.5 Hz test frequency. This recovered an aliased signal of 0.5 Hz with the same amplitude as the test frequency. Capture blocks of 5 seconds (65.5 frames) were triggered every 80 seconds (1000 load cycles) throughout the duration of the test. At the start of the fatigue tests the load is ramped from the minimum fatigue load level to the mean load before the servo-controller starts applying cyclic load. Then the start of the capture train was triggered manually an instant before the cyclic loading started. This allowed to obtain the cycle count of each frame within 1/13 cycles). Figure 6-10 shows an actual capture block superimposed on the corresponding analogue loading signal; values of load vs time from the acquired frames are indicated as red circles. Buffering limitations of the CCD cameras digital readout resulted in skipped captures every 3 to 4 frames. It can be seen, nonetheless, that load oscillations can be recovered with sufficient detail.

For this methodology to be viable, it was paramount to minimize the contribution of motion blur to the uncertainty in the deformation maps obtained from DIC. That is because any motion comparable to a pixel size at the prescribed magnification will result in blurring of intensity gradients, i.e. image texture, during the frame exposure time. Consequently, the exposure time of the frame needs to be set in proportion to the pixel size at the highest displacement rate within the FOV. A short exposure time poses another difficulty, namely, that more illumination is needed to make use of the full dynamic range of the sensor. This in turn, needs to be balanced with the lens aperture needed to minimize errors due to out-of-plane displacement.

The maximum exposure time needed for a material point to displace no more than 1 pixel can be calculated as

$$exposure\ [\mathrm{s}] \leq \frac{1}{\dot{U}} \left[\frac{\mathrm{s}}{\mathrm{px}}\right] \tag{15}$$

where $\dot{U}[\mathrm{px/s}]$ is the displacement rate in pixels per second at the prescribed magnification, which can be calculated as

$$\dot{U} \left[\frac{\mathrm{px}}{\mathrm{s}}\right] = \dot{U} \left[\frac{\mathrm{mm}}{\mathrm{s}}\right] \times magnification \left[\frac{\mathrm{px}}{\mathrm{mm}}\right] \tag{16}$$

6.5.4 Experimental Method

From the OHC static testing results it can be seen that only the T3 system exhibited a comparable resistance to the development of crush zones at the hole edge, as discussed in Section 5.3.4. For this reason and due to the time scale of each fatigue test in the context of the research programme, it was decided to investigate the BL and T3 systems only.

To obtain a measure of statistical significance between the two systems, 10 specimens from each were fatigued to failure under compression: 7 using TSA and 3 2D-DIC. Each specimen was fatigued under load control at 80% and R = 0.1 of the system's mean compressive strength at a frequency of 12.5 Hz. Load and displacement analogue data was acquired only at the turning points (peak and trough) of each cycle to construct the stiffness history of each specimen. It should be noted that the displacement data is independent of the load train compliance, as it was acquired with the 3 mm LVDT.

For TSA, the capture interval was set at 16 seconds or 200 cycles at 12.5 Hz but due to inconsistent timing of the frame grabber as controlled by the TSA PC, captures were, in fact, taken approximately every 211 cycles. The TSA integration for each ΔT capture was set to 16 seconds at the maximum frame rate (140 fps) with an exposure time of 1 ms. The Deltatherm system can acquire direct temperature maps simultaneous with the ΔT acquisition and so,

T maps were also captured with integration periods of 8 seconds. The capture rate and the durations of the integration period were selected with the intent to capture the occurrence of damage events and locate them in the specimen life as accurately as possible. This in order to compare different strategies to assess damage development in the OHC specimens. Then, both settings of the integration period were the minimum allowed by the DeltaVision software. TSA specimens were prepared as per Section 6.5.2.

For the 2D–DIC acquisition, inspection of 3D-DIC data sets from static testing indicated that the largest displacement at the top of the FOV for the load range (peak to trough) was ~0.37 mm. This is equivalent to a maximum displacement rate of 14.6 mm/s at the zero crossings of 12.5 Hz frequency displacement oscillations. The magnification used for the 2D-DIC capture was ~47 px/mm. Thus, in order to avoid motions larger than 1 pixel an exposure of $\leq$ 1.47 ms needed to be set. The CCD cameras allowed for a minimum exposure time of 27 μs. Sufficient illumination was procured to obtain the best contrast attainable from the sensor's dynamic range with a 50 μs exposure, which is almost 30 times less than the required level calculated above. The capture method is as described in the previous section and specimens were prepared in the same way as for the static tests with 3D–DIC (Section 5.2.2).

6.6 Results

After completion of the test campaign and inspection of the different datasets collected, it was found that all OHC specimens exhibited a similar progression of damage, independent of material system. Due to the large amount of data collected it was not possible to include details of each individual fatigue test. Instead, datasets with the most salient features are presented and discussed. Namely, 1 BL specimen (failed at 10,560 cycles) and 1 T3 specimen (failed at 37,722 cycles) are shown as captured by TSA and DIC, respectively. Analogue data acquisition for the whole fatigue test campaign can be found in Appendices B and C, for the BL and T3 system, respectively. Several methodologies for the assessment of damage are presented and compared (Sections 6.6.1 to 6.6.3). In turn, a statistical analysis of the specimen life data of the whole campaign is performed to evaluate the effect of interleaving in the compressive fatigue performance of CFRP notched laminates (Section 6.6.4).

6.6.1 Damage assessment of OHC fatigue with TSA

Temperature profiles

From the TSA measurements, it was found that the temperature distribution maps alone can provide evidence of the damage processes in OHC fatigue. A horizontal interrogation line that cuts through the centre of the specimen, as indicated in Figure 6-11b for the first TSA capture, was used to construct a temperature profile history for a full test as shown in Figure 6-11a. Each row in figure (a) was extracted from single captures of a BL specimen that failed at 10,560 cycles. The first row corresponds to the temperature profile of the unloaded specimen, for reference.

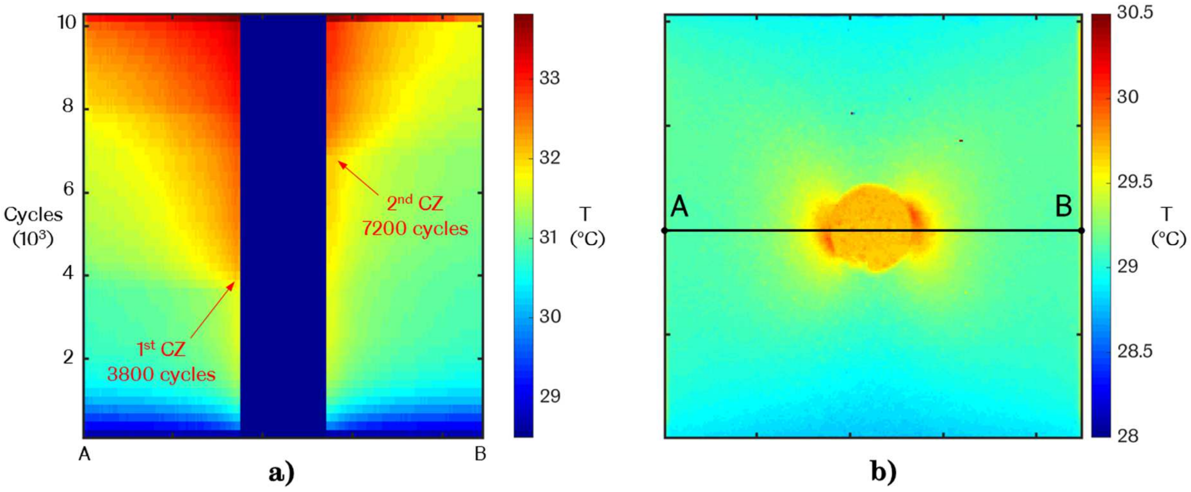

Figure 6-11. a) Temperature profile history from the horizontal midline of an OHC specimen; every row represents approximately 211 cycles. B) Temperature distribution map at first frame (~211 cycles) and interrogation line for profile history (a). The subject specimen was from the BL system and failed at 10,560 cycles.

It can be seen (Figure 6.11b) that the maximum temperature reached at the vicinity of the notch is only ~5.5 °C higher than the bulk temperature at the start of the test. This is not the same as the local temperature at the damage process zones at the micro scale due to the sensor resolution being several orders of magnitude larger. It is however, evidence that the bulk temperature of the specimen does not change significantly with respect to typical the T_g of epoxy resins. For practical reasons, in-service load regimes are rarely at frequencies comparable with the ones used in fatigue tests and so, it is important to substantiate the assumption that the material properties are equivalent between the fatigue tests and a structure in service. The sudden increases in temperature gradient at ~3800 cycles and ~7200 cycles indicate the rapid development of damage at the left and right edges of the hole, respectively. At imminent failure the left side of the specimen approached a uniform temperature distribution, which was indicative of damage extension to the edge of specimen.

Thermoelastic maps

Maps of the in-phase and out of phase components of the thermoelastic response normalized by temperature $\Delta T_x/T$ and $\Delta T_y/T$, respectively, are shown in Figure 6-12 for the same specimen as the last section. Note that the capture index is shown with the prefix “S” at the left of the image with the number of cycles in parenthesis, which is a multiple of the capture interval –211 cycles. All TSA datasets where phased-in with a 25×25 px^2 area at the lower right corner of the test surface in the first capture. Although this region is not entirely free from stress gradients, this was done for consistency.

The range of captures shown in Figure 6-12, S15 to S18, encompasses the formation of the first crush zone at the left edge of the notch, which is barely visible at S18 (~3800 cycles) as indicated by “CZ”; this corresponds to the left side temperature increase in Figure 6-11. It is notable that the $\Delta T_x/T$ and $\Delta T_y/T$ appear to have the same distribution. Also, that the out-of-phase magnitude at the hole edge location of maximum thermoelastic response is ~25% of the in-phase response. The large phase difference between the far-field and the hole edge was expected, as the large stress gradients in the vicinity of the notch are bound to produce acute thermal gradients. However, by using a far-field region as a zero-phase reference, the thermoelastic signal is attenuated by effectively splitting in two components with comparable magnitude.

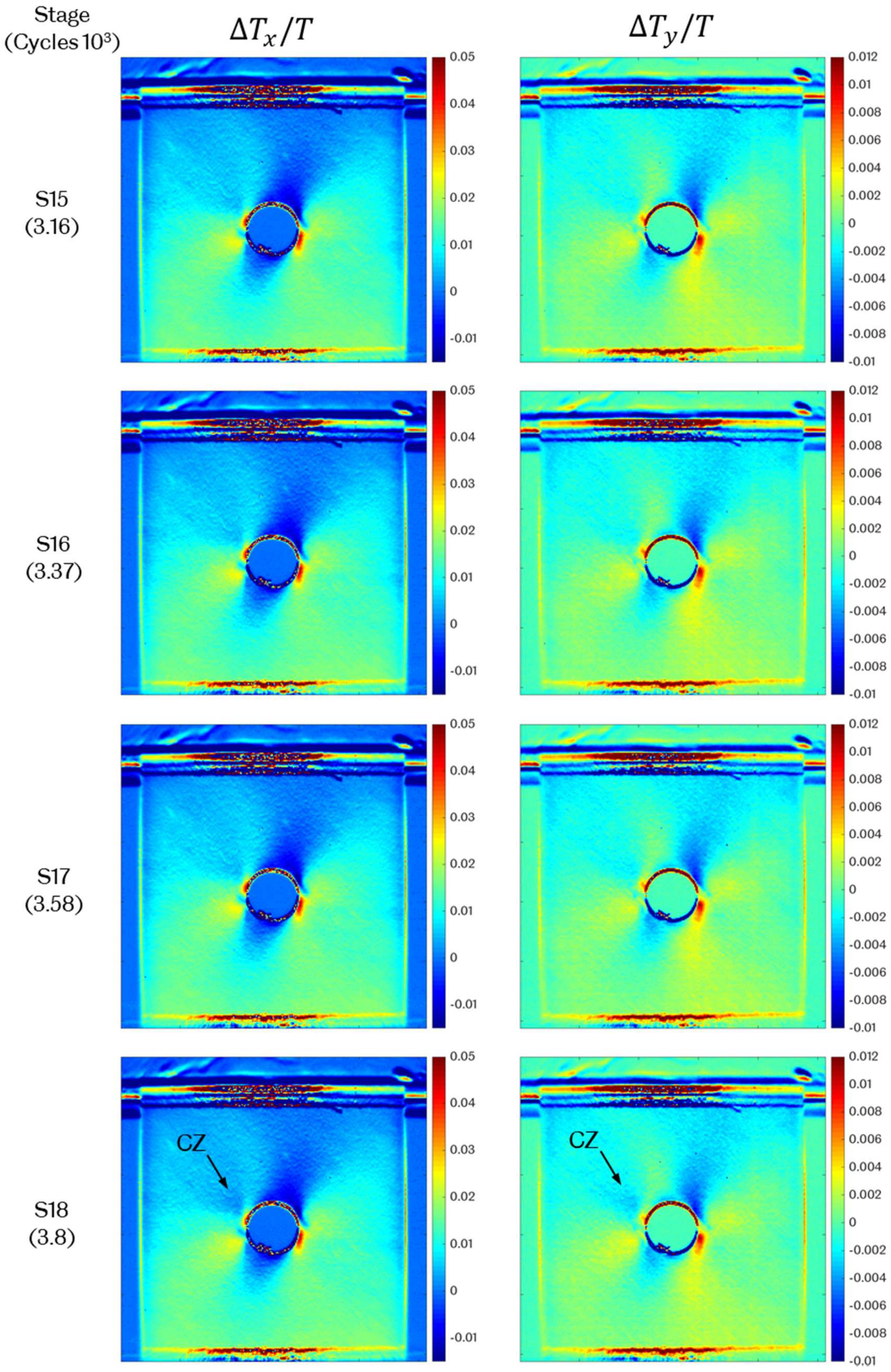

Figure 6-12. Maps of in-phase and out-of-phase normalized temperature change for a BL specimen to show the development of a crush zone (CZ) at the hole edge. The stage index is equivalent to multiples of ~211 cycles.

Thermoelastic capture differentials

To aid the observation of the development of damage, an alternative method is proposed whereby subtracting every pair of captures, changes in the thermoelastic maps pertaining to damage growth are highlighted, as shown in Figure 6-13 for the sequence S16 – S18. The subtraction of each step is done as $S_n - S_{n-1}$, where S indicates a capture stage and n is the stage index. To clarify, the subtraction of captures is termed here interchangeably as "step" or "capture differential". Note that the magnitude of the gradients uncovered is small and thus the scale had to be adjusted accordingly to improve contrast.

The development of damage is visible as early as in the 15/16 step, as very faint (of the order of 1×10^{-3} °C) but localized spots at the left and right edges of the notch. The crush zone can be seen developing over the next two steps, which comprise as little as 424 load cycles. The sudden development of damage justifies the requirement for short integration times. Also, the negative magnitude of the subtracted signal indicates that there is stress relaxation at these zones, which is in agreement with the strain maps obtained from static testing (Section 5.3.3). Then, upon the full development of the crush zone (S17/18), stress redistribution about 5 times larger than the thermoelastic signature at S15/16 is observed. From the relative magnitude of the change in $\Delta T/T$ gradient in S17/18 it can be inferred that the damage process is much localized. Also, the sign reversal in the change in $\Delta T/T$ between the S16/17 and S17/18 steps is indicative of buckling, which results from delamination growth.

This method of obtaining capture differentials is clearly superior to using single captures, in relation to the ability to resolve damage development. However, damage resolution can be further improved by using the total thermoelastic change rather that the in- and out-of-phase components. Figure 6-14 shows a sequence of capture differentials of $\Delta T/T$ spanning the whole life of the specimen. Namely, the first 800 cycles are shown from the S1-4 capture span, the development of the first crush zone from S15-18, the development of the last from S32-35 and imminent failure from S48-49. To capture damage development over a longer period of time the differentials between each capture span are also shown. Two distinct phenomena can be observed from the capture differentials of the first 800 cycles.

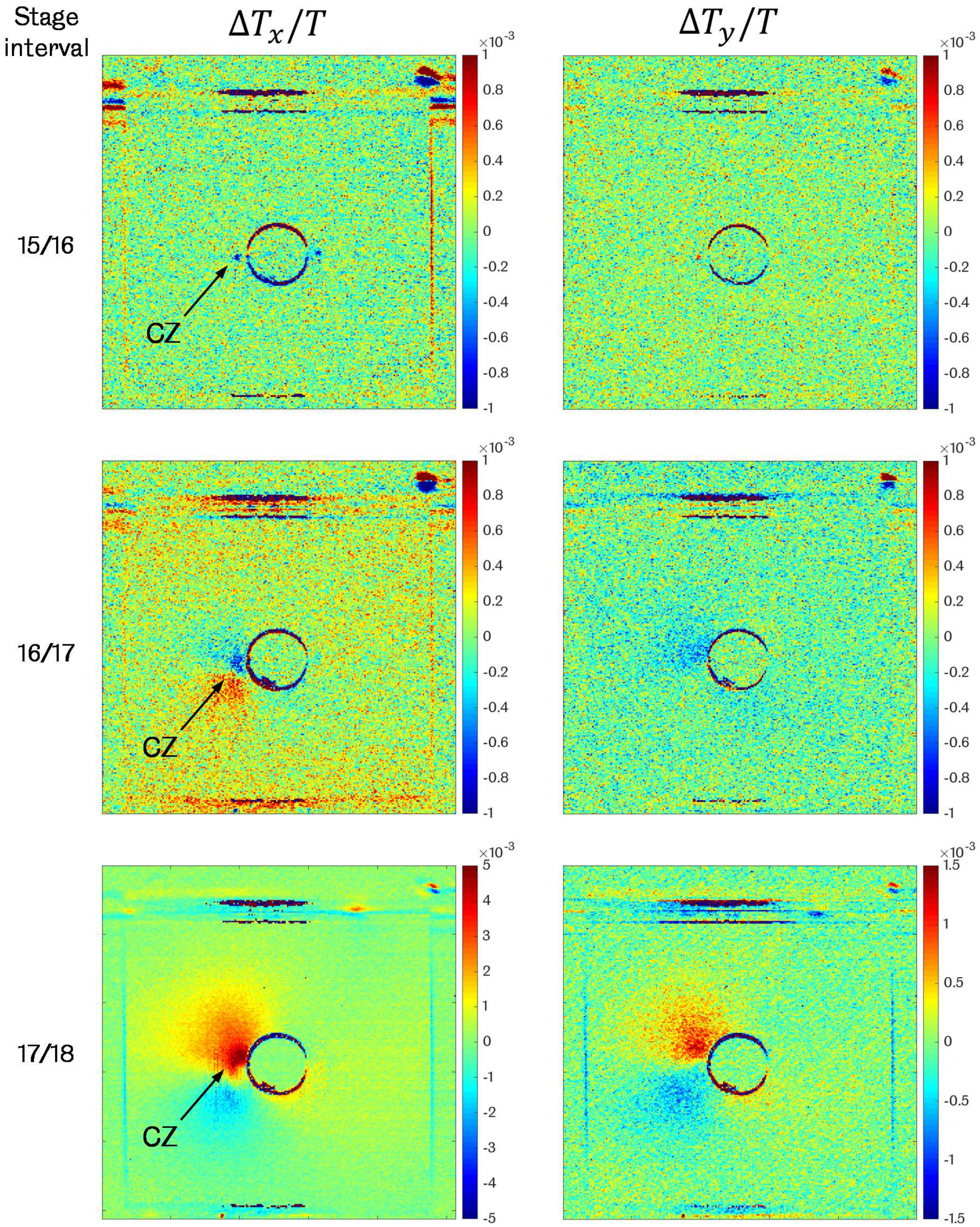

Figure 6-13. Maps of subtracted in-phase and out-of-phase normalized temperature change for a BL specimen to show the development of a crush zone (CZ) at the hole edge. The stage index is equivalent to multiples of ~211 cycles and stage intervals are shown to the left of each map.

The first is a reduction in the bulk stiffness of the laminate as shown by the uniform differences in the zones away from the notch, which is thought to be due to stress redistribution resulting from subcritical matrix micro-cracking. This bulk redistribution consistently occurs over a span of ~1000 cycles at the start of fatigue loading, as will be shown from strain histories presented in Section6.6.3.

The second salient feature is the appearance of large splits, i.e. through thickness matrix cracks, in the 45° surface ply. It is believed that these splits contribute to the softening of the laminate by alleviating the stress concentration at the left and right edges of the notch. From the S4/15 differential it can be seen that until the formation of the first crush zone, damage growth concentrates at the left and right hole edges. The point is made here that obtaining the differential for a longer cycle span is also useful to observe continuous slow damage growth.

The development of the left crush zone is shown again in the S15/18 capture span but with improved contrast in comparison with the previous method. Then, the long span differential S18/32 reveals what is thought to be delamination growth at the interface of the first two plies (+45°/0°), as can be surmised from the reduction in thermoelastic change over this cycle span. The second crush zone at the right edge develops at ~7200 cycles (S34), in agreement with the temperature profile history in Figure 6-11. It is notable that the magnitude of the thermoelastic change during the formation of this second crush zone was significantly lower.

This comparison is shown in Figure 6-15, where vertical interrogation lines along the stress concentrations at the sides of the hole (a) are used to construct the plots of $\Delta T/T$ in (b) and (c) for left and right, respectively. The difference in the magnitude of these steps, suggests that a portion of the fracture energy at the crush zone was absorbed by delamination growth. A faint gradient of annular shape in the S34/35 differential, further supports the theory that delamination growth took place after the 2nd crush zone developed.

1/2

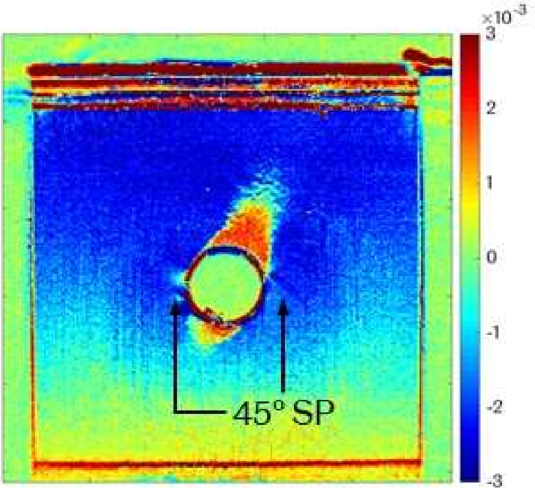

2/3

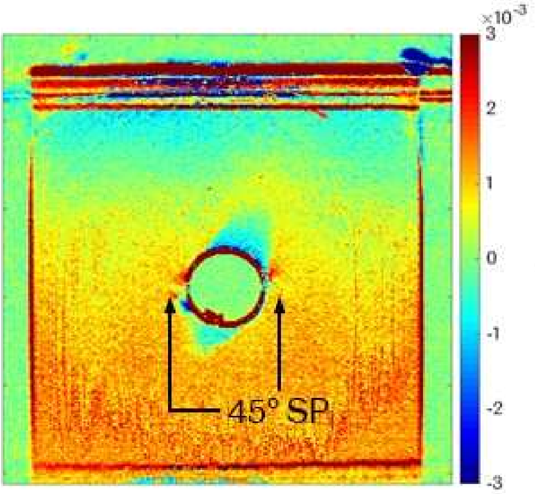

3/4

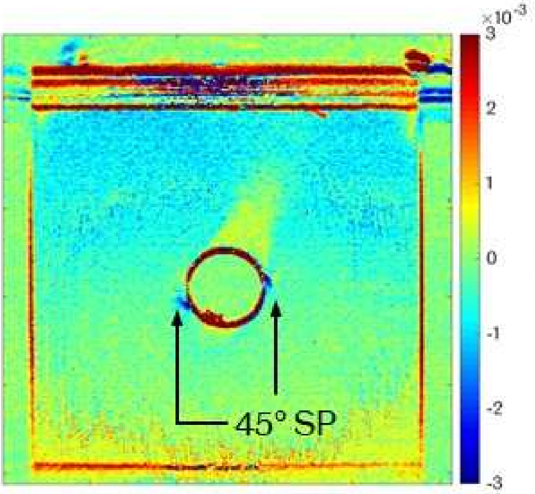

4/15

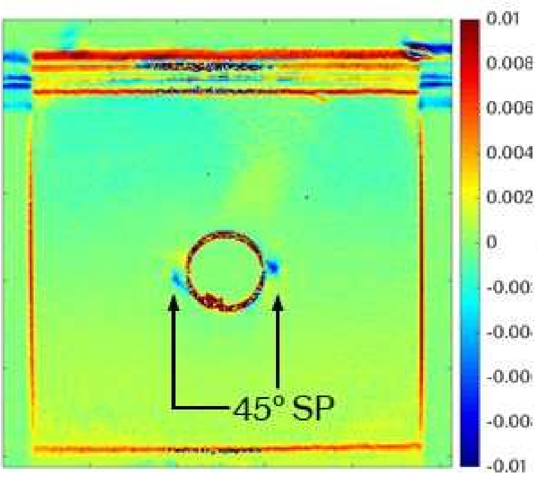

15/16

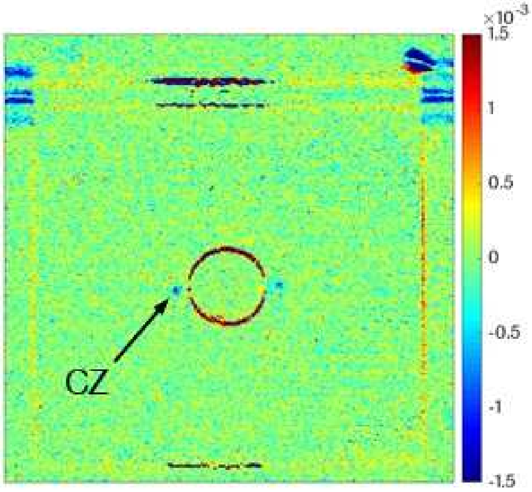

16/17

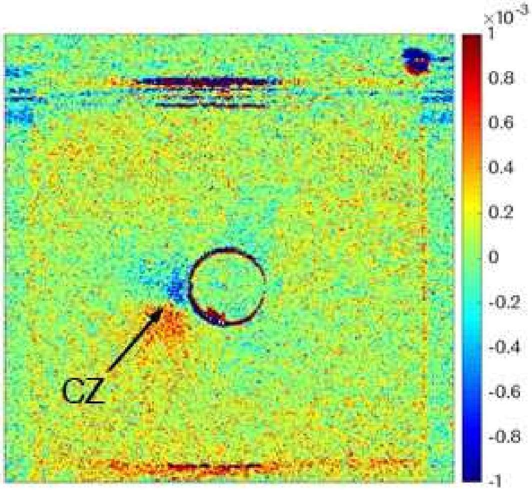

17/18

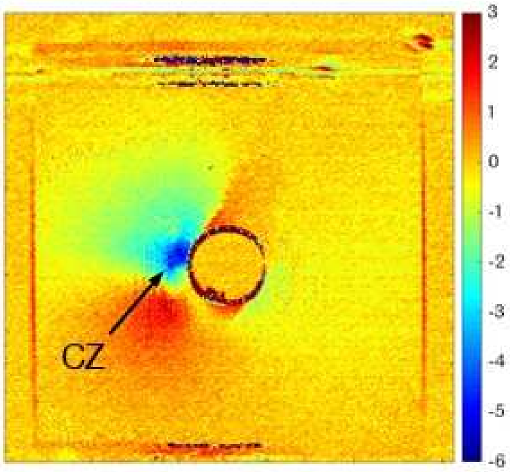

18/32

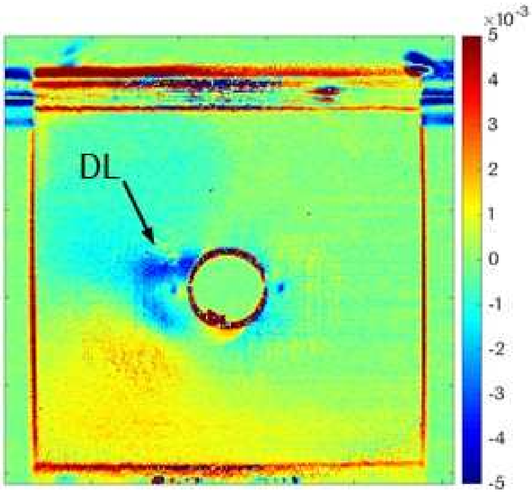

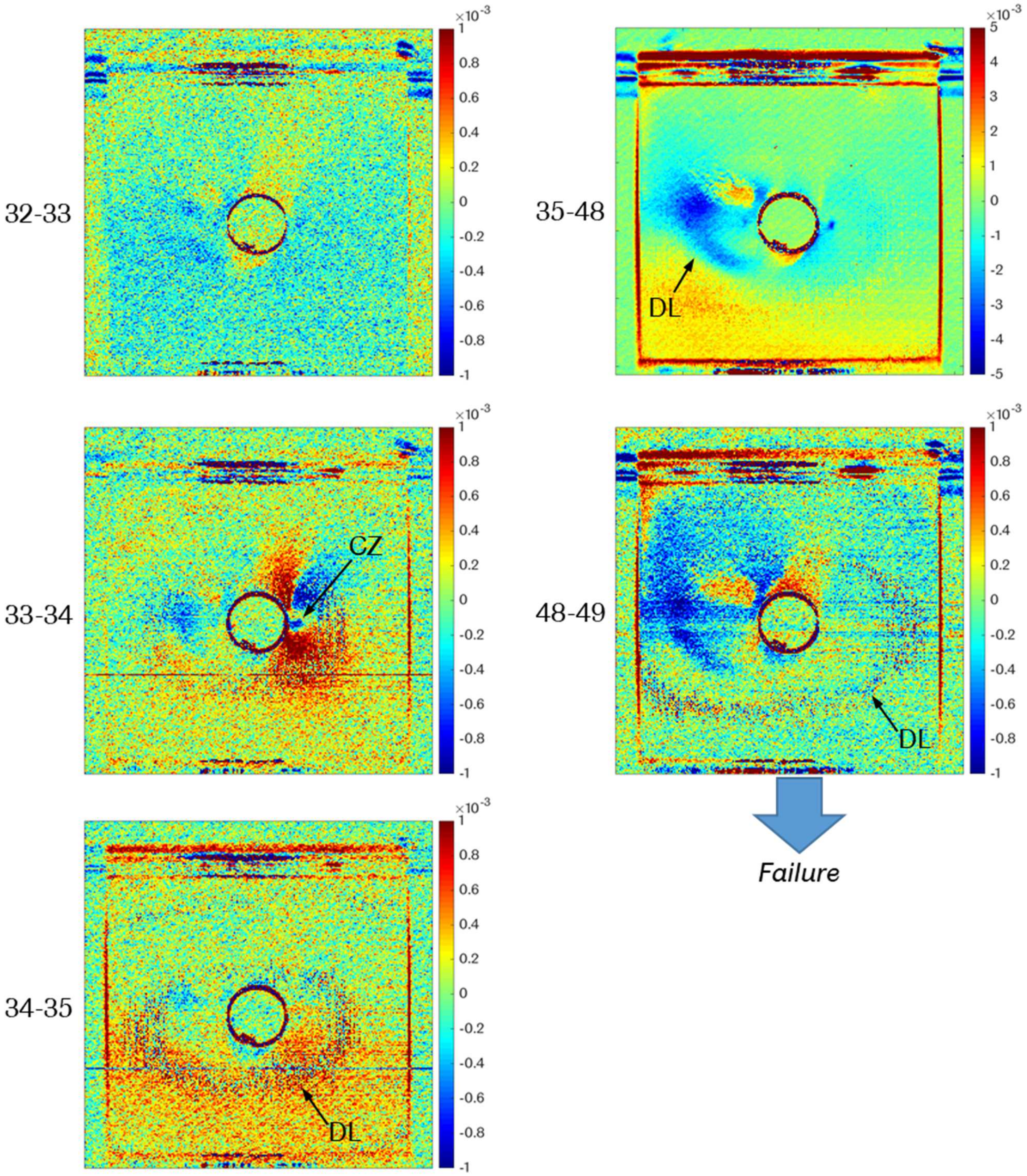

Figure 6-14. Maps of subtracted total normalized temperature change for an OHC specimen to show the development of damage. The stage index is equivalent to multiples of ~211 cycles and stage intervals are shown to the left of each map. Matrix cracks or splits are indicated as SP, crush zones are indicated as CZ and delamination growth is indicated as DL.

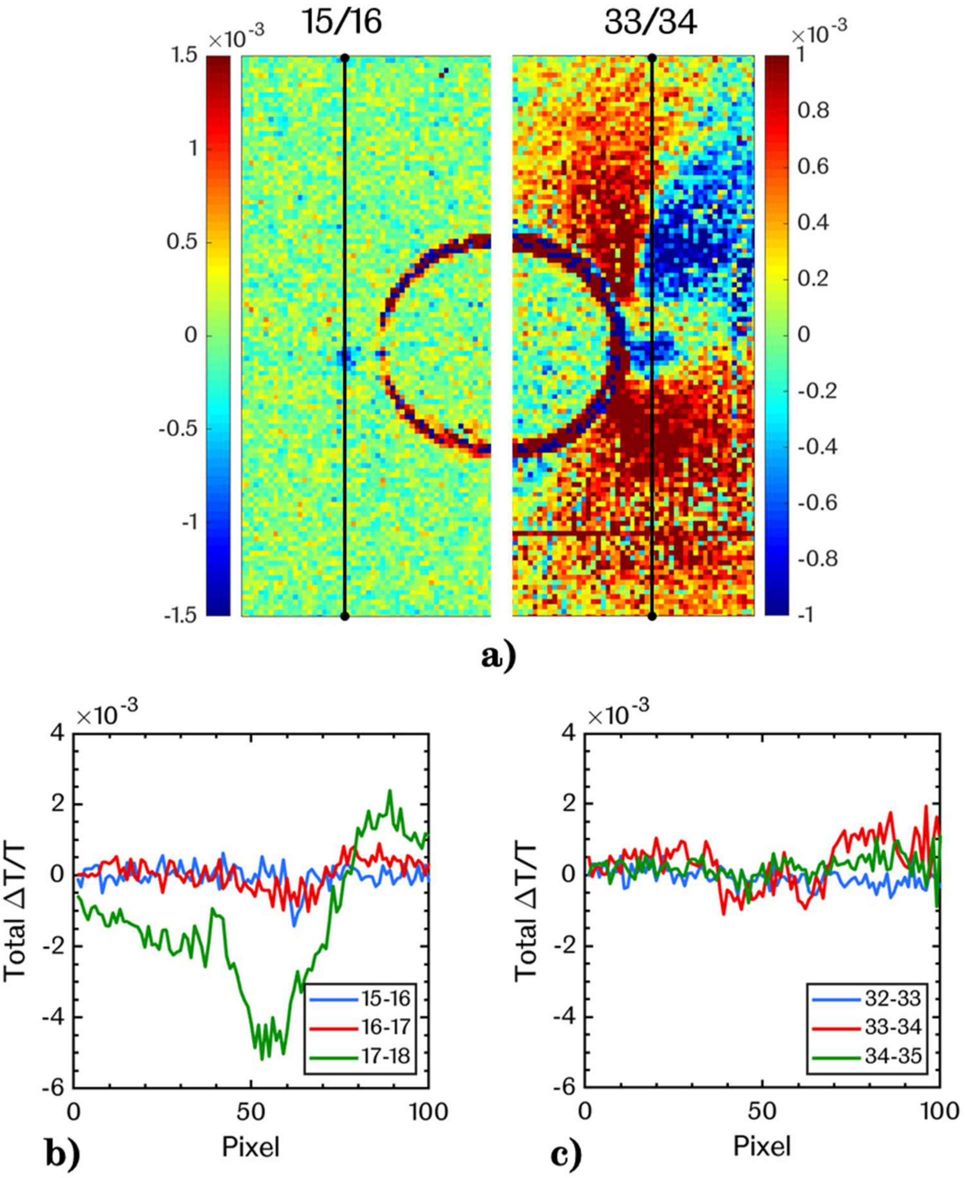

Figure 6-15. Vertical interrogation of the locations where crush zones develop taken from the S15/18 and S32/33 capture spans for the left and right sides, respectively.

For the remainder of its life, damage growth was concentrated at the left side of the specimen as seen from the S35/48 step. The decrease in the thermoelastic change again reveals delamination growth, as in the S18/32 differential. The reasoning for this deduction is that localized buckling at the delamination zones would cause a region of strain softening, which in turn would decrease the thermoelastic signal. Catastrophic failure was caused by the delamination extending to the left edge of the laminate as can be seen from the same annular gradient indicating delamination growth in the last capture differential.

6.6.2 Damage assessment of OHC fatigue using DIC

The stiffness history of the specimen that is used in this section to discuss assessment of damage using DIC is shown in Figure 6-16, for reference. Two quantities are calculated at each half-cycle (peak-to-trough) to construct this history, namely, stiffness and modulus. From the load and displacement analogue data obtained at every turning point of the load signal values of stiffness were calculated as

$$Q_L = \frac{F}{Pk_1 - Tr} \tag{17}$$

where Q_L is the longitudinal stiffness of the specimen, F is the load, Pk and Tr are the peak and trough displacements and the subscript 1 refers to the peak displacement (minimum load level) measured at the first half-cycle. In this manner, the stiffness and modulus history is calculated with the first half-cycle as a reference. Since the displacement turning points were acquired by the 3 mm LVDT from the top platen they can be applied directly to the following expression to calculate modulus

$$E_L = Q_L \frac{l}{A} \tag{18}$$

where E_L is the longitudinal secant modulus, l is the specimen length and A the nominal cross-sectional area, i.e. disregarding the notch. The load-strain response is assumed to be linear and so the right axis in Figure 6-16 is indicated as Young's modulus for consistency with results from the static testing. For comparison, the average modulus from static testing is indicated as a horizontal red line in Figure 6-16.

The specimen in Figure 6-16 failed at 37,722 cycles and, similar to the specimen in the previous section, underwent a sudden stiffness drop with the development of the first crush zone at ~ 26,600 cycles. This marked the onset of delamination growth which is shown as a steeper loss of stiffness for another ~ 10,000 cycles before the development of the second crush zone. Before catastrophic failure, the stiffness decreased very acutely for another ~ 1000 cycles. The specimen displayed a shallow monotonic decrease of stiffness at a relatively constant rate for ~70% of its life until the onset of delamination. Two regimes are highlighted in Figure 6-16, namely, before and after crush zone development, as blue and red, respectively.

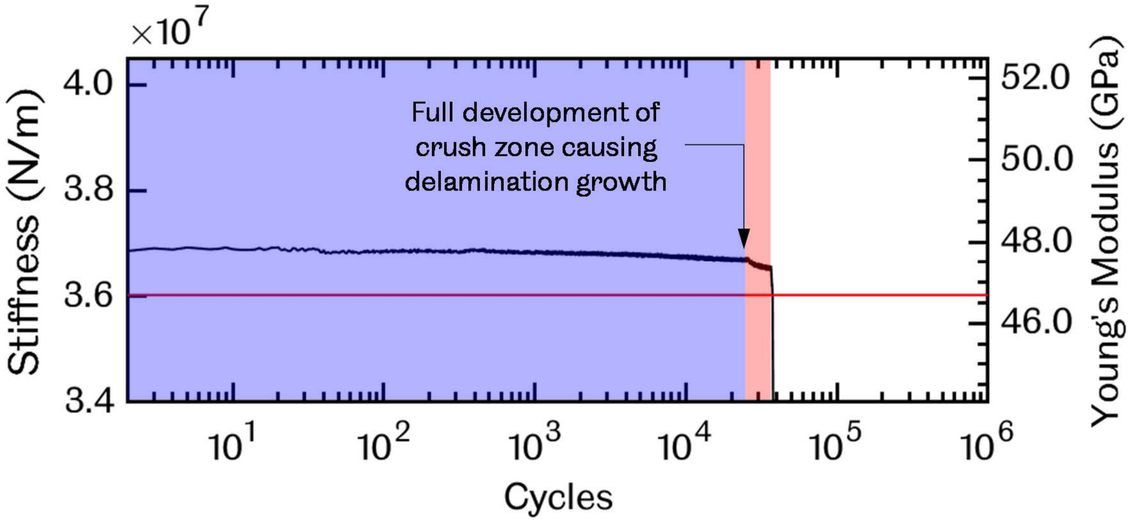

Figure 6-16. Example of a typical stiffness history from the OHC fatigue tests. The two distinct events observed in all tests are a decrease of tangent stiffness for most of the specimen life and the start of a more acute reduction in stiffness before failure. The regimes before and after the onset of delamination are highlighted in blue and red, respectively. The horizontal line indicates the average stiffness obtained from static testing.

As a way of comparing both techniques (TSA and DIC), maps of the change in the sum of strains from the first capture of the specimens reported in this and the previous section, are shown in Figure 6-17. The $\Delta T/T$ map corresponds to the S1 capture, i.e. at ~211 cycles. The $\Delta(\epsilon_x + \epsilon_y)$ map from DIC was obtained by subtracting correlated datasets from the first pair of turning points in the recovered deformation cycles. Note that the subtraction was made so that the colormap for areas of highest compressive strain corresponded to TSA, namely peak minus trough. Since each recovered deformation cycle is equivalent to 25 loading cycles, the map shown in Figure 6-17b corresponds to the span of the first 12.5 cycles.

It was found that splits in the surface ply appear as early as 12.5 cycles, as shown in Figure 6-17b. Splitting can also be observed at the corresponding locations in the $\Delta T/T$ map in (b). From these observations, it can be surmised that splitting in the angle plies at the vicinity of the notch contribute to the early reduction in stiffness by alleviating stress concentration. This, in turn, suggests that initial damage is controlled by the shear fracture toughness of the matrix. It is important to note that both methods were able to capture the acute strain gradients caused by the splits but damage resolution from the DIC capture is limited by the correlation parameters that determine the strain resolution of the correlated datasets, i.e. step size and strain window size. In contrast, the ability of TSA to resolve damage is dependent mostly on magnification and, thus, by balancing capture integration time with the exposure setting of the camera, damage can almost always be resolved more clearly with TSA than DIC.

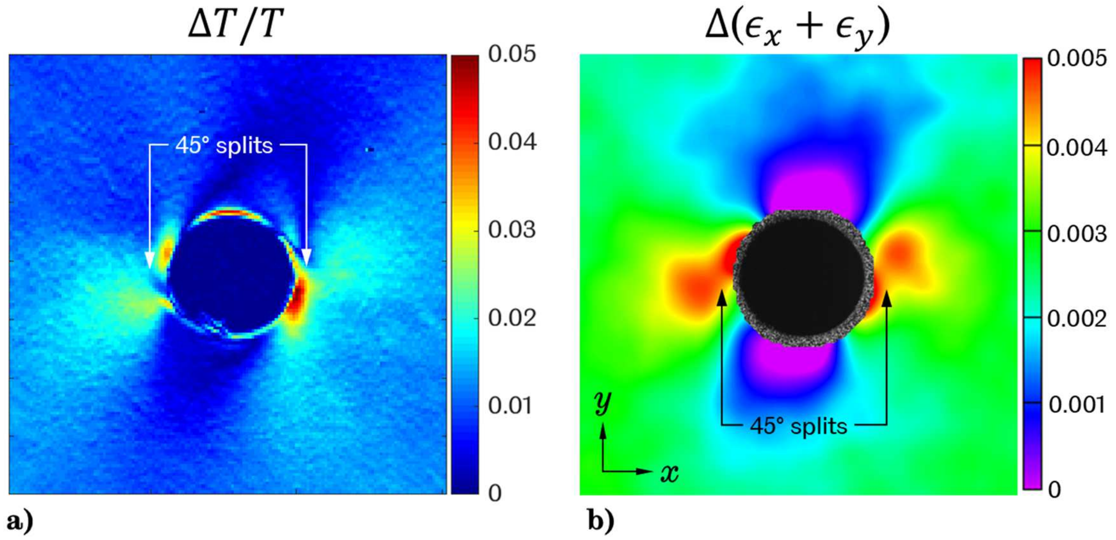

Figure 6-17. Maps of strain change from specimens captured separately with TSA (a) and DIC (b) at the beginning of compressive fatigue testing, i.e. ~211 cycles for TSA and ~12.5 cycles for DIC. Splits in the 45° surface ply can be observed as early as 12.5 cycles from the DIC map.

Nonetheless, the application of DIC to capture the fatigue tests offers capabilities not possible with TSA. An example is the tracking of hysteresis loops at prescribed locations, as shown in Figure 6-18, where (a) and (b) are plots of longitudinal strain for the whole capture train (as defined in Section

6.5.3) and (c) and (d) are plots of load vs. longitudinal strain for each capture. Moreover, leveraging from findings of the TSA captures, the values of longitudinal strain were interrogated at the locations where crush zones were expected to develop at the left and right sides of the hole; (a) and (c) plots correspond to the left side, and (b) and (d) to the right side. The colour code corresponds to the regimes highlighted in Figure 6-16 with the last capture block shown in black for visibility. In the strain vs life plots, each column of data is a capture block, i.e. spanning 62.5 loading cycles.

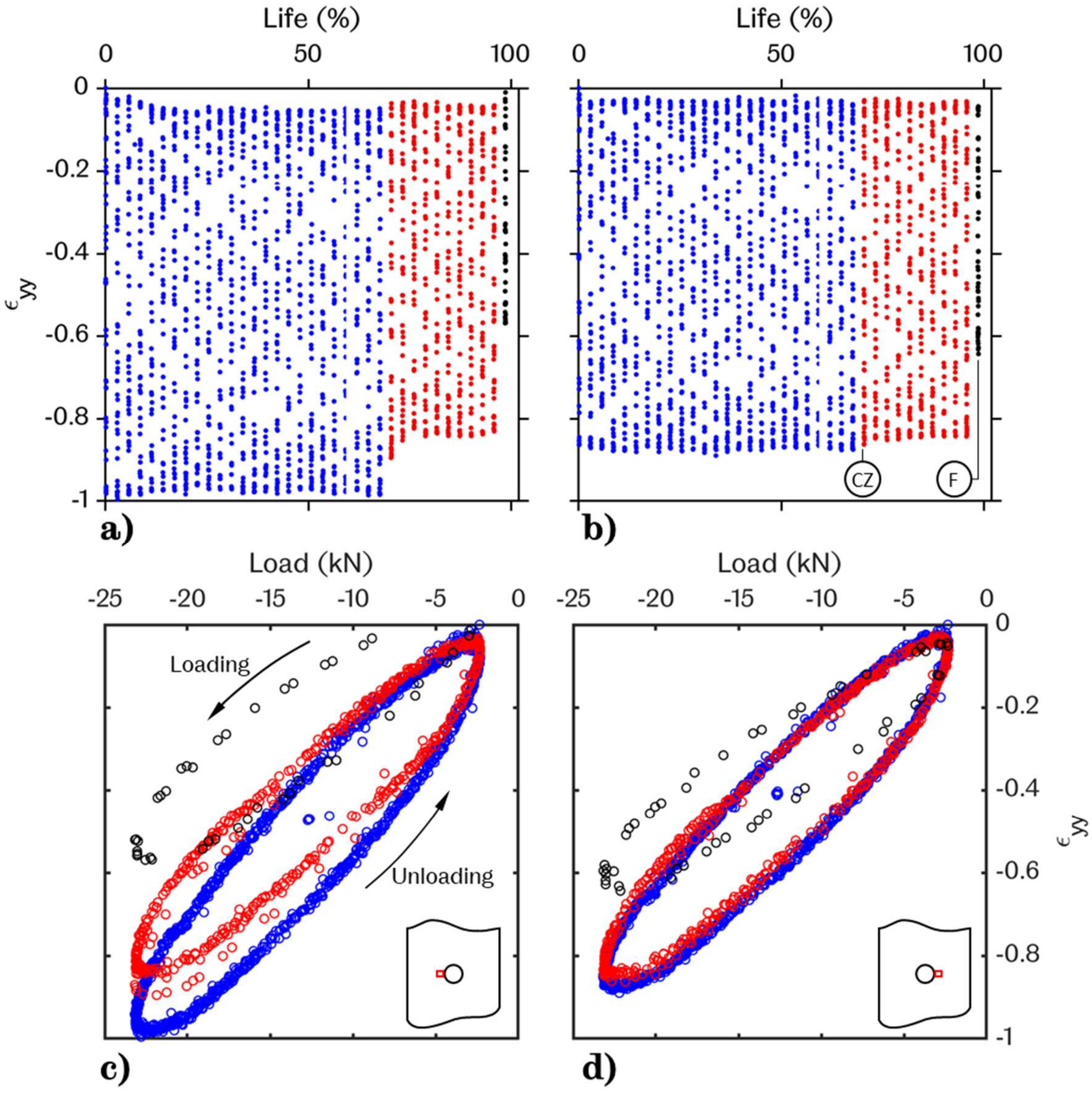

Figure 6-18. Plots of longitudinal strain ϵ_{yy} vs life percentage (a, b) and ϵ_{yy} vs. load (c, d) from DIC. The values of ϵ_{yy} were taken from the locations of expected development of crush zones with (a, c) and (b, d) corresponding to the left and right side of the hole, respectively.

From the strain vs life plots, it can be seen that the first crush zone develops at the left side around 27,000 cycles or ~82% of the specimen life, showing as an apparent drop in the minimum strain. The right side did not show a significant change in strain level until the last capture block. Both sides exhibited a significant strain drop during the last capture block i.e. imminent failure, which is indicative of large scale delamination in agreement with observations from TSA.

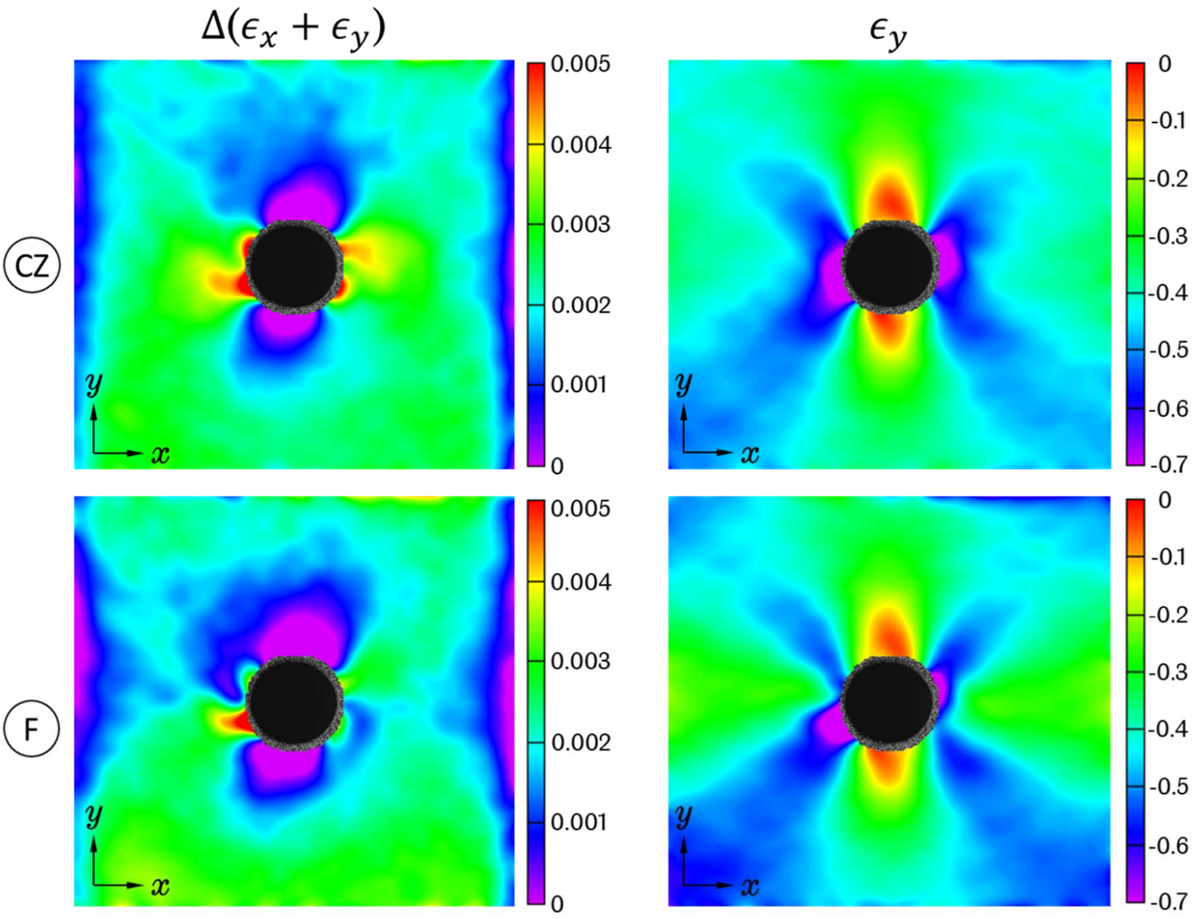

Figure 6-19. Maps of the change in the strain sum $\Delta(\epsilon_x + \epsilon_y)$ and longitudinal strain ϵ_y from DIC at the onset of delamination and imminent failure, labeled as "CZ" and "F" in Figure 6-18b.

From the hysteresis plots (Figures 6-18c and d), it can be seen that the material response is viscoelastic and that the same differences between the damage regimes can be observed. Namely, that at the onset of delamination the local strain at the sides of the notch displays a sudden decrease. It is also notable that energy dissipation decreases after each decrease of the strain level, as indicated by the relatively smaller loop areas, further supporting the thesis that delamination had taken place.

Figure 6-19 shows maps of $\Delta(\epsilon_x + \epsilon_y)$ and ϵ_y at the onset of delamination and at the last half-cycle of the last capture block extracted from the DIC capture, in order to compare damage evolution with the TSA data. The strain distributions were found to be consistent with the TSA maps, in particular that the development of crush zones as revealed by a significant drop in local stiffness gives was to large scale delamination. Delamination grows perpendicular to the loading direction until it reaches the edges of the specimen, at which point failure by gross buckling ensues, as shown in Figure 6-20.

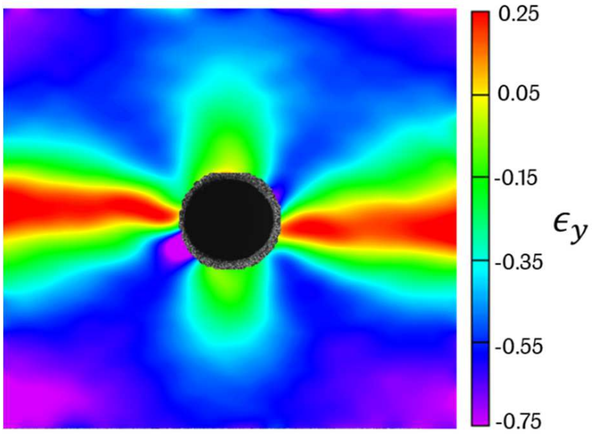

Figure 6-20. Longitudinal strain map from the last captured DIC dataset. It can be inferred from the bands of tensile strain that large scale delamination had taked place throughout the width of the specimen.

Note that the sequence of damage events during OHC fatigue is the same as from static testing. This is with the exception of splitting for which no evidence was found in the static datasets. However, this last item is not conclusive, as the gradients resulting from splitting could have been obscured by insufficient strain resolution.

6.6.3 Stiffness history from analogue acquisition

The full field datasets had, necessarily, to be compared with analogue data acquisition in order to locate damage events in the specimen life. But also, the capacity of the analogue instruments to indicate or resolve these damage events had to be gauged. This is because the simplest form to measure a fatigue test is with analogue instruments, e.g. an LDVT or extensometer. So, by relating the changes observed in the analogue displacement signal acquired from the OHC fatigue campaign with the corresponding events observed in TSA or DIC, a set of heuristic guidelines for life assessment can be derived.

Figures 6-21 to 6-23 comprise examples of analogue acquisition histories for 4 specimens, 2 from each material system tested in fatigue. In each Figure one “short” and one “long” life specimen is shown from each system. In order to locate damage events the displacement analogue signature of each test was formatted in three distinct forms:

1. Semi-log plots of stiffness and modulus vs cycles were produced for each test, as shown in Figure 6-21. This format helps to observe the early changes in laminate stiffness. The horizontal red lines indicate the average stiffness of the material system as measured from static testing (see Section 5.3).
2. Plots of normalized stiffness vs life percentage, as shown in Figure 6-22. This format helps to visualize the shape of the stiffness history irrespective of the cycles to failure. In these plots stiffness is normalized against the first load half-cycle.
3. Plots of the change in the positions of the signal turning points, i.e. peak and trough, as shown in Figure 6-23. These plots help to understand the physical changes that the specimen undergoes during OHC fatigue, which in turn manifest as a change in its bulk stiffness.

Note that the specimen in Figure 6-21a is the one in Section 6.6.1. By inspection of the set of plots, several common features can be observed as follows:

- A shallow monotonic decrease of stiffness precludes the faster degradation of the laminate after the development of the first crush zone. Of these two regimes, the former suggests a more diffuse subcritical damage process i.e. matrix cracking, while the latter is indicative of large scale delamination.

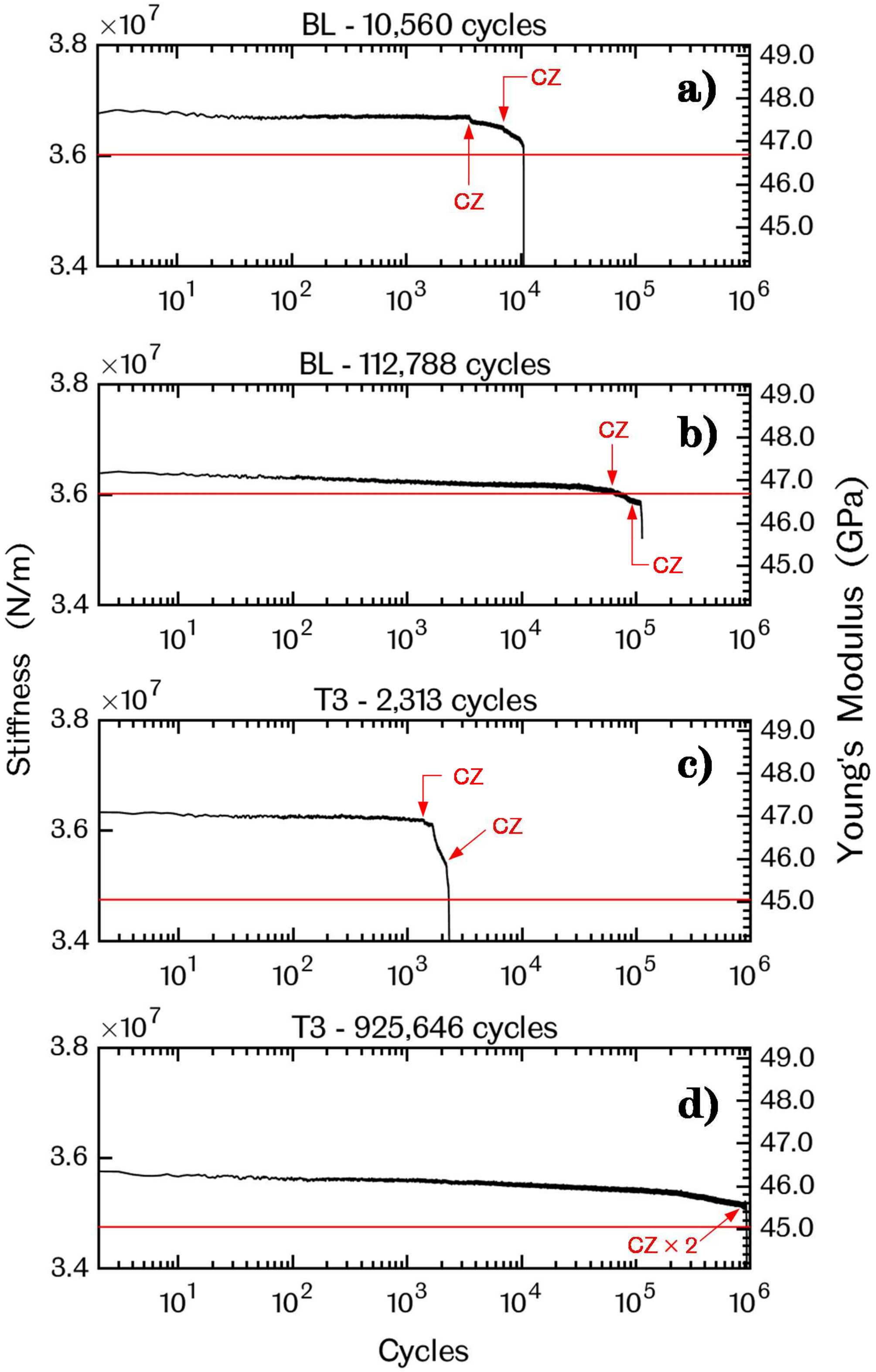

Figure 6-21. Plots of stiffness and modulus vs cycles for short and long life specimens of the BL (a ,b) and T3 (c, d) systems. Stiffness was normalized against the first half-cycle. Damage events are indicated as MC for matrix cracking and CZ for crush zone development.

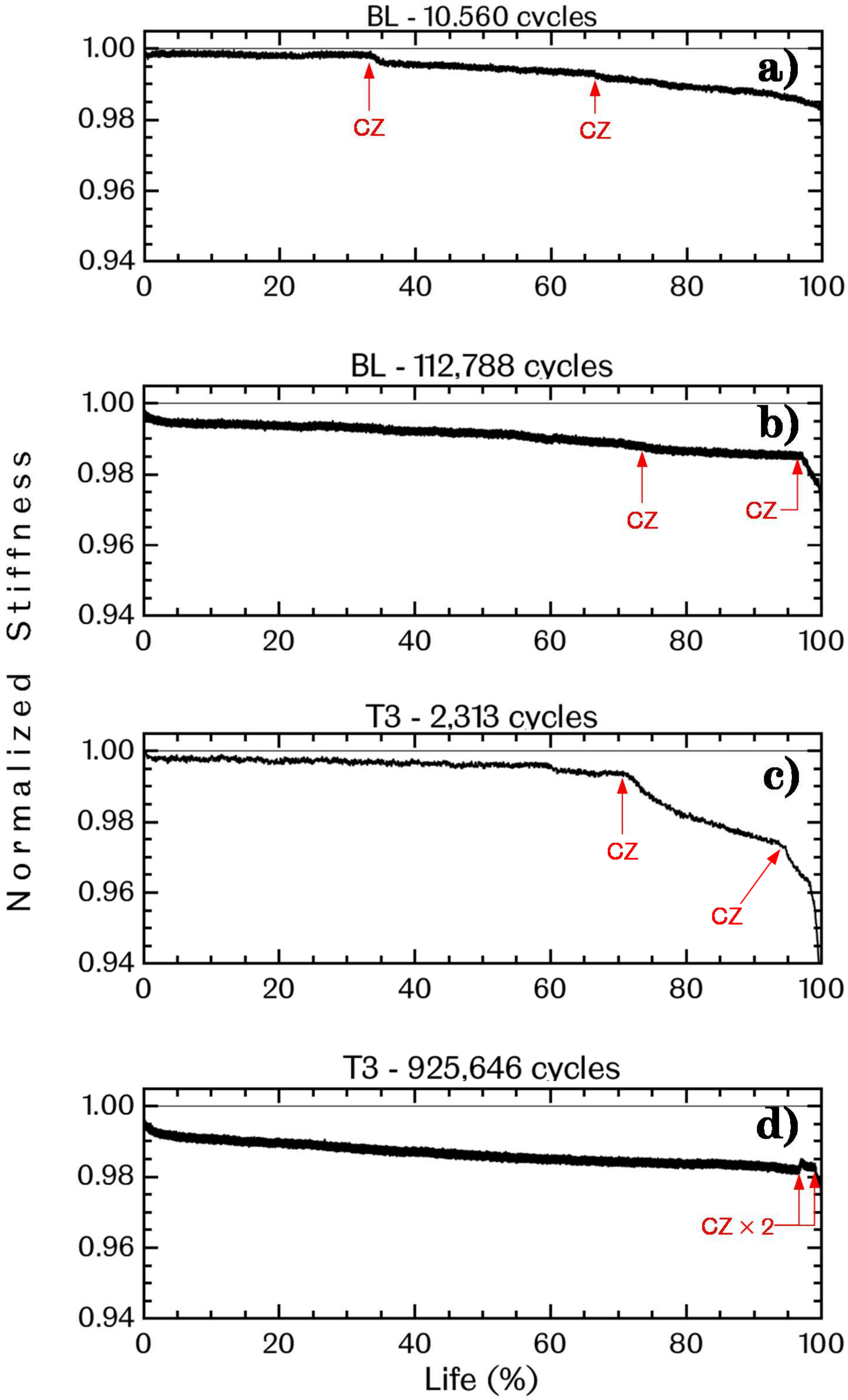

Figure 6-22. Plots of normalized stiffness vs life percentage for short and long life specimens of the BL (a ,b) and T3 (c, d) systems. Stiffness was normalized against the first half-cycle. Damage events are indicated as MC for matrix cracking and CZ for crush zone development.

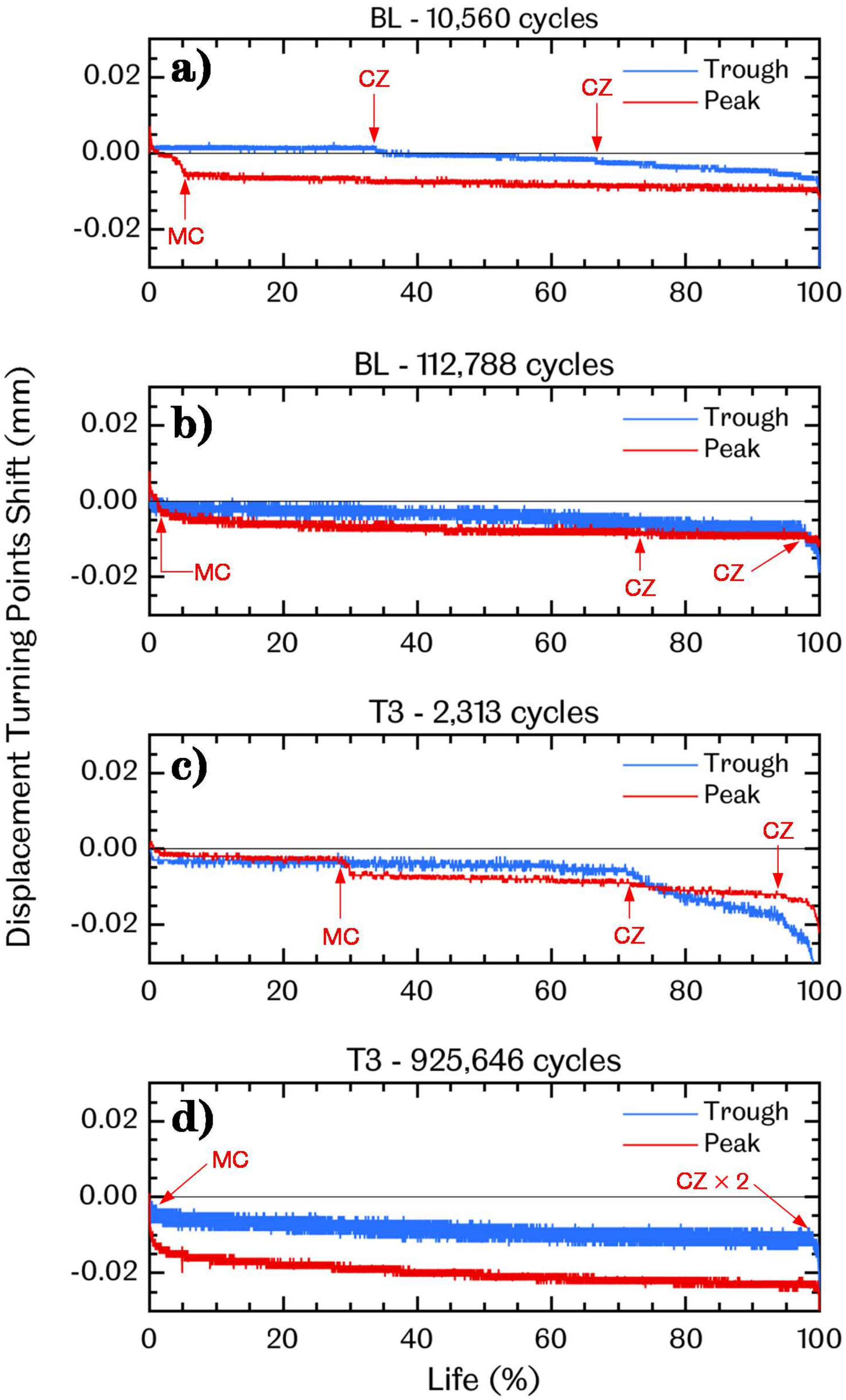

Figure 6-23. Plots of change in the peak and trough positions of the loading cycles for short and long life specimens of the BL (a ,b) and T3 (c, d) systems. Damage events are indicated as MC for matrix cracking and CZ for crush zone development.

- From the plots of turning point positions (Figure 6-23), it was found that all specimens showed an acute shift within the first 10^3 cycles or so. Both positions (peak and trough) display this change but typically more markedly for the peak i.e. the minimum load level. This corresponded to the appearance of splits in the 45° surface ply which are believed to blunt the stress concentration and delay the development of kink bands.
- At the onset of delamination, the trough displacement position starts to drop which, consequently, manifests as decreasing stiffness until failure. The duration of this decrease seems to be a function of cycles rather than life percentage. Catastrophic failure appears to be controlled by the development of the 2nd crush zone which increases the rate of delamination and, by the same measure, reducing the laminate strength.

Based on these common observations, relatively good confidence in the location of subcritical damage and the decline in stiffness before failure can be obtained, by use of analogue data alone. To reduce the uncertainty of such locating, noise needs to be minimized in comparison with the magnitude of the signal changes pertaining to stiffness change. An alternative solution to better precision in the displacement transducer is a robust filtering scheme of the analogue acquisition to bring out relevant information only. For the measurements in this work, noise equivalent to a maximum of ~5 μm did not preclude the observation of stiffness changes.

It was observed that in some specimens the trough displacement position shifted by a positive amount significantly, which could be interpreted as the laminate stiffening as per Equation 17. However, upon inspection of the full-field datasets it was found that this resulted from asymmetric non-parallel motion of the fixture's top platen and the probing location of the 3 mm LVDT, at the side of the specimens. Since the LVDT could not measure the displacement closer to the specimen's midline, deformation of the specimen side opposite to where the LVDT was mounted caused the top platen to tilt due to tolerances in the linear bearing assembly. The platen lopsided motion incorrectly manifested as an extensional change of the specimen.

Lastly, it is again noted that analogue data acquisition for the whole fatigue test campaign can be found in Appendices C and D, for the BL and T3 system, respectively.

6.6.4 Effect of interleaving on the fatigue performance

Statistical survival analysis was performed on the life data, in order to evaluate the effect of interleaving in the OHC fatigue performance of the subject material systems, which was one of the high level objectives of the current work. Also, an alternative method to predict the OHC fatigue life within confidence bounds was explored by fitting two-parameter Weibull distributions to the life data.

The use of a so-called hazard function to calculate survival probability is very common in the analysis of life data, where a certain number of items are considered at risk of failure at the beginning of a certain time period [148]. A common method to calculate this probability is by using the Kaplan-Meier non-parametric method to obtain empirical cumulative distribution function for the probability of survival [149]. The method is adept to the study of fatigue life whereby the hazard or failure rate as a function of loading cycles can be calculated as

$$h(N) = \frac{d_N}{r_N} \tag{19}$$

where d_N and r_N are the number of specimens that have failed and or still survive after N cycles. Then, the survival probability can be obtained as

$$S(N) = S_{N-1}\big(1 - h(N)\big) \tag{20}$$

where $S(0) = 1$. The Kaplan-Meier estimator for the survivor function is also known as the product-limit estimator and provides a conservative measure of survival probability. This is because the probability is modelled as a discrete step function, which is an overestimate of the cumulative hazard function.

Thus, survival probability plots with 95% confidence bounds were constructed using Matlab `ecdf` function on the life data of the two material systems, as shown in Figure 6-24. It can be seen that, although there is an apparent difference in the mean survival probability curves, it cannot be concluded that interleaving improved the fatigue life within 95% of confidence.

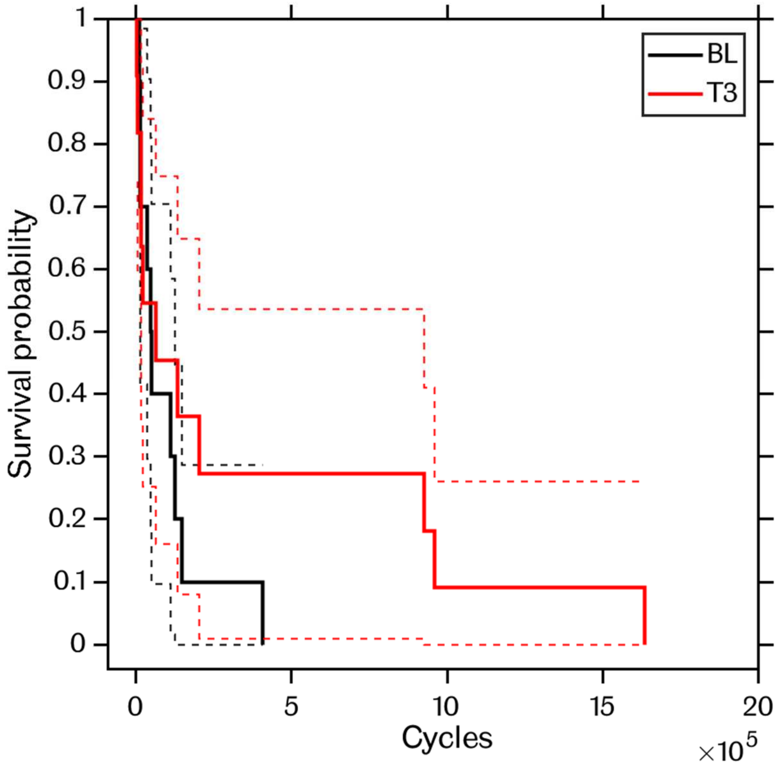

Figure 6-24. Survival probability plot of the life data using the Kaplan-Meier method. The 95% confidence bounds are shown with dotted lines.

An alternative method to model probability of failure is to fit a two-parameter Weibull distribution to the life data [150]. The Weibull distribution is used extensively for reliability and lifetime modelling. A very relevant example of its use can be found in reference [151], which is a technical report on fatigue life assessment of composite aircraft structures from the Federal Aviation Administration of the U.S. Department of Transportation.

A two parameter Weibull cumulative distribution function to calculate the probability of failure as a function of cycles can be defined as [150]

$$f(N|a,b) = ba^{-b}N^{b-1}e^{-\left(\frac{N}{a}\right)^{b}}I_{(0,\infty)}(N) \tag{21}$$

where a is known as the scale parameter and b as the shape parameter, and $I_{(0,\infty)}(N)$ indicates that the function can only take positive values.

Thus, curves of cumulative probability of failure with 95% confidence bounds were constructed by fitting the life data of each system using the Matlab commands `wblfit` and `wblcdf`, as shown in Figure 6-25. The fitted parameters (a, b) were (93 257, 0.9267) and (200 098, 0.5255) for BL and T3, respectively. Also, the mean and variance were, respectively, 96 618.6 and 1.088e10 from the BL fit and 366 644 and 5.862e11 from the T3 fit.

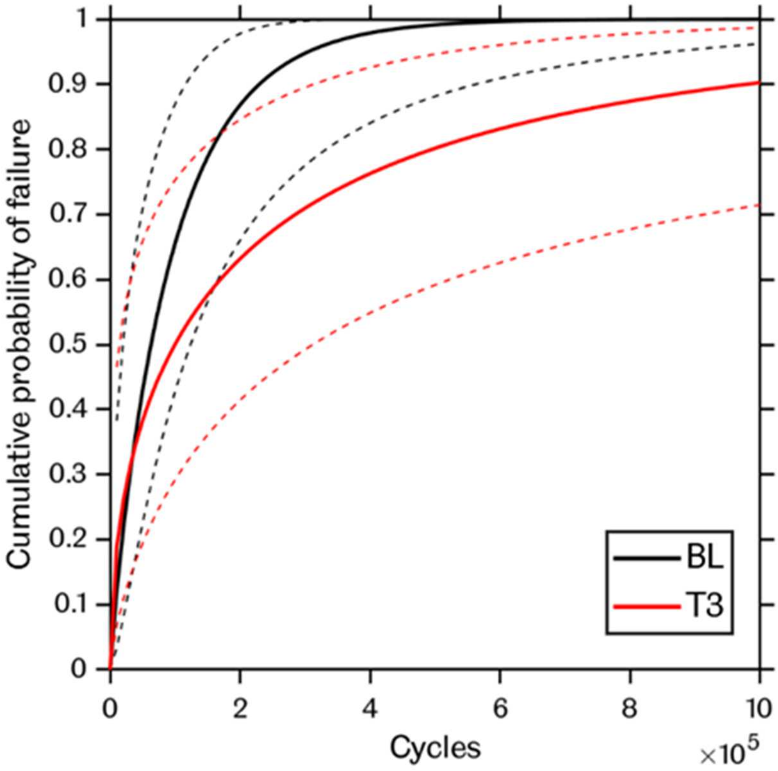

Figure 6-25. Two-parameter Weibull distributions fitted to the fatigue life data of each system. The 95% confidence bounds are shown with dotted lines.

Again, it could not be concluded, within 95% of confidence, that interleaving as in the T3 system improves the OHC fatigue life of the laminates. Even though the mean of the T3 system was predicted as ~3.8 as many cycles as for the BL system, the variance was one order of magnitude larger. As such, additional observations (tests) are needed to decrease the spread of the life data and reveal potential differences in the performance of the material systems. Nonetheless, the fitted curves and confidence bounds were evaluated at intervals of 10^5 cycles to provide means of comparing the probability of failure for durations $\leq 10^6$ cycles, as shown in Table 6-2.

Table 6-2. Evaluation of BL and T3 fitted Weibull distributions and confidence bounds at 10^5 cycle intervals.

Cycles	$f(x)$		$\Delta f(x)$	Lower Bound			Upper Bound		
10^5	BL	T3		BL	T3	ΔLB	BL	T3	ΔUB
0	0	0	–	–	–	–	–	–	–
1	65.6%	50.1%	-15.5%	42.8%	29.2%	-13.6%	87.0%	75.3%	-11.7%
2	86.8%	63.2%	-23.6%	66.1%	41.4%	-24.7%	97.8%	84.6%	-13.2%
3	94.8%	71.0%	-23.8%	77.5%	49.3%	-28.3%	99.7%	89.5%	-10.2%
4	97.9%	76.3%	-21.6%	84.1%	54.9%	-29.2%	100.0%	92.6%	-7.4%
5	99.1%	80.2%	-19.0%	88.2%	59.2%	-29.0%	100.0%	94.6%	-5.4%
6	99.6%	83.1%	-16.5%	90.9%	62.6%	-28.3%	100.0%	96.0%	-4.0%
7	99.8%	85.5%	-14.3%	92.9%	65.4%	-27.5%	100.0%	97.0%	-3.0%
8	99.9%	87.4%	-12.5%	94.3%	67.7%	-26.6%	100.0%	97.7%	-2.3%
9	100.0%	89.0%	-11.0%	95.4%	69.7%	-25.6%	100.0%	98.3%	-1.7%
10	100.0%	90.3%	-9.7%	96.2%	71.5%	-24.7%	100.0%	98.7%	-1.3%

6.7 Summary

The validation of the testing parameters for TSA enabled the best possible capture of the OHC tests with the current equipment. It was found that the effect of paint coat thickness is not negligible, in agreement with published literature. However, since the application of a coat of paint is subjective and will, in practice, vary between users, a parametric study of the paint application is recommended in order to minimize attenuation of the TSA signal. The same reasoning applies to the selection of the testing frequency and magnification. The linear increase in signal noise with load rate, has to be considered when selecting the test frequency. In contrast, signal attenuation depends by a larger extent to the transmittance of the optics used rather than the magnification.

From the results described in this chapter, it was demonstrated that the application of DIC and TSA is effective in the damage assessment of notched laminates. Most notably, the different methods used to extract information from the full field datasets are able to locate the sudden changes that result from damage growth during OHC fatigue. This enabled the observation of a common sequence of damage events across all specimens. Namely, that after an early (~10^3 cycles) and sudden decrease, the stiffness of the specimens remains relatively constant until the onset of delamination, which marks the beginning of a steady decline in stiffness until catastrophic failure. The residual life of the specimen after the development of the first crush zone appears to be a function of cycles. Final failure appears to be controlled by the development of the 2nd crush zone after which the specimen underwent a very steep decline in residual strength.

Lastly, statistical analysis of life data demonstrated that it could not be concluded, within 95% of confidence, that interleaving as in the T3 system improves the OHC fatigue life of the laminates.

CHAPTER 7 CONCLUSIONS AND FUTURE WORK

The work presented in this thesis constitutes the first dedicated application of surface full-field experimental techniques to the damage assessment of open-hole compression in composite laminates, under both static and fatigue loading. The work was motivated by an existing gap in the published literature pertaining to the location of the occurrence of different damage events during the life of in-service composite structures. As such, the main goal of the work was to demonstrate the viability of using TSA and DIC to study the evolution of damage in CFRP laminates with an open-hole under compressive loading. A obvious benefit of this work is that by characterizing the sequence of damage events and their occurrence in OHC coupons, the design allowables of composite structures can be better approximated.

Thus, in relation to the high-level objectives set at the beginning of this thesis, the main conclusions are summarised below, followed by recommendations made for future work.

7.1 Fixture design for full-field testing

A compression test fixture that provides enough visual access for the use of TSA and DIC were designed and manufactured as part of this work. The design was rated for dynamic loading of composite laminates in accordance to ASTM and BS standards. Then, in using the fixture it was demonstrated that:

- The design allowed the application of compressive loads to un-notched specimens of up to 75% F_{ult} without significant buckling. This, in turn, allowed the calculation of realistic reference values of bulk stiffness and Poission’s ratio.
- The failure mode of OHC specimens was in line with ASTM standards, thus providing valid measurements of modulus, strength and ultimate strain.

7.2 Use of 3D–DIC for OHC static testing

The use of DIC for the static testing of notched laminates enabled the observation of the acute strain gradients that result from damage development at the vicinity of the notch and the damage mechanisms that lead to bulk failure of the laminate. The main findings from the OHC static tests were:

- The presence of the notch does not decrease the stiffness of the laminate significantly and is independent of the material system, i.e. that interleaving does not have an impact.
- The presence of the hole does reduce significantly the compressive strength of the laminate by up to 50%, which is in agreement with published literature.
- The mean reduction in failure strain due to the presence of the hole was ~25% and, again, interleaving did not appear to affect this property.
- Failure of OHC specimens starts with what is thought to be the collapse of kink bands in the 0° plies at the east and west edges of the hole, referred to here as crush zones. The development of these crush zones is brittle and marks the start of unstable damage growth in the form of large scale delamination. These delamination zones grow towards the edges of the specimen, perpendicular to the load axis before bulk failure by buckling.

7.3 Use of TSA for OHC fatigue testing

Next, the use of TSA to capture fatigue tests enabled the observation of a characteristic sequence of damage events and their associated morphology. Detailed validation studies were carried out to find the optimum experimental setup parameters and specimen preparation. It was demonstrated that:

- The paint coat thickness is critical in controlling the attenuation of the TSA signal, which is consistent with published literature. However, it is recommended that the paint application is characterized per operator to find the optimum number of coats. Here it was found that 1 coat of paint as defined in section 6.5.2 was the optimum thickness.

- The loading frequency also has a significant effect on the TSA signal magnitude and its standard deviation. It was found that, for the materials investigated, signal magnitude increased asymptotically with frequency and converged for the most part above 12.5 Hz. Also, the standard deviation was found to increase linearly with frequency.
- In the absence of motion compensation (digital or physical), a compromise can be made between spatial resolution and motion blur by using a magnification level whereby the physical pixel size is marginally larger than the largest expected motion in the FOV.
- Within the practical loading frequency range (< 30 Hz) interlaminar heat transfer is significant and will cause a finite difference of up to ~17% in the out-of-phase component within the 5 to 25 Hz range. This supported the case for using the total thermoelastic change rather that the in- and out-of-phase components in order to improve the observation of damage events.
- By optimizing the testing parameters it is possible to resolve thermoelastic changes down to the order of 1×10^{-3} °C. This allowed to locate and characterize the different damage events in the life of the specimens.

7.4 Use of 2D–DIC for OHC fatigue testing

By judiciously selecting the capture rate, it was possible to perform measurements on OHC fatigue tests using 2D–DIC with more conventional low frame rate cameras. A testing methodology based on subsampling of the loading signal was successfully used to recover oscillations of the correlation area in the DIC datasets. Provided that the illumination is enough for the magnification used and the level of motion in the deformation field, it was shown that adequate resolution can be achieved with this simplified methodology. It was demonstrated that:

- It is possible to observe and locate the distinct damage events involved in the fatigue testing of OHC coupons by recovering deformation pseudo-cycles at finite intervals during the life of the specimen.
- DIC enables the observation of crush zone development and the resulting stress redistribution. The identification of the different damage regimes was possible by interrogating the east and west edges of the hole. Sudden reductions in longitudinal strains (in line with loading) were observed when the crush zones developed.
- Plots of $\Delta(\epsilon_x + \epsilon_y)$ between the peak and trough positions match the $\Delta T/T$ maps from the TSA. This shows that subsurface kink band formation can also be inferred from the acute strain gradients observed with DIC.
- It is possible to measure the viscoelastic response of these materials by plotting load-strain hysteresis from the DIC datasets. This allows to observe the change in strain energy dissipation during the life of the specimen.

7.5 Damage assessment of OHC tests

The use of the different data reduction methods detailed in section 6-6 show that that there appears to be causality in the damage sequence of notched laminates when subjected to compressive loads, independent of load rate. Namely, that failure is controlled by the resistance to kink band formation in the 0° plies. Whilst this was known to be the case from published literature, the work in this thesis is the first to establish a relationship between the damage sequences in static tests to the one in fatigue. It was found that:

- Damage growth in notched laminates appears to be a critical process whereby the development of the crush zones causes unstable growth rate until failure. Therefore, the onset of delamination upon the collapse of a kink band divides the damage regimes based on its growth rate i.e. stable and unstable. This is important for the definition of design allowables for in-service structures.

- No noticeable subcritical damage was observed from static testing with 3D-DIC before the collapse of the first kink band. The absence of observable damage, however, is not conclusive because the ability to resolve damage is limited by the strain resolution of the correlation.
- The first observable damage type to appear during fatigue testing was matrix cracking in the form of splits at the 45° surface ply. These splits are responsible for an early stress redistribution at the areas of highest stress concentration at the vicinity of the notch, effectively blunting the stress gradients.
- This blunting of the stress concentration at the notch delays the development and collapse of the kink bands. Due to this, the load bearing capacity, i.e. the residual strength, of the laminate undergoes a shallow monotonic decrease until the formation of the first crush zone. This suggests that the laminate is still mostly structurally sound before the onset of delamination. Thus, by locating this event in the life of the specimens, more appropriate design allowables can be obtained.
- The collapse of the second kink band further increases the delamination growth thus accelerating catastrophic failure, which was found to occur within 10^3 cycles.
- The statistical analysis of life data demonstrated that it could not be concluded, within 95% of confidence, that interleaving as in the T3 system improves the OHC fatigue life of the laminates.

7.6 Recommendations for future work

The outcomes from the work contained in this thesis give way to further research in the application of DIC and TSA to study notched laminates. The areas of further work with relevance to this thesis are described below.

A first recommendation is the refinement of the specimen geometry with aim to reduce spurious variation in the results. Greater care should be exercised in the machining of the hole and loading surfaces. That is, to minimize the machining damage from the drilling operation and increase the flatness parallelism of the loading surfaces. Also, the possibility of characterizing drilling damage could help in elucidating a relationship between hole quality and the structural performance of the laminate. The recommendation to refine the machining of the loading surfaces is motivated by the need for even application of the load in order to approximate a uniaxial load configuration.

The second recommendation is to improve the acquisition of displacement analogue data that is machine compliance independent by positioning the transducer closer to the specimen midline. This change in combination with the first recommendation should decrease the spread in the results by a significant amount.

A third recommendation is the use of internal NDE techniques like microCT scanning or C-scanning to observe internal damage in specimens before failure. This could help to further elucidate the damage micro-mechanisms responsible for the surface changes observed here with TSA and DIC. It could also help to validate the use of the analogue displacement acquisition alone to obtain a measure of residual life.

The next recommendation is the automation of the TSA data processing and the extraction of the quantities of interest. In particular, it would be of interest to automate the location of the onset of delamination. It is the author’s opinion that the application of vision algorithms can help to process the large datasets that can result from fatigue tests much faster and more reliably.

Lastly, it is thought that a comprehensive understanding of the OHC fatigue performance cannot be achieved unless a sufficiently large amount of tests is performed for a particular load level. As a guideline, the ASTM D7615 standard requires 24 specimens for the construction of an S-N curve to be used for reliability and design allowables. This is also desirable based on the need to revisit the study of interleaving and its effects to establish if it yields any benefit.

REFERENCES

[1] C. Soutis, “Carbon fiber reinforced plastics in aircraft construction,” *Mater. Sci. Eng. A*, vol. 412, no. 1–2, pp. 171–176, 2005.

[2] M. O. W. Richardson and M. J. Wisheart, “Review of low-velocity impact properties of composite materials,” *Compos. Part A Appl. Sci. Manuf.*, vol. 27, no. 12, pp. 1123–1131, Jan. 1996.

[3] C. Soutis and P. T. Curtis, “Prediction of the post-impact compressive strength of cfrp laminated composites,” *Compos. Sci. Technol.*, vol. 56, no. 6, pp. 677–684, Jan. 1996.

[4] E. Guynn, W. Bradley, and W. Elber, “Micromechanics of Compression Failures in Open Hole Composite Laminates,” in *Composite Materials: Fatigue and Fracture, Second Volume*, 100 Barr Harbor Drive, PO Box C700, West Conshohocken, PA 19428-2959: ASTM International, 1989, pp. 118-118–19.

[5] N. A. Fleck, “Compressive Failure of Fiber Composites,” *Adv. Appl. Mech.*, vol. 33, pp. 43–117, Jan. 1997.

[6] J. R. Fried, *Polymer Science and Technology*, 3rd ed. Pearson Education, 2014.

[7] B. J. Derkowski and H. J. Sue, “Morphology and Compression-After-Impact Strength Relationship in Interleaved Toughened Composites,” *Polym. Compos.*, vol. 24, no. 1, pp. 158–170, 2003.

[8] F. Salmon Guzman, M. Jackson, S. Jones, and R. A. Tomlinson, “Use of digital image correlation to measure strain recovery in particle toughened thermoset resins,” *Strain*, vol. 54, no. 2, p. e12261, Apr. 2018.

[9] D. J. Bull, S. M. Spearing, and I. Sinclair, “Investigation of the response to low velocity impact and quasi-static indentation loading of particle-toughened carbon-fibre composite materials,” *Compos. Part A Appl. Sci. Manuf.*, vol. 74, pp. 38–46, Jul. 2015.

[10] D. J. Bull, S. M. Spearing, I. Sinclair, and L. Helfen, “Three-dimensional

assessment of low velocity impact damage in particle toughened composite laminates using micro-focus X-ray computed tomography and synchrotron radiation laminography," *Compos. Part A Appl. Sci. Manuf.*, vol. 52, pp. 62–69, Sep. 2013.

[11] D. J. Bull, A. E. Scott, S. M. Spearing, and I. Sinclair, "The influence of toughening-particles in CFRPs on low velocity impact damage resistance performance," *Compos. Part A Appl. Sci. Manuf.*, vol. 58, pp. 47–55, Mar. 2014.

[12] D. J. Bull, S. M. Spearing, and I. Sinclair, "Observations of damage development from compression-after-impact experiments using ex situ micro-focus computed tomography," *Compos. Sci. Technol.*, vol. 97, pp. 106–114, Jun. 2014.

[13] G. Borstnar, M. N. Mavrogordato, L. Helfen, I. Sinclair, and S. M. Spearing, "Interlaminar fracture micro-mechanisms in toughened carbon fibre reinforced plastics investigated via synchrotron radiation computed tomography and laminography," *Compos. Part A Appl. Sci. Manuf.*, vol. 71, pp. 176–183, Apr. 2015.

[14] G. Borstnar, F. Gillard, M. N. Mavrogordato, I. Sinclair, and S. M. Spearing, "Three-dimensional deformation mapping of Mode I interlaminar crack extension in particle-toughened interlayers," *Acta Mater.*, vol. 103, pp. 63–70, Jan. 2016.

[15] M. A. Sutton, H. W. Schreier, and J.-J. Orteu, *Image correlation for shape, motion and deformation measurements: basic concepts, theory and applications*. Springer, 2009.

[16] R. J. Greene, E. A. Patterson, and R. E. Rowlands, "Thermoelastic Stress Analysis," in *Springer Handbook of Experimental Solid Mechanics*, Boston, MA: Springer US, 2008, pp. 743–768.

[17] D. Hull and T. W. Clyne, *An introduction to composite materials*. Cambridge University Press, 1996.

[18] K. K. Chawla, *Composite materials : science and engineering*. Springer, 2012.

[19] O. Daniel, Isaac M and Ishai, *Engineering Mechanics of Composite Materials*. Oxford University Press, 2006.

[20] R. M. Jones, *Mechanics of composite materials*, 2nd ed. Taylor & Francis, 2014.

[21] A. Kaw, *Mechanics of Composite Materials*. CRC Press, 2006.

[22] C. Soutis, P. T. Curtis, and N. A. Fleck, "Compressive Failure of Notched Carbon Fibre Composites," *Proc. R. Soc. A Math. Phys. Eng. Sci.*, vol. 440, no. 1909, pp. 241–256, Feb. 1993.

[23] S. Kyriakides, R. Arseculeratne, and E. J. Perry, "On the compressive failure of fiber reinforced composites," *Int. J. Solids Struct.*, vol. 32, no. 6–7, pp. 689–738, Mar. 1995.

[24] T. J. Vogler and S. Kyriakides, "On the initiation and growth of kink bands in fiber composites: Part I. experiments," *Int. J. Solids Struct.*, vol. 38, no. 15, pp. 2639–2651, Apr. 2001.

[25] P. M. Moran, X. H. Liu, and C. F. Shih, "Kink band formation and band broadening in fiber composites under compressive loading," *Acta Metall. Mater.*, vol. 43, no. 8, pp. 2943–2958, Aug. 1995.

[26] B. W. Rosen, "Mechanics of Composite Strengthening," in *Fiber Composite Materials*, Metals Park, OH: American Society of Metals, 1965, pp. 37–75.

[27] C. Soutis, "Compressive Strength of Unidirectional Composites: Measurement and Prediction," in *Composite Materials: Testing and Design, Thirteenth Volume*, 100 Barr Harbor Drive, PO Box C700, West Conshohocken, PA 19428-2959: ASTM International, pp. 168-168–9.

[28] J. R. Lager and R. R. June, "Compressive Strength of Boron-Epoxy Composites," *J. Compos. Mater.*, vol. 3, no. 1, pp. 48–56, Jan. 1969.

[29] P. Ewins, "Tensile and compressive test specimens for unidirectional

carbon fibre reinforced plastics," *RAE Tech. Rep.*, vol. 71217, p. 342, 1971.

[30] A. Argon, "Fracture of composites," in *Treatise on materials science and technology*, 2013, pp. 79–114.

[31] R. Batdorf, SB and Ko, "Stress-strain behaviour and failure of uniaxial composites in combined compression and shear, Parts I and II," *Intern. report, Sch. Eng. Appl. Sci. Univ. California, Los Angeles, CA*, 1987.

[32] B. Budiansky and N. A. Fleck, "Compressive failure of fibre composites," *J. Mech. Phys. Solids*, 1993.

[33] C. R. Schultheisz and A. M. Waas, "Compressive failure of composites, part I: Testing and micromechanical theories," *Prog. Aerosp. Sci.*, vol. 32, no. 1, pp. 1–42, Jan. 1996.

[34] S. T. Pinho, C. G. Dávila, P. P. Camanho, L. Iannucci, and P. Robinson, "Failure Models and Criteria for FRP Under In-Plane or Three-Dimensional Stress States Including Shear Non-Linearity," 2005.

[35] R. Gutkin, S. T. Pinho, P. Robinson, and P. T. Curtis, "On the transition from shear-driven fibre compressive failure to fibre kinking in notched CFRP laminates under longitudinal compression," *Compos. Sci. Technol.*, vol. 70, no. 8, pp. 1223–1231, Aug. 2010.

[36] A. Puck and H. Schürmann, "FAILURE ANALYSIS OF FRP LAMINATES BY MEANS OF PHYSICALLY BASED PHENOMENOLOGICAL MODELS," *Compos. Sci. Technol.*, vol. 58, no. 7, pp. 1045–1067, Jul. 1998.

[37] A. Puck and H. Schürmann, "Failure analysis of FRP laminates by means of physically based phenomenological models," *Compos. Sci. Technol.*, vol. 62, no. 12–13, pp. 1633–1662, Sep. 2002.

[38] P. Berbinau, C. Soutis, P. Goutas, and P. T. Curtis, "Effect of off-axis ply orientation on 0°-fibre microbuckling," *Compos. Part A Appl. Sci. Manuf.*, vol. 30, no. 10, pp. 1197–1207, Oct. 1999.

[39] E. G. Guynn and W. L. Bradley, "A Detailed Investigation of the Micromechanisms of Compressive Failure in Open Hole Composite

Laminates," *J. Compos. Mater.*, vol. 23, no. 5, pp. 479–504, May 1989.

[40] E. G. Guynn and W. L. Bradley, "Measurements of the Stress Supported by the Crush Zone in Open Hole Composite Laminates Loaded in Compression," *J. Reinf. Plast. Compos.*, vol. 8, no. 2, pp. 133–149, Mar. 1989.

[41] L. B. Lessard and F.-K. Chang, "Damage Tolerance of Laminated Composites Containing an Open Hole and Subjected to Compressive Loadings: Part II—Experiment," *J. Compos. Mater.*, vol. 25, no. 1, pp. 44–64, Jan. 1991.

[42] C. Soutis, "Damage tolerance of open-hole CFRP laminates loaded in compression," *Compos. Eng.*, vol. 4, no. 3, pp. 317–327, Jan. 1994.

[43] C. Soutis, N. A. Fleck, and P. A. Smith, "Failure Prediction Technique for Compression Loaded Carbon Fibre-Epoxy Laminate with Open Holes," *J. Compos. Mater.*, vol. 25, no. 11, pp. 1476–1498, Nov. 1991.

[44] and P. A. S. Soutis, C., N. A. Fleck, "Compression fatigue behaviour of notched carbon fibre-epoxy laminates.," *Int. J. Fatigue*, vol. 13, no. 4, pp. 303–312, 1991.

[45] W. S. Slaughter and N. A. Fleck, "Compressive fatigue of fibre composites," *J. Mech. Phys. Solids*, vol. 41, no. 8, pp. 1265–1284, 1993.

[46] W. S. Slaughter and N. A. Fleck, "Viscoelastic Microbuckling of Fiber Composites," *J. Appl. Mech.*, vol. 60, no. 4, p. 802, Dec. 1993.

[47] W. S. Slaughter, J. Fan, and N. A. Fleck, "Dynamic compressive failure of fiber composites," *J. Mech. Phys. Solids*, vol. 44, no. 11, pp. 1867–1890, Nov. 1996.

[48] J. Fan and W. S. Slaughter, "High strain rate compression of fiber composites," *J. Mech. Phys. Solids*, vol. 45, no. 5, pp. 731–751, May 1997.

[49] Z. Mróz, "On the description of anisotropic workhardening," *J. Mech. Phys. Solids*, vol. 15, no. 3, pp. 163–175, May 1967.

[50] S. (Subra) Suresh, *Fatigue of materials*. Cambridge University Press,

1998.

[51] W. Ramberg and W. R. Osgood, “Description of stress-strain curves by three parameters,” Jul. 1943.

[52] M. . Hinton, A. . Kaddour, and P. . Soden, “A comparison of the predictive capabilities of current failure theories for composite laminates, judged against experimental evidence,” *Compos. Sci. Technol.*, vol. 62, no. 12–13, pp. 1725–1797, Sep. 2002.

[53] J. Degrieck and W. Van Paepegem, “Fatigue damage modeling of fibre-reinforced composite materials: Review,” *Appl. Mech. Rev.*, vol. 54, no. 4, p. 279, 2001.

[54] L. Reis and M. de Freitas, “Damage growth analysis of low velocity impacted composite panels,” *Compos. Struct.*, vol. 38, no. 1–4, pp. 509–515, May 1997.

[55] S. Abrate, *Impact on composite structures*. Cambridge University Press, 2005.

[56] M. de Freitas and L. Reis, “Failure mechanisms on composite specimens subjected to compression after impact,” *Compos. Struct.*, vol. 42, no. 4, pp. 365–373, Aug. 1998.

[57] J. C. Prichard and P. J. Hogg, “The role of impact damage in post-impact compression testing,” *Composites*, vol. 21, no. 6, pp. 503–511, Nov. 1990.

[58] R. Thomas *et al.*, “Miscibility, morphology, thermal, and mechanical properties of a DGEBA based epoxy resin toughened with a liquid rubber,” *Polymer (Guildf).*, vol. 49, no. 1, pp. 278–294, Jan. 2008.

[59] A. F. Yee, R. A. Pearson, A. F. Yee, R. A. Pearson, and A. F. Yee, “Toughening mechanisms in elastomer-modified epoxies,” *J. Mater. Sci.*, vol. 21, no. 7, Jul. 1986.

[60] R. Thomas *et al.*, “Cure kinetics, morphology and miscibility of modified DGEBA-based epoxy resin – Effects of a liquid rubber inclusion,” *Polymer (Guildf).*, vol. 48, no. 6, pp. 1695–1710, Mar. 2007.

[61] N. Chikhi, S. Fellahi, and M. Bakar, “Modification of epoxy resin using reactive liquid (ATBN) rubber,” *Eur. Polym. J.*, vol. 38, no. 2, pp. 251–264, Feb. 2002.

[62] C. Carfagna, L. Nicolais, E. Amendola, C. Carfagna, and A. G. Filippov, “Toughening epoxy resins by liquid crystalline polymers,” *J. Appl. Polym. Sci.*, vol. 44, no. 8, pp. 1465–1471, Mar. 1992.

[63] B.-L. Zhang, G.-L. Tang, K.-Y. Shi, Y.-C. You, Z.-J. Du, and J.-F. Huang, “A study on the properties of epoxy resin toughened by a liquid crystal-type oligomer,” *J. Appl. Polym. Sci.*, vol. 71, no. 1, pp. 177–184, Jan. 1999.

[64] P. Rosso, L. Ye, K. Friedrich, and S. Sprenger, “A toughened epoxy resin by silica nanoparticle reinforcement,” *J. Appl. Polym. Sci.*, vol. 100, no. 3, pp. 1849–1855, May 2006.

[65] B. B. Johnsen, A. J. Kinloch, R. D. Mohammed, A. C. Taylor, and S. Sprenger, “Toughening mechanisms of nanoparticle-modified epoxy polymers,” *Polymer (Guildf).*, vol. 48, no. 2, pp. 530–541, Jan. 2007.

[66] T. H. Hsieh, A. J. Kinloch, K. Masania, A. C. Taylor, and S. Sprenger, “The mechanisms and mechanics of the toughening of epoxy polymers modified with silica nanoparticles,” *Polymer (Guildf).*, vol. 51, no. 26, pp. 6284–6294, Dec. 2010.

[67] B. Wetzel, P. Rosso, F. Haupert, and K. Friedrich, “Epoxy nanocomposites – fracture and toughening mechanisms,” *Eng. Fract. Mech.*, vol. 73, no. 16, pp. 2375–2398, Nov. 2006.

[68] J. Spanoudakis and R. J. Young, “Crack propagation in a glass particle-filled epoxy resin,” *J. Mater. Sci.*, vol. 19, no. 2, pp. 473–486, Feb. 1984.

[69] R. A. Pearson and A. F. Yee, “Influence of particle size and particle size distribution on toughening mechanisms in rubber-modified epoxies,” *J. Mater. Sci.*, vol. 26, no. 14, pp. 3828–3844, Jul. 1991.

[70] D. . Hourston and J. . Lane, “The toughening of epoxy resins with thermoplastics: 1. Trifunctional epoxy resin-polyetherimide blends,”

Polymer (Guildf)., vol. 33, no. 7, pp. 1379–1383, Jan. 1992.

[71] R. A. Pearson and A. F. Yee, “Toughening mechanisms in thermoplastic-modified epoxies: 1. Modification using poly(phenylene oxide),” *Polymer (Guildf).*, vol. 34, no. 17, pp. 3658–3670, 1993.

[72] L. Boogh, B. Pettersson, and J.-A. E. Månson, “Dendritic hyperbranched polymers as tougheners for epoxy resins,” *Polymer (Guildf).*, vol. 40, no. 9, pp. 2249–2261, Apr. 1999.

[73] V. D. Ramos, H. M. da Costa, V. L. P. Soares, and R. S. V. Nascimento, “Modification of epoxy resin: a comparison of different types of elastomer,” *Polym. Test.*, vol. 24, no. 3, pp. 387–394, May 2005.

[74] A. J. Kinloch, “Toughening Epoxy Adhesives to Meet Today’s Challenges,” *MRS Bull.*, vol. 28, no. 06, pp. 445–448, Jun. 2003.

[75] A. C. Garg and Y.-W. Mai, “Failure mechanisms in toughened epoxy resins—A review,” *Compos. Sci. Technol.*, vol. 31, no. 3, pp. 179–223, Jan. 1988.

[76] “Standard test method for compressive properties of rigid plastics,” *ASTM D695-10*, 2010.

[77] N. Sela and O. Ishai, “Interlaminar fracture toughness and toughening of laminated composite materials: a review,” *Composites*, vol. 20, no. 5, pp. 423–435, Sep. 1989.

[78] O. Ishai, H. Rosenthal, N. Sela, and E. Drukker, “Effect of selective adhesive interleaving on interlaminar fracture toughness of graphite/epoxy composite laminates,” *Composites*, vol. 19, no. 1, pp. 49–54, Jan. 1988.

[79] A. N. Xuefeng, J. I. Shuangying, T. Bangming, Z. Zilong, and Y. Xiao-Su, “Toughness improvement of carbon laminates by periodic interleaving thin thermoplastic films,” *J. Mater. Sci. Lett.*, vol. 21, no. 22, pp. 1763–1765, 2002.

[80] N. H. Nash, T. M. Young, P. T. McGrail, and W. F. Stanley, “Inclusion of a

thermoplastic phase to improve impact and post-impact performances of carbon fibre reinforced thermosetting composites — A review," *Mater. Des.*, vol. 85, pp. 582–597, Nov. 2015.

[81] R. F. Gibson, "A review of recent research on mechanics of multifunctional composite materials and structures," *Compos. Struct.*, vol. 92, no. 12, pp. 2793–2810, Nov. 2010.

[82] S. U. Khan and J.-K. Kim, "Improved interlaminar shear properties of multiscale carbon fiber composites with bucky paper interleaves made from carbon nanofibers," *Carbon N. Y.*, vol. 50, no. 14, pp. 5265–5277, Nov. 2012.

[83] T. C. Chu, W. F. Ranson, and M. A. Sutton, "Applications of digital-image-correlation techniques to experimental mechanics," *Exp. Mech.*, vol. 25, no. 3, pp. 232–244, Sep. 1985.

[84] J. D. Helm, S. R. McNeill, and M. A. Sutton, "Improved three-dimensional image correlation for surface displacement measurement," *Opt. Eng.*, vol. 35, no. 7, p. 1911, Jul. 1996.

[85] M. A. Sutton, S. R. McNeill, J. D. Helm, and Y. J. Chao, "Advances in Two-Dimensional and Three-Dimensional Computer Vision," in *Photomechanics*, Berlin, Heidelberg: Springer Berlin Heidelberg, 2000, pp. 323–372.

[86] F. Hild and S. Roux, "Digital Image Correlation: from Displacement Measurement to Identification of Elastic Properties - a Review," *Strain*, vol. 42, no. 2, pp. 69–80, May 2006.

[87] M. A. Sutton, "Computer Vision-Based, Noncontacting Deformation Measurements in Mechanics: A Generational Transformation," *Appl. Mech. Rev.*, vol. 65, no. 5, p. 050802, Aug. 2013.

[88] H. Schreier, J.-J. Orteu, and M. A. Sutton, *Image Correlation for Shape, Motion and Deformation Measurements*. Boston, MA: Springer US, 2009.

[89] B. Pan, K. Qian, H. Xie, and A. Asundi, "Two-dimensional digital image

correlation for in-plane displacement and strain measurement: a review," *Meas. Sci. Technol.*, vol. 20, no. 6, p. 062001, Jun. 2009.

[90] H. W. Schreier, J. R. Braasch, and M. A. Sutton, "Systematic errors in digital image correlation caused by intensity interpolation," *Opt. Eng.*, vol. 39, no. 11, p. 2915, Nov. 2000.

[91] M. A. Sutton, J. L. Turner, H. A. Bruck, and T. A. Chae, "Full-field representation of discretely sampled surface deformation for displacement and strain analysis," *Exp. Mech.*, vol. 31, no. 2, pp. 168–177, Jun. 1991.

[92] B. Pan, A. Asundi, H. Xie, and J. Gao, "Digital image correlation using iterative least squares and pointwise least squares for displacement field and strain field measurements," *Opt. Lasers Eng.*, vol. 47, no. 7–8, pp. 865–874, Jul. 2009.

[93] M. A. Sutton, J. H. Yan, V. Tiwari, H. W. Schreier, and J. J. Orteu, "The effect of out-of-plane motion on 2D and 3D digital image correlation measurements," *Opt. Lasers Eng.*, vol. 46, no. 10, pp. 746–757, Oct. 2008.

[94] R. I. Hartley and P. Sturm, "Triangulation," 1997.

[95] Y.-Q. Q. Wang *et al.*, "On Error Assessment in Stereo-based Deformation Measurements," *Exp. Mech.*, vol. 51, no. 4, pp. 405–422, Apr. 2011.

[96] H. W. Schreier and M. A. Sutton, "Systematic errors in digital image correlation due to undermatched subset shape functions," *Exp. Mech.*, vol. 42, no. 3, pp. 303–310, Sep. 2002.

[97] A. K. Landauer, · M Patel, · D L Henann, and · C Franck, "A q-Factor-Based Digital Image Correlation Algorithm (qDIC) for Resolving Finite Deformations with Degenerate Speckle Patterns," *Exp. Mech.*, vol. 58, pp. 815–830, 2018.

[98] B. Pan, W. Dafang, and X. Yong, "Incremental calculation for large deformation measurement using reliability-guided digital image correlation," *Opt. Lasers Eng.*, vol. 50, no. 4, pp. 586–592, Apr. 2012.

[99] Y. Q. Wang, M. A. Sutton, H. A. Bruck, and H. W. Schreier, “Quantitative Error Assessment in Pattern Matching: Effects of Intensity Pattern Noise, Interpolation, Strain and Image Contrast on Motion Measurements,” *Strain*, vol. 45, no. 2, pp. 160–178, Apr. 2009.

[100] Y. L. Dong and B. Pan, “A Review of Speckle Pattern Fabrication and Assessment for Digital Image Correlation,” *Exp. Mech.*, vol. 57, no. 8, pp. 1161–1181, Oct. 2017.

[101] P. Reu, “Stereo-rig Design: Camera Selection-Part 2,” *Exp. Tech.*, vol. 36, no. 6, pp. 3–4, Nov. 2012.

[102] P. Reu, “Calibration: Sanity Checks,” *Exp. Tech.*, vol. 38, no. 2, pp. 1–2, Mar. 2014.

[103] S. T. Pinho, P. Robinson, and L. Iannucci, “Fracture toughness of the tensile and compressive fibre failure modes inlaminated composites,” *Compos. Sci. Technol.*, vol. 66, no. 13, pp. 1–26, 2005.

[104] W. Weber, “Ueber die specifische Wärme fester Körper, insbesondere der Metalle,” *Ann. der Phys. und Chemie*, vol. 96, no. 10, pp. 177–213, Jan. 1830.

[105] W. Thomson, “XV.—On the Dynamical Theory of Heat, with numerical results deduced from Mr Joule’s Equivalent of a Thermal Unit, and M. Regnault’s Observations on Steam,” *Trans. R. Soc. Edinburgh*, vol. 20, no. 02, pp. 261–288, Jan. 1853.

[106] K. T. Compton and D. B. Webster., “Temperature Changes Accompanying the Adiabatic Compression of Steel,” *Phys. Rev.*, vol. 5, no. 2, pp. 159–166, Feb. 1915.

[107] M. A. Biot, “Theory of Stress-Strain Relations in Anisotropic Viscoelasticity and Relaxation Phenomena,” *J. Appl. Phys.*, vol. 25, no. 11, pp. 1385–1391, Nov. 1954.

[108] M. A. Biot, “Theory of Elasticity and Consolidation for a Porous Anisotropic Solid,” *J. Appl. Phys.*, vol. 26, no. 2, pp. 182–185, Feb. 1955.

[109] M. A. Biot, “Variational Principles in Irreversible Thermodynamics with

Application to Viscoelasticity," *Phys. Rev.*, vol. 97, no. 6, pp. 1463–1469, Mar. 1955.

[110] M. A. Biot, "Thermoelasticity and Irreversible Thermodynamics," *J. Appl. Phys.*, vol. 27, no. 3, pp. 240–253, Mar. 1956.

[111] R. T. Potter and L. J. Greaves, "The Application Of Thermoelastic Stress Analysis Techniques To Fibre Composites," 1987, vol. 0817, p. 134.

[112] A. S. Machin, J. G. Sparrow, and M. G. Stimson, "Mean stress dependence of the thermoelastic constant," *Strain*, vol. 23, no. 1, pp. 27–30, Feb. 1987.

[113] N. F. Enke, "An Enhanced Theory for Thermographic Stress Analysis of Isotropic Materials," 1989, vol. 1084, p. 84.

[114] S. Quinn, J. M. Dulieu-Barton, and J. M. Langlands, "Progress in thermoelastic residual stress measurement," *Strain*, vol. 40, no. 3, pp. 127–133, Aug. 2004.

[115] A. K. Wong, J. G. Sparrow, and S. A. Dunn, "On the revised theory of the thermoelastic effect," *J. Phys. Chem. Solids*, vol. 49, no. 4, pp. 395–400, 1988.

[116] M. A. Bramson, *Infrared radiation: A handbook for applications*. Plenum Press, 1968.

[117] A. Rogalski, "Infrared detectors: an overview," *Infrared Phys. Technol.*, vol. 43, no. 3–5, pp. 187–210, Jun. 2002.

[118] A. Daniels, *Field Guide to Infrared Systems, Detectors, and FPAs*, 2nd ed. SPIE, 2010.

[119] M. H. Belgen, "Structural stress measurements with an infrared radiometer," *ISA Trans. 6*, vol. 6, pp. 49–53, 1967.

[120] D. S. Mountain and J. M. B. Webber, "Stress Pattern Analysis By Thermal Emission (SPATE)," 1979, vol. 0164, pp. 189–196.

[121] A. Rogalski, *Infrared Detectors, Second Edition*. CRC Press, 2010.

[122] J. R. Lesniak and B. R. Boyce, "A High-Speed Differential Thermographic

Camera."

[123] J. M. Dulieu-Smith, "Alternative calibration techniques for quantitative thermoelastic stress analysis," *Strain*, vol. 31, no. 1, pp. 9–16, Feb. 1995.

[124] P. Stanley and W. K. Chan, "The application of thermoelastic stress analysis techniques to composite materials," *J. Strain Anal. Eng. Des.*, vol. 23, no. 3, pp. 137–143, Jul. 1988.

[125] R. T. Potter, "Stress Analysis In Laminated Fibre Composites By Thermoelastic Emission," 1987, vol. 0731, p. 110.

[126] T. R. R. Emery, J. M. M. Dulieu-Barton, J. S. S. Earl, and P. R. R. Cunningham, "A generalised approach to the calibration of orthotropic materials for thermoelastic stress analysis," *Compos. Sci. Technol.*, vol. 68, no. 3–4, pp. 743–752, Mar. 2008.

[127] C. E. Bakis and K. L. Reifsnider, "The Adiabatic Thermoelastic Effect in Laminated Fiber Composites," *J. Compos. Mater.*, vol. 25, no. 7, pp. 809–830, Jul. 1991.

[128] A. K. K. Wong, "A non-adiabatic thermoelastic theory for composite laminates," *J. Phys. Chem. Solids*, vol. 52, no. 3, pp. 483–494, Jan. 1991.

[129] A. K. Mackenzie, "Effects Of Surface Coatings On Infra-Red Measurements Of Thermoelastic Responses," 1989, vol. 1084, p. 59.

[130] S. Barone and E. A. Patterson, "Polymer coating as a strain witness in thermoelasticity."

[131] A. F. Robinson, J. M. Dulieu-Barton, S. Quinn, and R. L. Burguete, "Paint coating characterization for thermoelastic stress analysis of metallic materials," *Meas. Sci. Technol.*, vol. 21, no. 8, p. 085502, Aug. 2010.

[132] S. Sambasivam, S. Quinn, and J. M. Dulieu-Barton, "Identification of the source of the thermoelastic response from orthotropic laminated composites," in *Proceedings of the 17th International Conference on Composite Materials*, 2009.

[133] P. R. Cunningham, J. M. Dulieu-Barton, A. G. Dutton, and R. A. Shenoi,

"Thermoelastic Characterisation of Damage Around a Circular Hole in a GRP Component," *Key Eng. Mater.*, vol. 204–205, pp. 453–0, Apr. 2001.

[134] G. P. Horn, T. J. Mackin, and P. Kurath, "Estimating the residual fatigue lifetimes of impact-damaged composites using thermoelastic stress analysis," *Polym. Compos.*, vol. 22, no. 3, pp. 420–431, Jun. 2001.

[135] G. P. Horn, T. J. Mackin, and P. Kurath, "Composite machining damage quantification using thermoelastic stress analysis," *Polym. Compos.*, vol. 23, no. 2, pp. 193–200, Apr. 2002.

[136] T. Emery, J. Dulieu-Barton, and P. Cunningham, "Subsurface damage location and identification using infrared techniques," *17th Int. Conf. Compos. Mater.*, 2009.

[137] J. M. Dulieu-Barton, T. R. Emery, S. Quinn, and P. R. Cunningham, "A temperature correction methodology for quantitative thermoelastic stress analysis and damage assessment," *Meas. Sci. Technol.*, vol. 17, no. 6, pp. 1627–1637, Jun. 2006.

[138] T. R. Emery and J. M. Dulieu-Barton, "Thermoelastic Stress Analysis of damage mechanisms in composite materials," *Compos. Part A Appl. Sci. Manuf.*, vol. 41, no. 12, pp. 1729–1742, Dec. 2010.

[139] D. Van Hemelrijck, L. Schillemans, A. H. Cardon, and A. K. Wong, "The effects of motion on thermoelastic stress analysis," *Compos. Struct.*, vol. 18, no. 3, pp. 221–238, Jan. 1991.

[140] M. L. Silva, "Damage Evolution in Composite Materials and Sandwich Structures Under Impulse Loading," California Institute of Technology, 2001.

[141] R. K. Fruehmann, J. M. Dulieu-Barton, and S. Quinn, "Assessment of fatigue damage evolution in woven composite materials using infra-red techniques," *Compos. Sci. Technol.*, vol. 70, no. 6, pp. 937–946, Jun. 2010.

[142] W. Wang, R. K. Fruehmann, and J. M. Dulieu-Barton, "Application of Digital Image Correlation to Address Complex Motions in Thermoelastic

Stress Analysis," *Strain*, vol. 51, no. 5, pp. 405–418, 2015.

[143] P. A. Temple, "An introduction to phase-sensitive amplifiers: An inexpensive student instrument," *Am. J. Phys.*, vol. 43, no. 9, pp. 801–807, 1975.

[144] C. E. Shannon, "Communication in the Presence of Noise," *Proc. IRE*, vol. 37, no. 1, pp. 10–21, Jan. 1949.

[145] S. Giancane, F. W. Panella, R. Nobile, and V. Dattoma, "Fatigue damage evolution of fiber reinforced composites with digital image correlation analysis," *Procedia Eng.*, no. 2, pp. 1307–1315, 2010.

[146] R. K. Fruehmann, J. M. Dulieu-Barton, S. Quinn, and J. P. Tyler, "The use of a lock-in amplifier to apply digital image correlation to cyclically loaded components," *Opt. Lasers Eng.*, vol. 68, pp. 149–159, May 2015.

[147] D. Chen, S. Sun, J. M. Dulieu-Barton, Q. Li, and W. Wang, "Crack growth analysis in welded and non-welded T-joints based on lock-in digital image correlation and thermoelastic stress analysis," *Int. J. Fatigue*, vol. 110, pp. 172–185, May 2018.

[148] D. G. Kleinbaum and M. Klein, *Survival Analysis*. New York, NY: Springer New York, 2012.

[149] N. Reid, *Analysis of Survival Data*. Routledge, 2018.

[150] J. F. Lawless, *Statistical models and methods for lifetime data*. Wiley-Interscience, 2003.

[151] "DOT/FAA/AR-10/6: Determining the Fatigue Life of Composite Aircraft Structures Using Life and Load-Enhancement," 2011.

APPENDIX A. OHC FIXTURE DRAWINGS

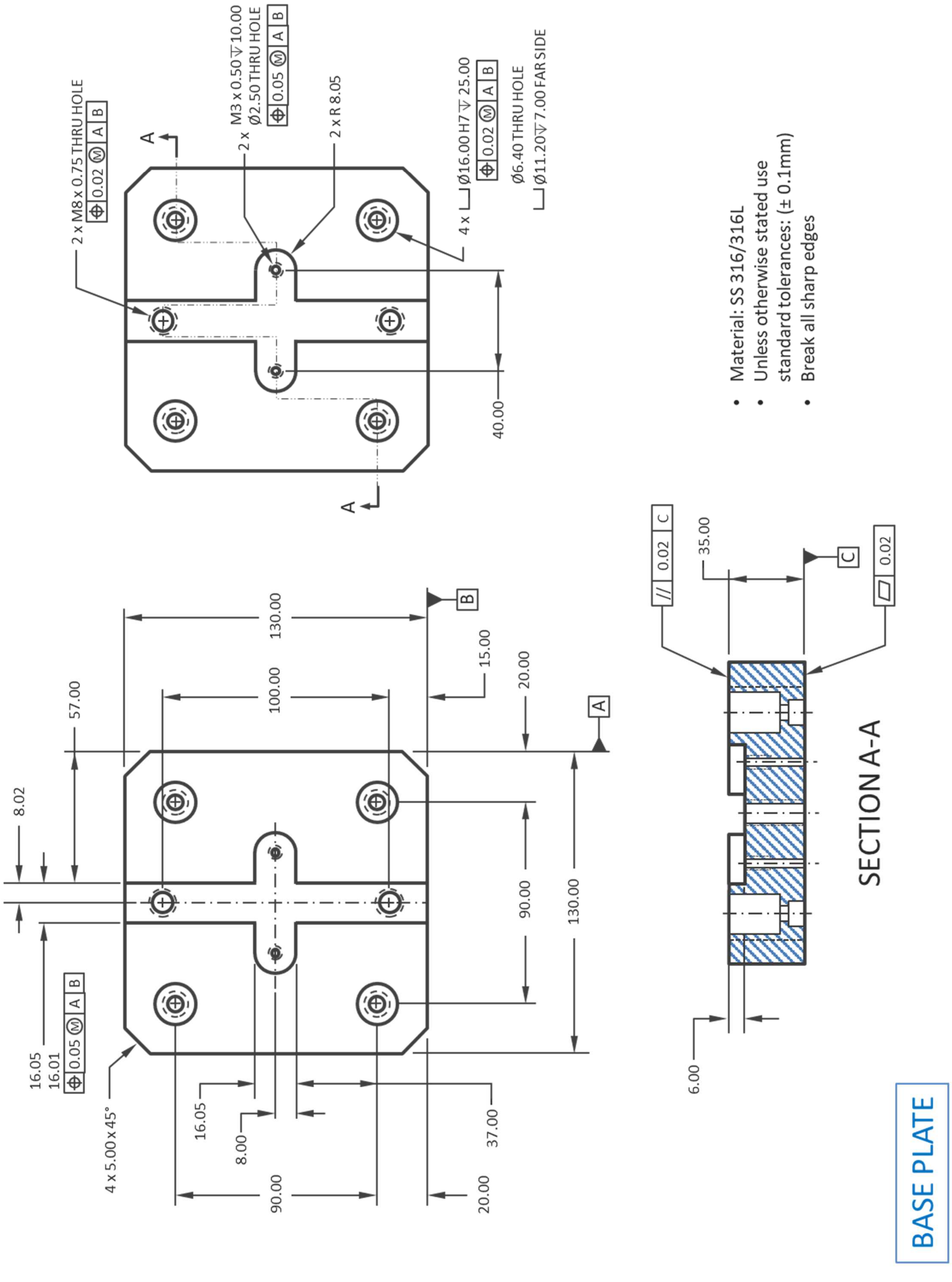

- Material: SS 316/316L
- Unless otherwise stated use standard tolerances: (± 0.1mm)
- Break all sharp edges

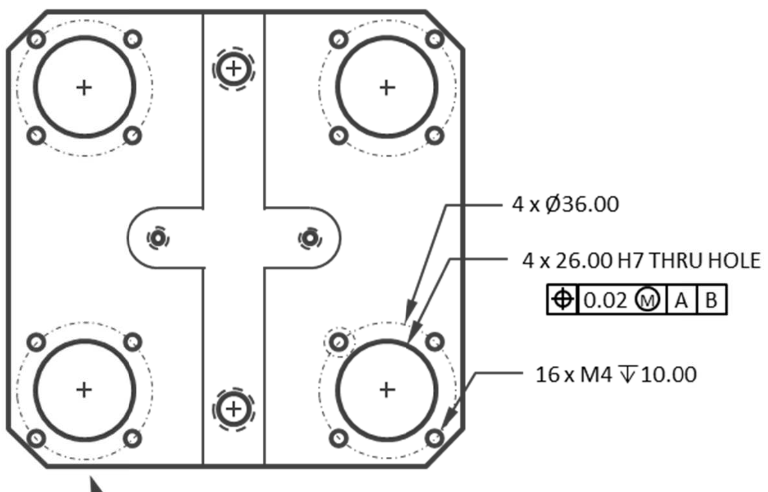

Bottom plate thickness is 36.5 mm

Machine cutouts for the bearing flanges of 6.5 depth on the slots side.

All dimensions, tolerances, datums and materials are the same as in "Base Plate" except those indicated

- Material: SS 316/316L
- Unless otherwise stated use standard tolerances: (± 0.1mm)
- Break all sharp edges

TOP PLATE

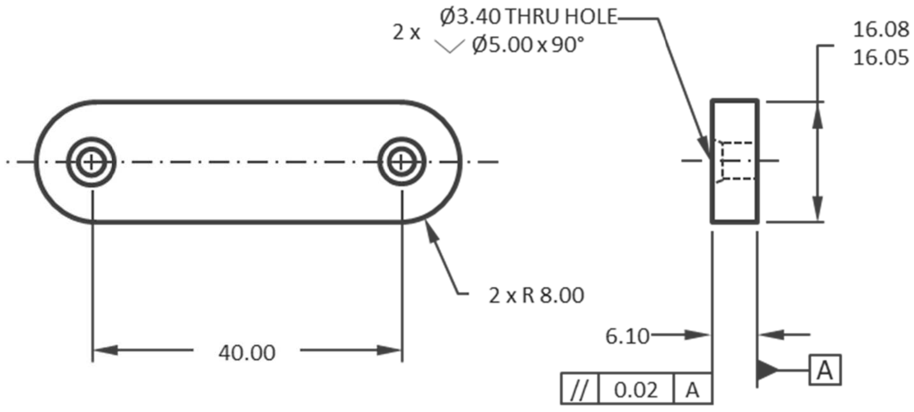

- Material: SS 316/316L
- Unless otherwise stated use standard tolerances: (± 0.1mm)
- Break all sharp edges

STOP TAB

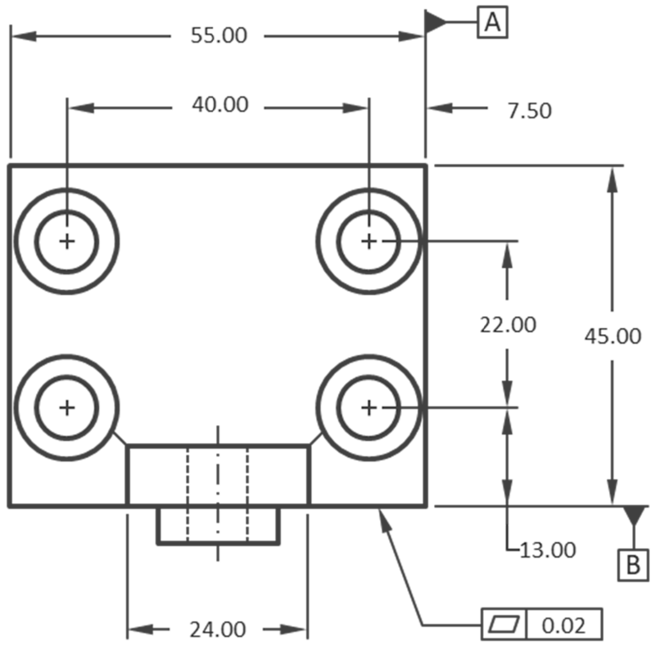

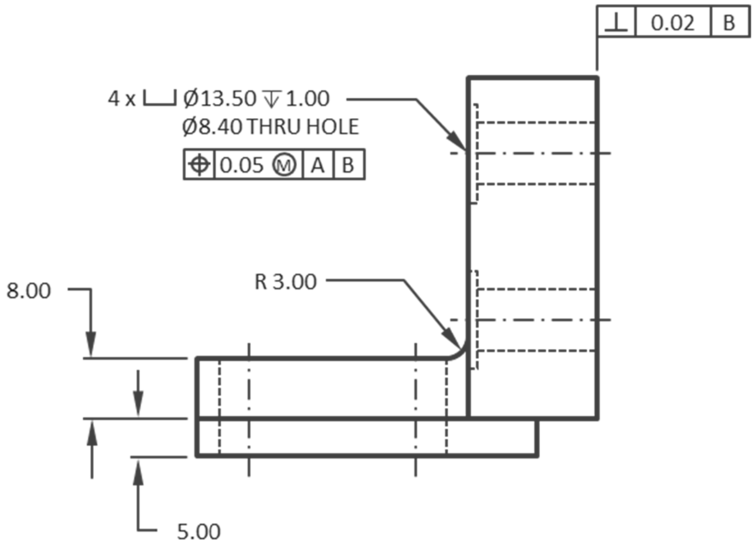

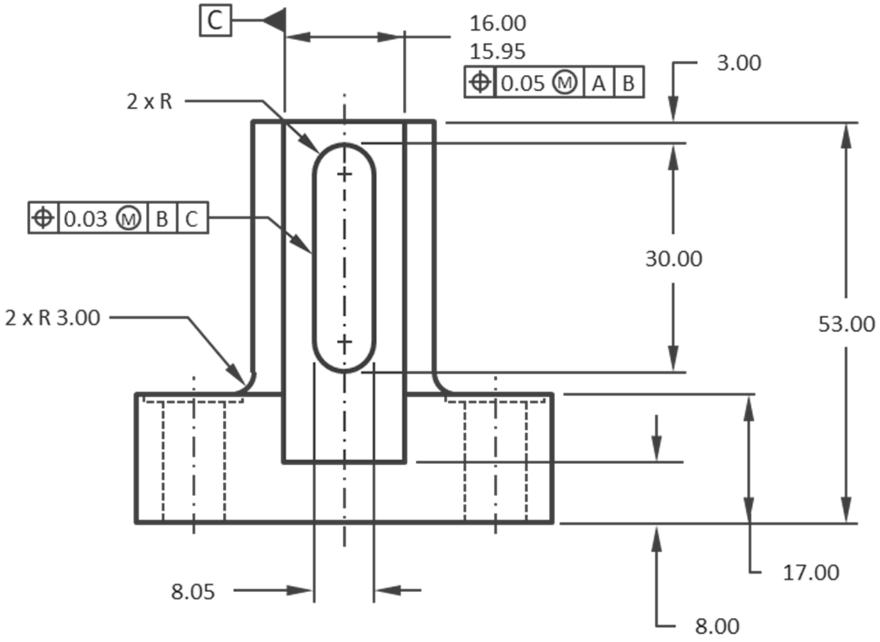

- Material: SS 316/316L
- Unless otherwise stated use standard tolerances: (± 0.1mm)
- Break all sharp edges

CLAMP

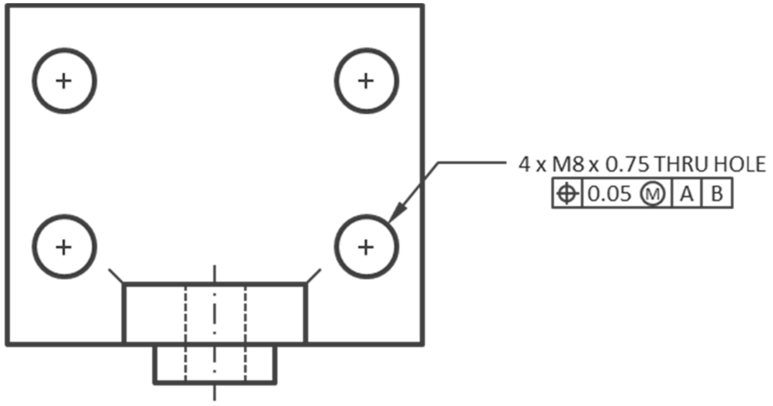

All dimensions, tolerances and datums are the same as in "Clamp" except those indicated

- Material: SS 316/316L
- Unless otherwise stated use standard tolerances: (± 0.1mm)
- Break all sharp edges

THREADED CLAMP

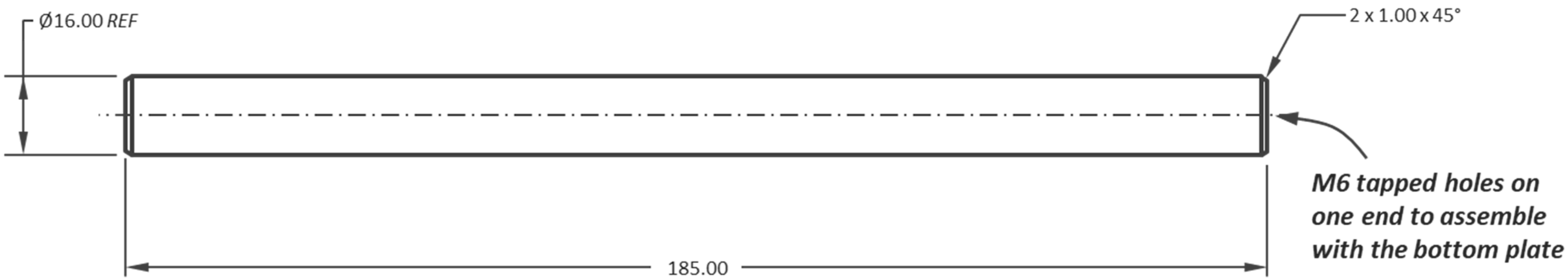

M6 tapped holes on one end to assemble with the bottom plate

GUIDE ROD

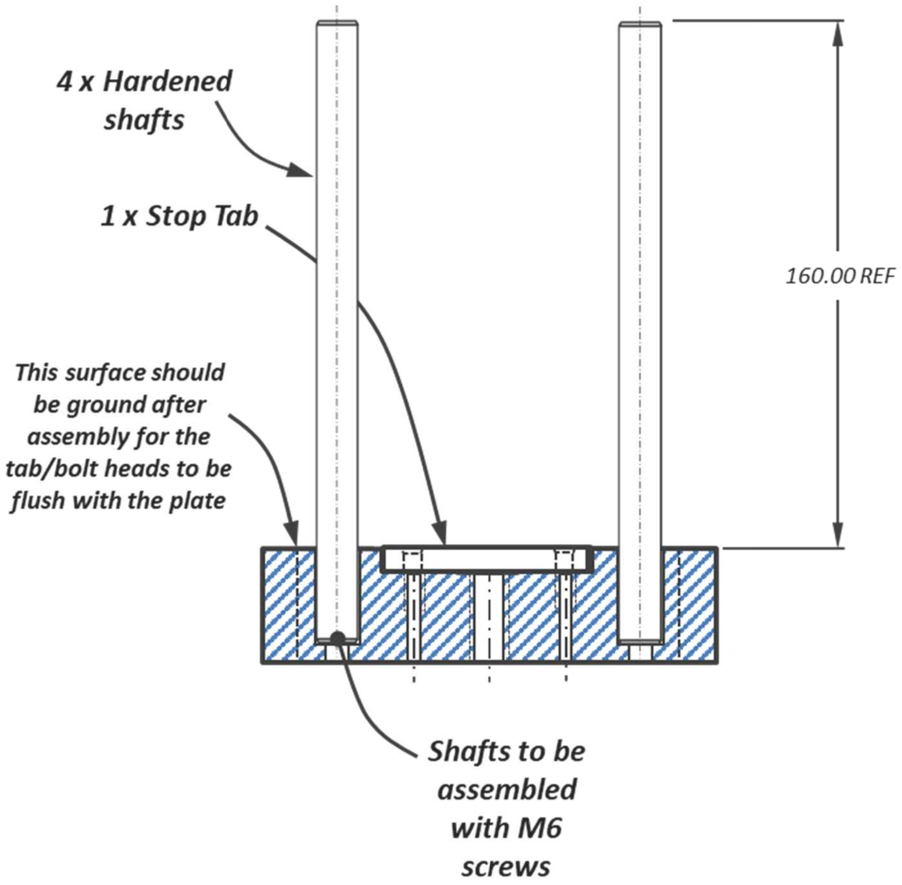

ASSEMBLY: BASE PLATE

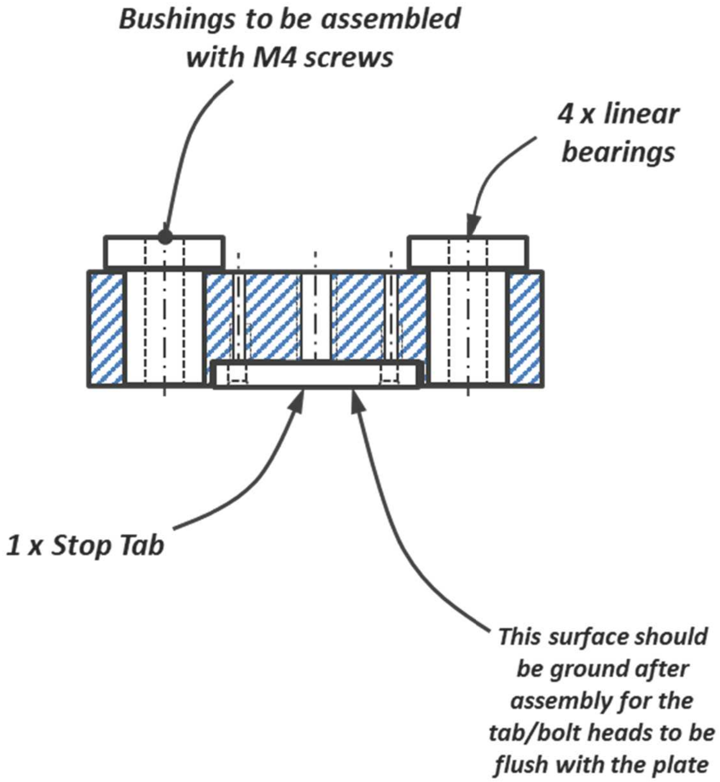

ASSEMBLY: TOP PLATE

Items

Description	Quantity	Material / Part No.
Base Plate	1	316/316L
Top Plate	1	
Clamp	2	
Threaded Clamp	2	
Stop Tab	2	
Linear ball bushings	4	L1721.016
Shafts	4	L1772.16-0200

Screws

Thread size	Head type	Length	Quantity
M8 x 0.75	Socket	50.00	8
		30.00	4
M6	Socket	Ad hoc	4
M4	Socket	Ad hoc	16
M3 x 0.50	Countersunk	12.00	4

APPENDIX B. BL ANALOGUE HISTORIES

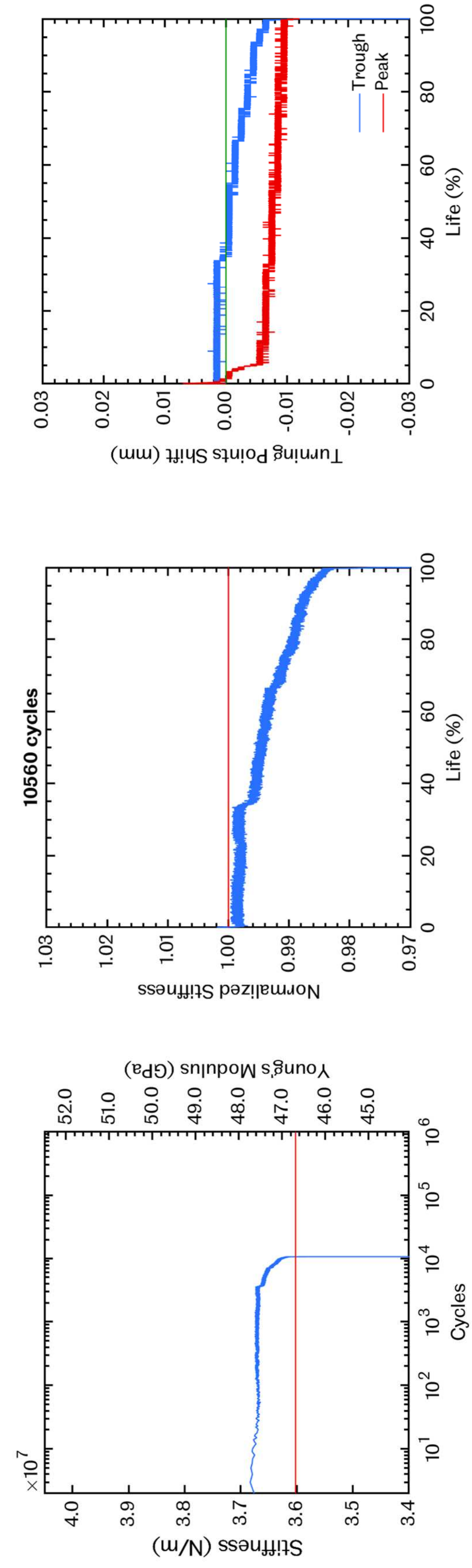

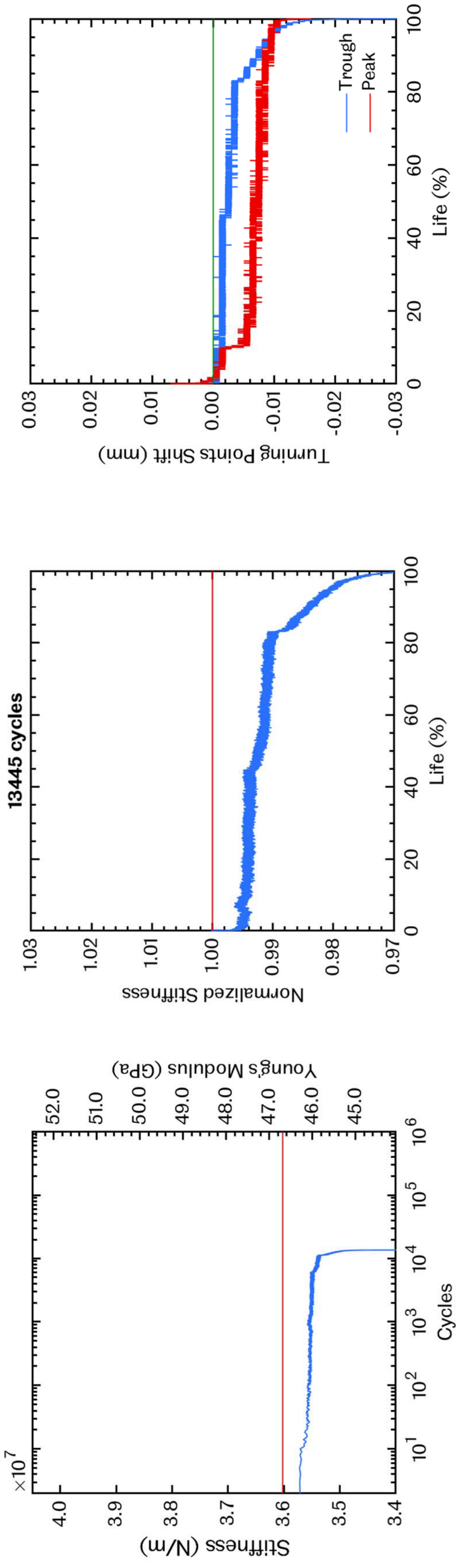

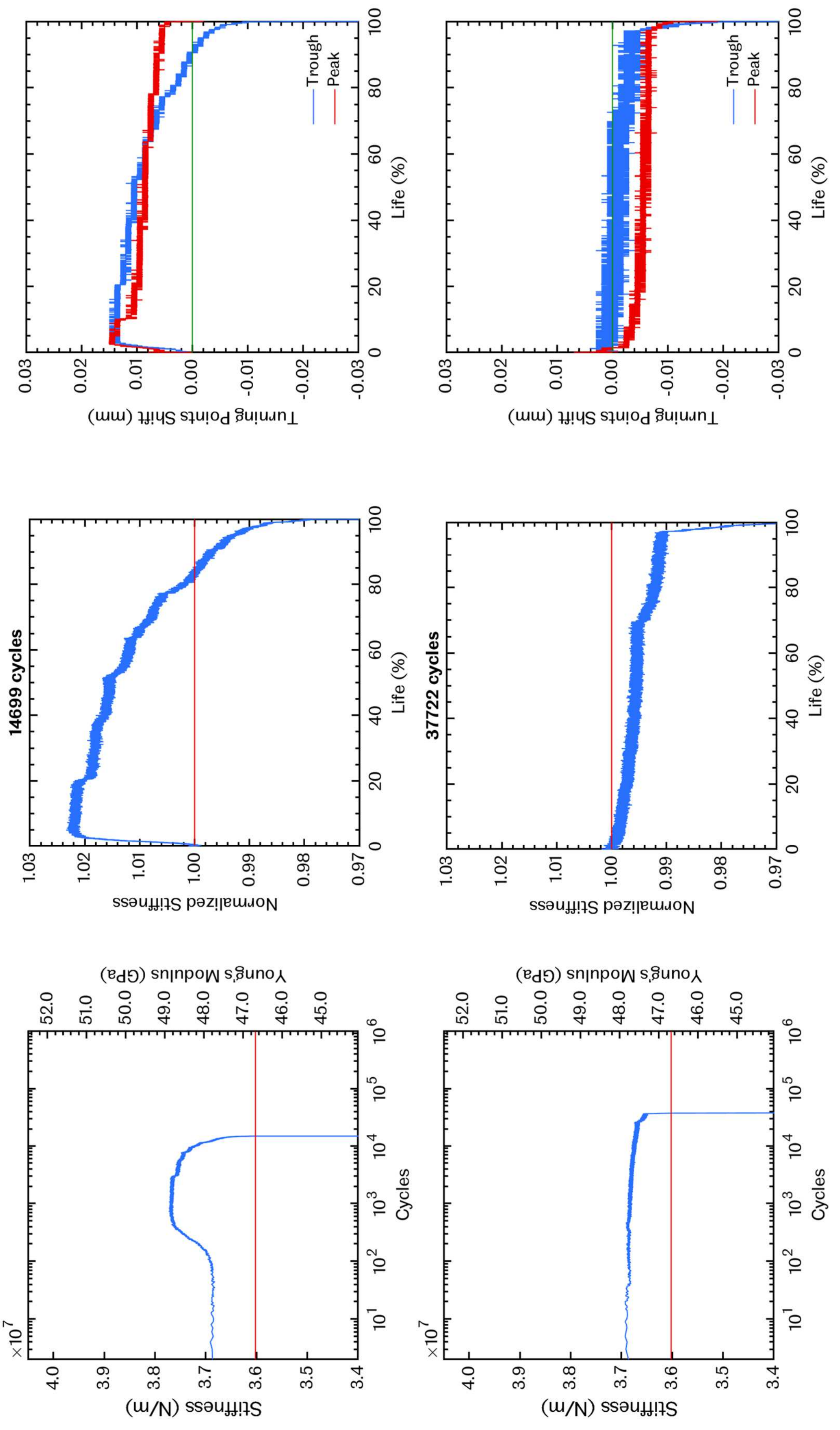
14699 cycles
37722 cycles
Stiffness (N/m)
×10^7
Young's Modulus (GPa)
Cycles
Normalized Stiffness
Life (%)
Turning Points Shift (mm)
Trough
Peak

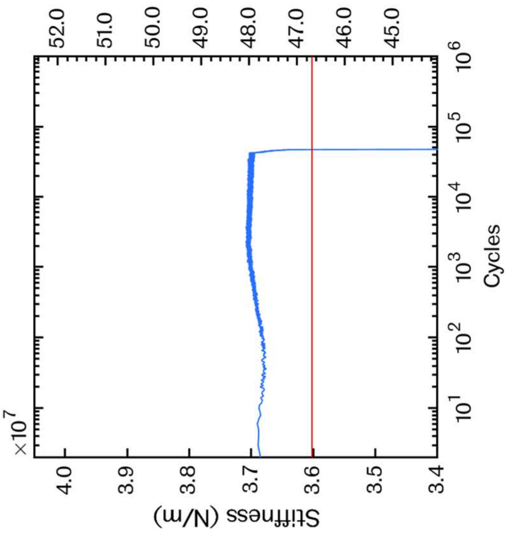
×10^7
Stiffness (N/m)
4.0
3.9
3.8
3.7
3.6
3.5
3.4
Cycles
10^1
10^2
10^3
10^4
10^5
10^6
Young's Modulus (GPa)
52.0
51.0
50.0
49.0
48.0
47.0
46.0
45.0

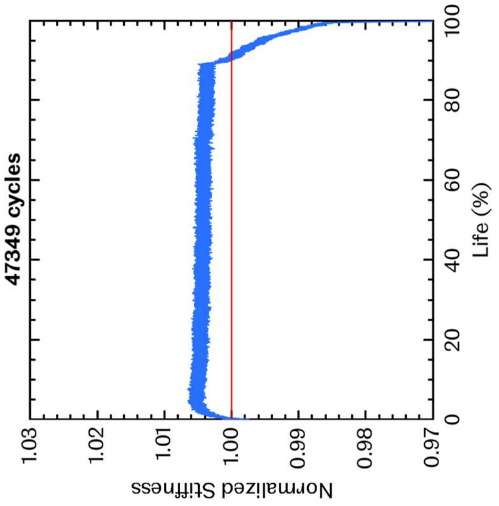
47349 cycles
Normalized Stiffness
1.03
1.02
1.01
1.00
0.99
0.98
0.97
Life (%)
0
20
40
60
80
100

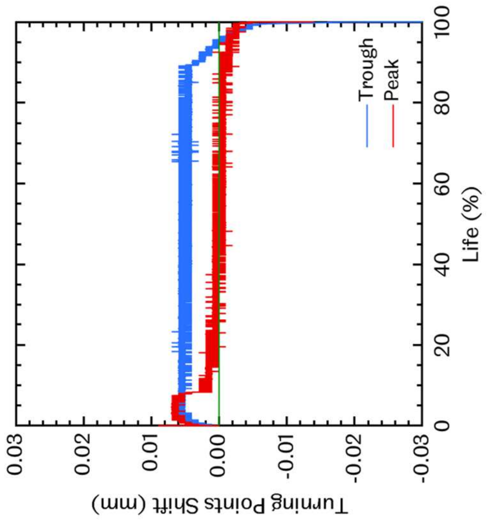
Turning Points Shift (mm)
0.03
0.02
0.01
0.00
-0.01
-0.02
-0.03
Life (%)
0
20
40
60
80
100
Trough
Peak

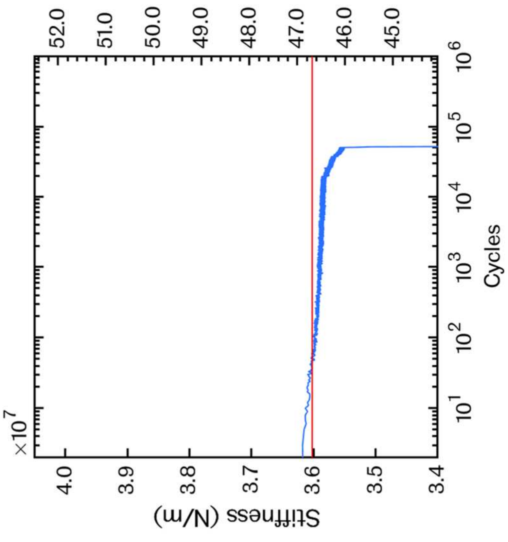
×10^7
Stiffness (N/m)
4.0
3.9
3.8
3.7
3.6
3.5
3.4
Cycles
10^1
10^2
10^3
10^4
10^5
10^6
Young's Modulus (GPa)
52.0
51.0
50.0
49.0
48.0
47.0
46.0
45.0

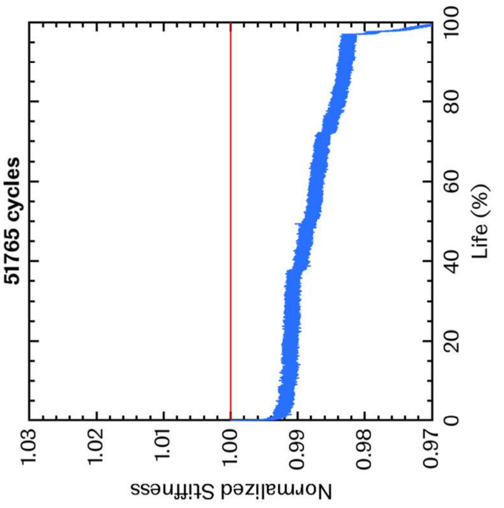
51765 cycles
Normalized Stiffness
1.03
1.02
1.01
1.00
0.99
0.98
0.97
Life (%)
0
20
40
60
80
100

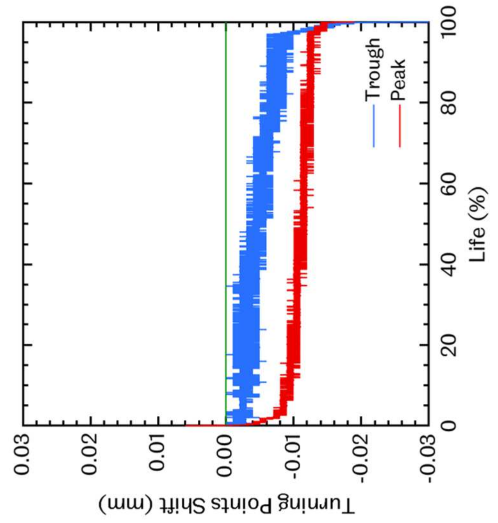
Turning Points Shift (mm)
0.03
0.02
0.01
0.00
-0.01
-0.02
-0.03
Life (%)
0
20
40
60
80
100
Trough
Peak

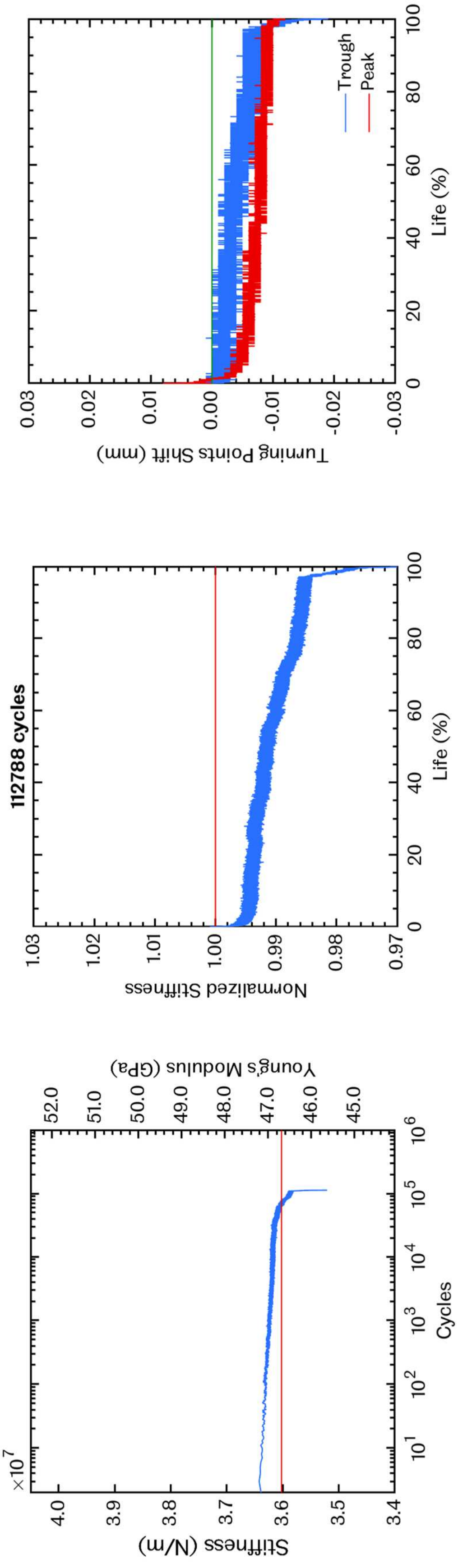
112788 cycles
Stiffness (N/m)
×10^7
4.0
3.9
3.8
3.7
3.6
3.5
3.4
Cycles
10^1
10^2
10^3
10^4
10^5
10^6
Young's Modulus (GPa)
52.0
51.0
50.0
49.0
48.0
47.0
46.0
45.0
Normalized Stiffness
1.03
1.02
1.01
1.00
0.99
0.98
0.97
Life (%)
0
20
40
60
80
100
Turning Points Shift (mm)
0.03
0.02
0.01
0.00
-0.01
-0.02
-0.03
Trough
Peak

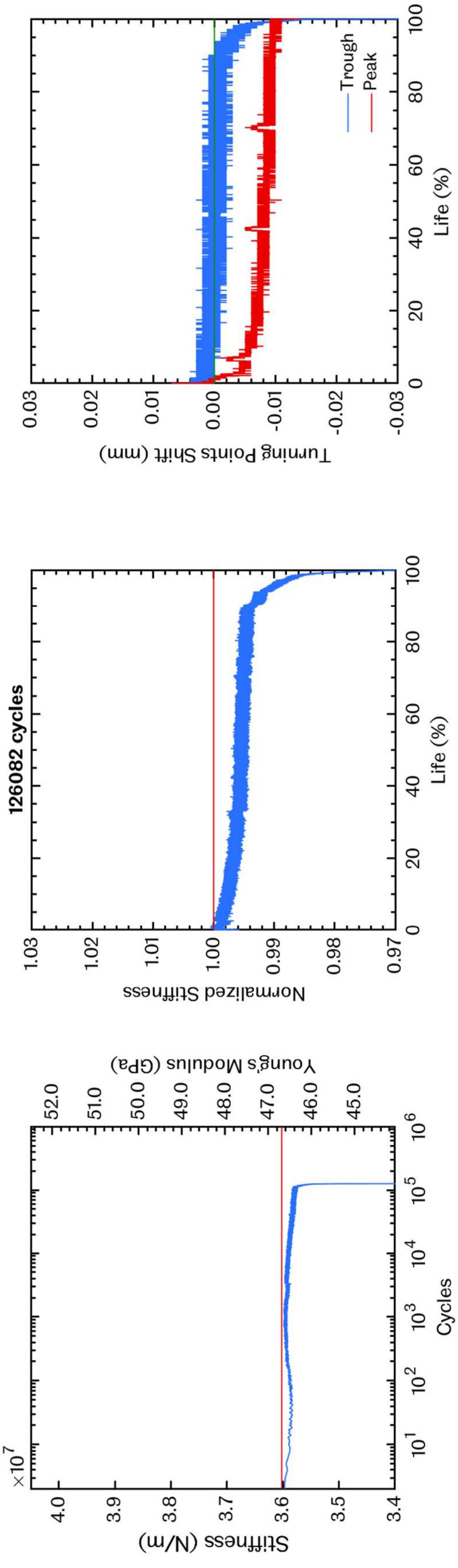
126082 cycles
Stiffness (N/m)
×10^7
4.0
3.9
3.8
3.7
3.6
3.5
3.4
Cycles
10^1
10^2
10^3
10^4
10^5
10^6
Young's Modulus (GPa)
52.0
51.0
50.0
49.0
48.0
47.0
46.0
45.0
Normalized Stiffness
1.03
1.02
1.01
1.00
0.99
0.98
0.97
Life (%)
0
20
40
60
80
100
Turning Points Shift (mm)
0.03
0.02
0.01
0.00
-0.01
-0.02
-0.03
Trough
Peak

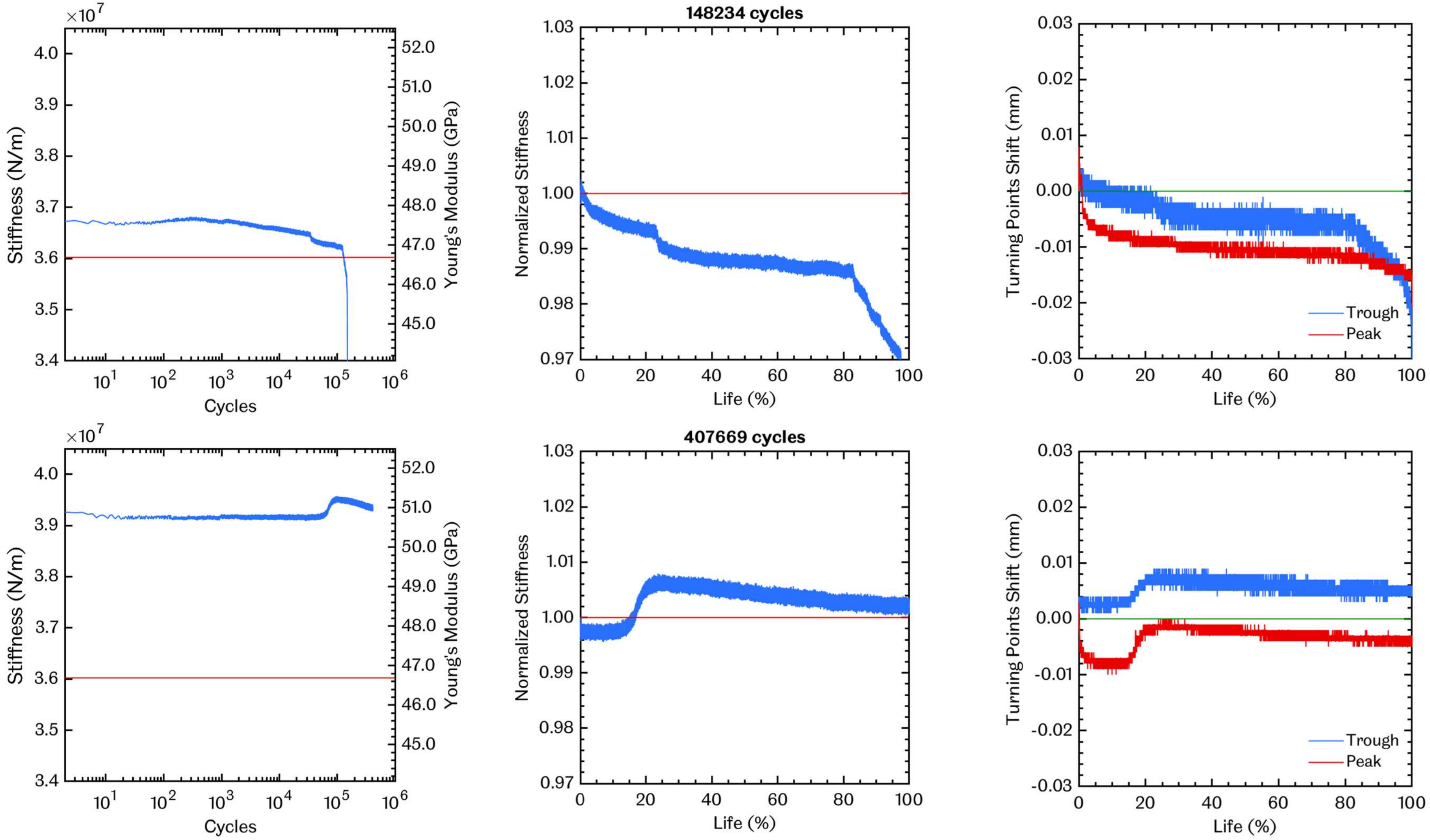
×10^7
Stiffness (N/m)
4.0
3.9
3.8
3.7
3.6
3.5
3.4
Young's Modulus (GPa)
52.0
51.0
50.0
49.0
48.0
47.0
46.0
45.0
10^1
10^2
10^3
10^4
10^5
10^6
Cycles
148234 cycles
Normalized Stiffness
1.03
1.02
1.01
1.00
0.99
0.98
0.97
0
20
40
60
80
100
Life (%)
Turning Points Shift (mm)
0.03
0.02
0.01
0.00
-0.01
-0.02
-0.03
Trough
Peak
407669 cycles

APPENDIX C. T3 ANALOGUE HISTORIES

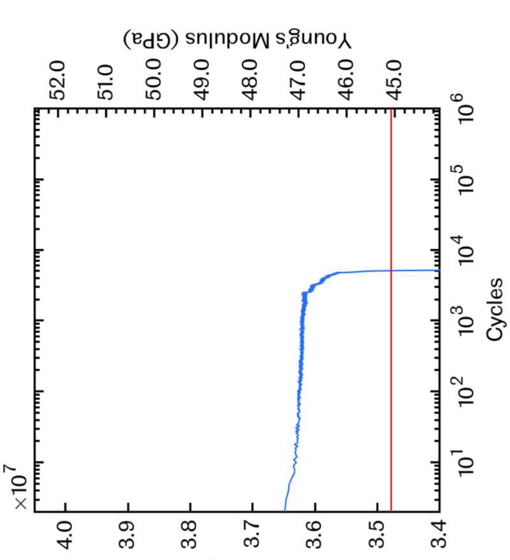

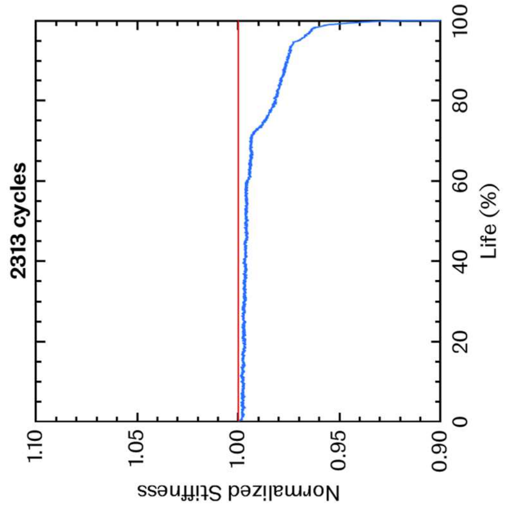

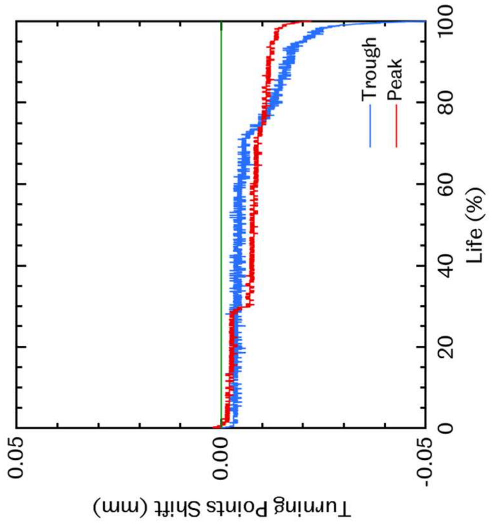

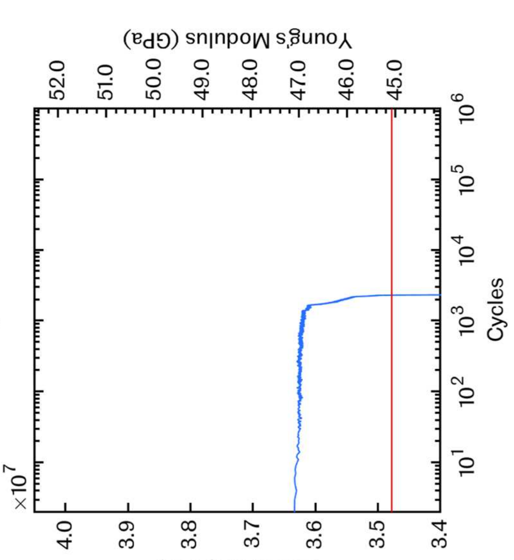

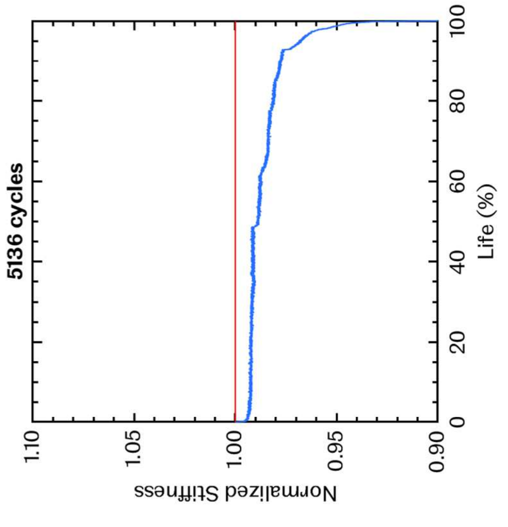

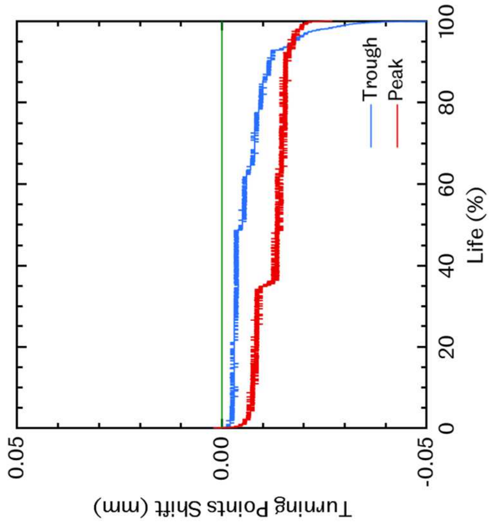

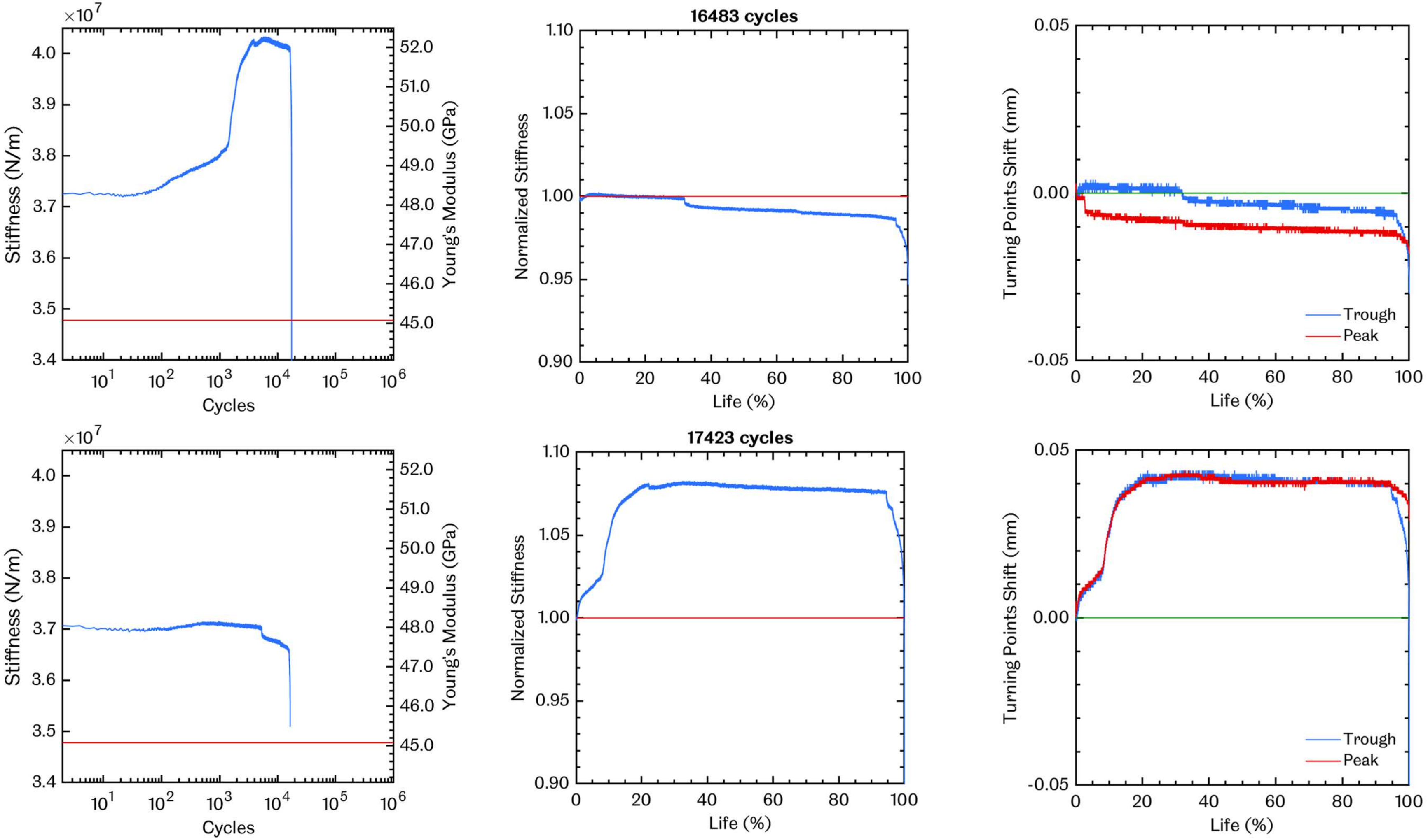
×10^7
Stiffness (N/m)
4.0
3.9
3.8
3.7
3.6
3.5
3.4
Young's Modulus (GPa)
52.0
51.0
50.0
49.0
48.0
47.0
46.0
45.0
Cycles
10^1
10^2
10^3
10^4
10^5
10^6
16483 cycles
17423 cycles
Normalized Stiffness
1.10
1.05
1.00
0.95
0.90
Life (%)
0
20
40
60
80
100
Turning Points Shift (mm)
0.05
0.00
-0.05
Trough
Peak

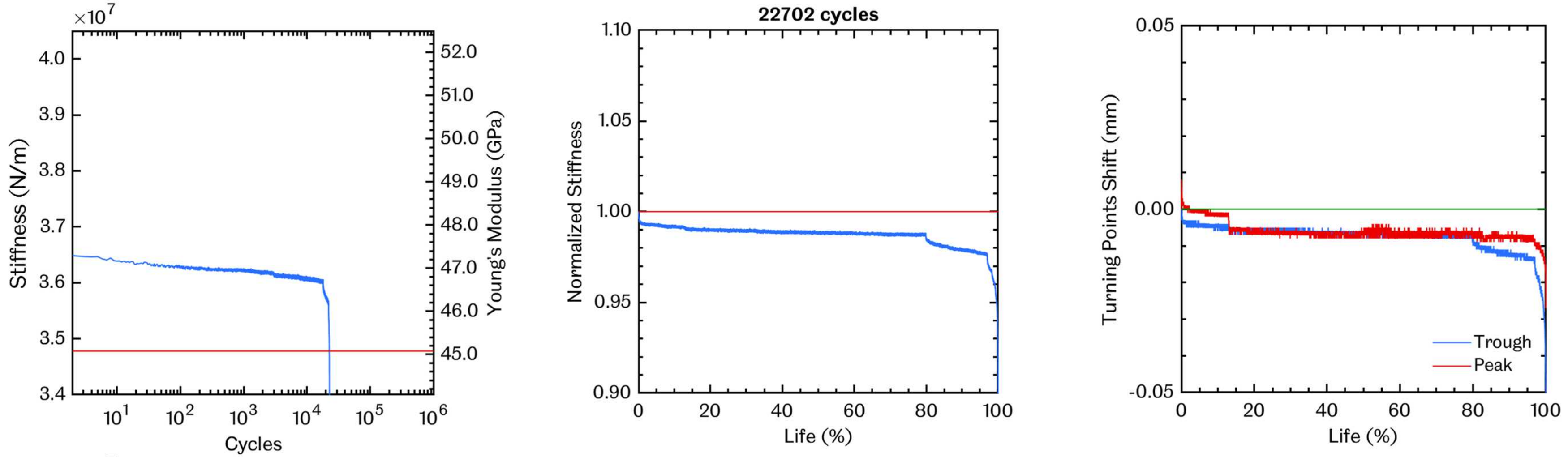
×10^7
Stiffness (N/m)
4.0
3.9
3.8
3.7
3.6
3.5
3.4
10^1
10^2
10^3
10^4
10^5
10^6
Cycles
Young's Modulus (GPa)
52.0
51.0
50.0
49.0
48.0
47.0
46.0
45.0
22702 cycles
Normalized Stiffness
1.10
1.05
1.00
0.95
0.90
0
20
40
60
80
100
Life (%)
Turning Points Shift (mm)
0.05
0.00
-0.05
Trough
Peak

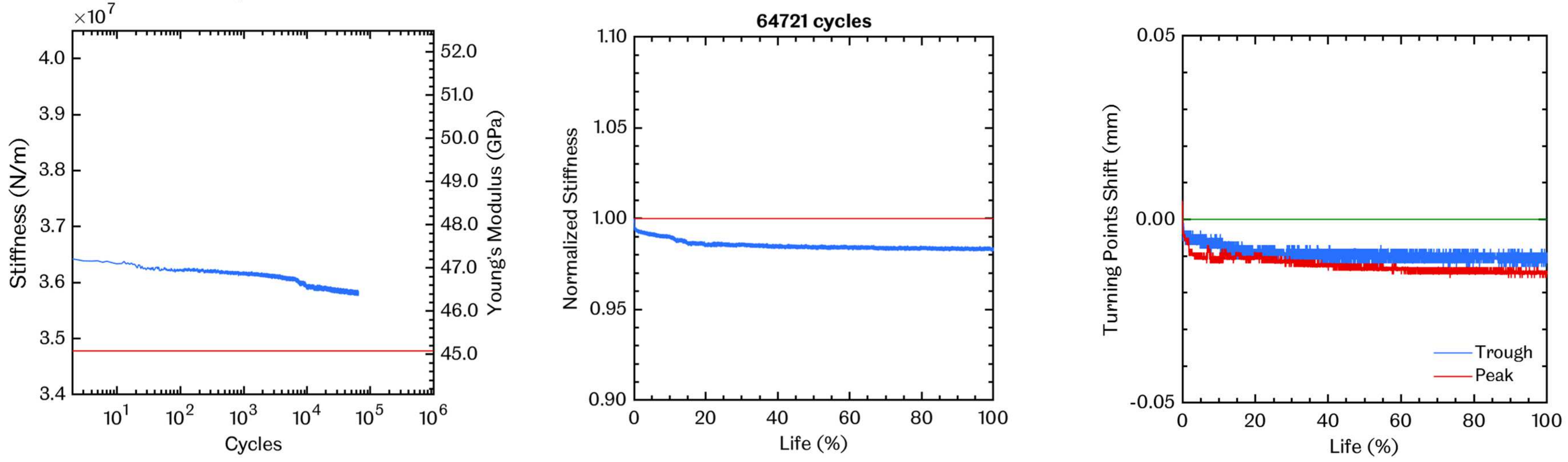
×10^7
Stiffness (N/m)
4.0
3.9
3.8
3.7
3.6
3.5
3.4
10^1
10^2
10^3
10^4
10^5
10^6
Cycles
Young's Modulus (GPa)
52.0
51.0
50.0
49.0
48.0
47.0
46.0
45.0
64721 cycles
Normalized Stiffness
1.10
1.05
1.00
0.95
0.90
0
20
40
60
80
100
Life (%)
Turning Points Shift (mm)
0.05
0.00
-0.05
Trough
Peak

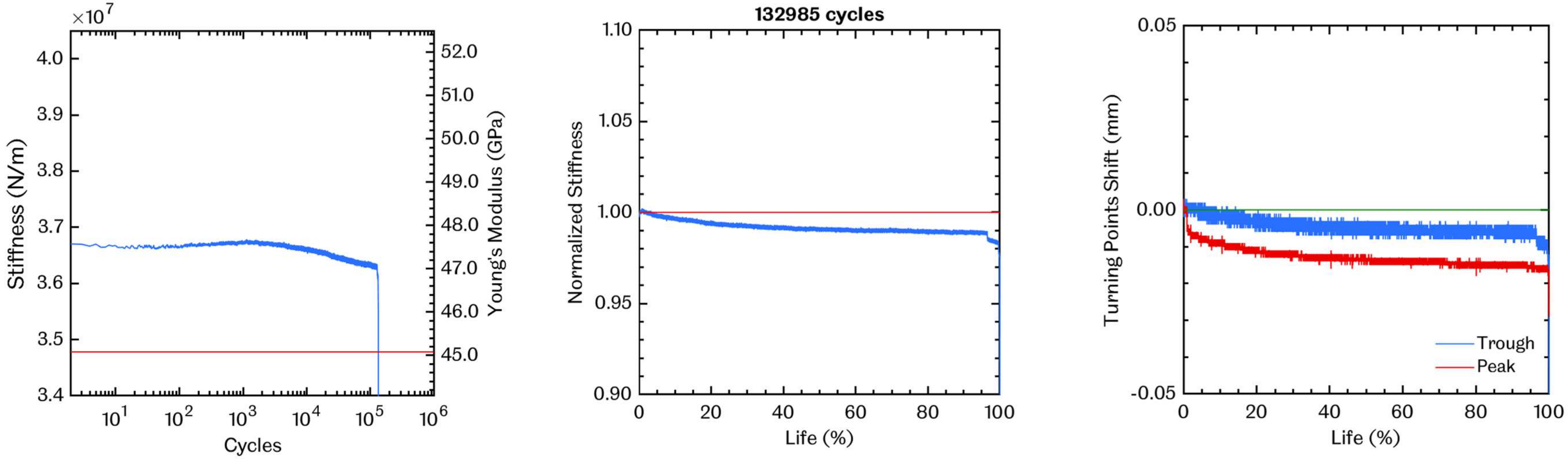
×10^7
Stiffness (N/m)
4.0
3.9
3.8
3.7
3.6
3.5
3.4
10^1
10^2
10^3
10^4
10^5
10^6
Cycles
Young's Modulus (GPa)
52.0
51.0
50.0
49.0
48.0
47.0
46.0
45.0
132985 cycles
Normalized Stiffness
1.10
1.05
1.00
0.95
0.90
0
20
40
60
80
100
Life (%)
Turning Points Shift (mm)
0.05
0.00
-0.05
Trough
Peak
0
20
40
60
80
100
Life (%)

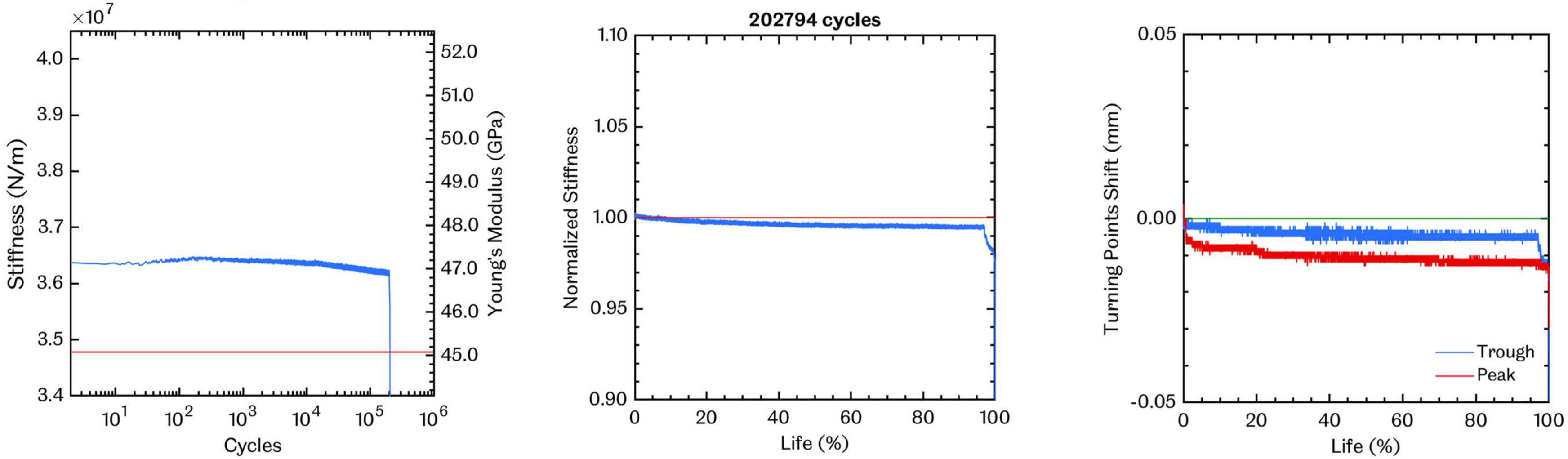
×10^7
Stiffness (N/m)
4.0
3.9
3.8
3.7
3.6
3.5
3.4
10^1
10^2
10^3
10^4
10^5
10^6
Cycles
Young's Modulus (GPa)
52.0
51.0
50.0
49.0
48.0
47.0
46.0
45.0
202794 cycles
Normalized Stiffness
1.10
1.05
1.00
0.95
0.90
0
20
40
60
80
100
Life (%)
Turning Points Shift (mm)
0.05
0.00
-0.05
Trough
Peak
0
20
40
60
80
100
Life (%)

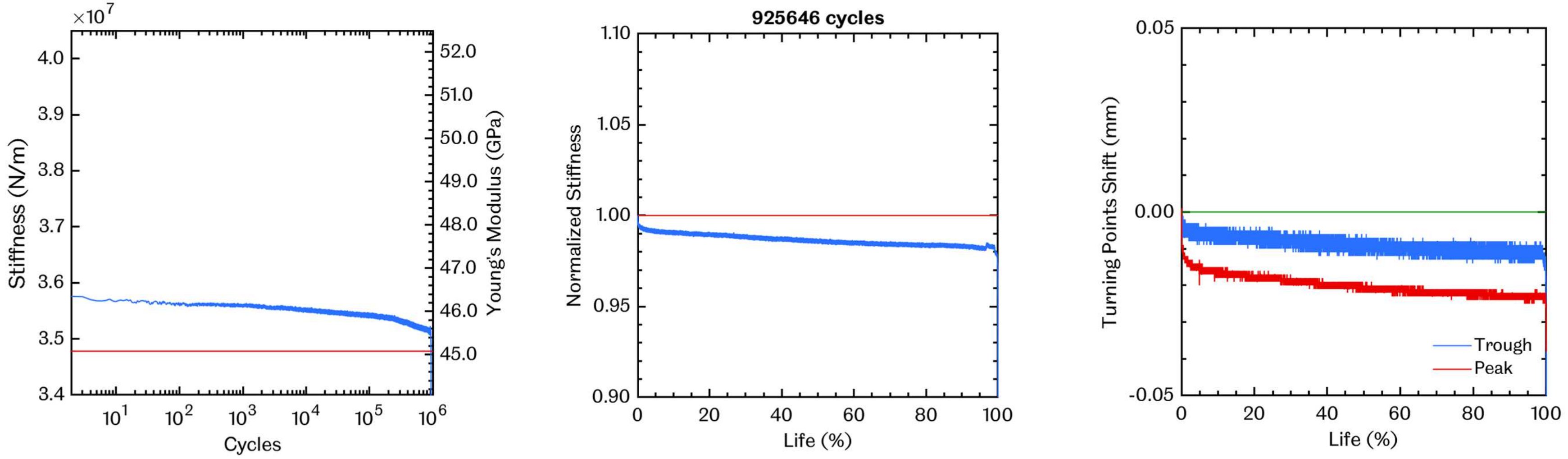
×10^7
Stiffness (N/m)
4.0
3.9
3.8
3.7
3.6
3.5
3.4
10^1
10^2
10^3
10^4
10^5
10^6
Cycles
Young's Modulus (GPa)
52.0
51.0
50.0
49.0
48.0
47.0
46.0
45.0
925646 cycles
Normalized Stiffness
1.10
1.05
1.00
0.95
0.90
0
20
40
60
80
100
Life (%)
Turning Points Shift (mm)
0.05
0.00
-0.05
Trough
Peak

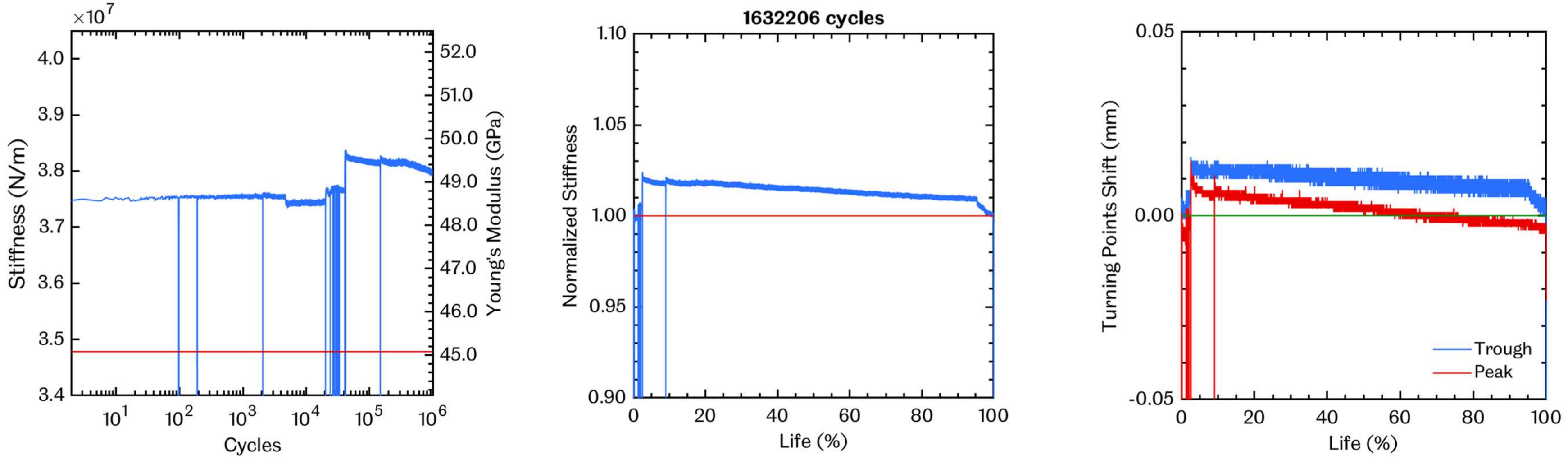
×10^7
Stiffness (N/m)
4.0
3.9
3.8
3.7
3.6
3.5
3.4
10^1
10^2
10^3
10^4
10^5
10^6
Cycles
Young's Modulus (GPa)
52.0
51.0
50.0
49.0
48.0
47.0
46.0
45.0
1632206 cycles
Normalized Stiffness
1.10
1.05
1.00
0.95
0.90
0
20
40
60
80
100
Life (%)
Turning Points Shift (mm)
0.05
0.00
-0.05
Trough
Peak